

Naval Surface Warfare Center Carderock Division

West Bethesda, MD 20817-5700

NSWCCD-61-TR-2021/10

June 2021

Platform Integrity Department
Technical Report

Temperature-Dependent Material Property Databases for Marine Steels – Part 4: HSLA-100

by

Jennifer K. Semple

Daniel H. Bechetti

Wei Zhang

Charles R. Fisher



DISTRIBUTION A. Approved for public release: distribution unlimited.

NSWCCD-61-TR-2021/10

June 2021

Platform Integrity Department
Technical Report

**Temperature-Dependent Material Property Databases for
Marine Steels – Part 4: HSLA-100**

by
Jennifer K. Semple
Daniel H. Bechetti
Wei Zhang
Charles R. Fisher

UNCLASSIFIED

REPORT DOCUMENTATION PAGE			<i>Form Approved</i> <i>OMB No. 0704-0188</i>		
Public reporting burden for this collection of information is estimated to average 1 hour per response, including the time for reviewing instructions, searching existing data sources, gathering and maintaining the data needed, and completing and reviewing this collection of information. Send comments regarding this burden estimate or any other aspect of this collection of information, including suggestions for reducing this burden to Department of Defense, Washington Headquarters Services, Directorate for Information Operations and Reports (0704-0188), 1215 Jefferson Davis Highway, Suite 1204, Arlington, VA 22202-4302. Respondents should be aware that notwithstanding any other provision of law, no person shall be subject to any penalty for failing to comply with a collection of information if it does not display a currently valid OMB control number. PLEASE DO NOT RETURN YOUR FORM TO THE ABOVE ADDRESS.					
1. REPORT DATE (DD-MM-YYYY) 14-06-2021		2. REPORT TYPE Technical Report		3. DATES COVERED (From - To) JAN 2018 - JUN 2019	
4. TITLE AND SUBTITLE Temperature-Dependent Material Property Databases for Marine Steels - Part 4: HSLA-100			5a. CONTRACT NUMBER N/A		
			5b. GRANT NUMBER N/A		
			5c. PROGRAM ELEMENT NUMBER N/A		
6. AUTHOR(S) Jennifer K. Semple Daniel H. Bechetti Wei Zhang Charles R. Fisher			5d. PROJECT NUMBER N/A		
			5e. TASK NUMBER		
			5f. WORK UNIT NUMBER		
7. PERFORMING ORGANIZATION NAME(S) AND ADDRESS(ES) AND ADDRESS(ES) Naval Surface Warfare Center, Carderock Division, Code 611 9500 MacArthur Boulevard West Bethesda, MD 20817-5700			8. PERFORMING ORGANIZATION REPORT NUMBER NSWCCD-61-TR-2021/10		
9. SPONSORING / MONITORING AGENCY NAME(S) AND ADDRESS(ES) William Mullins Program Manager, 332 Office of Naval Research Arlington, VA 22217			10. SPONSOR/MONITOR'S ACRONYM(S) ONR		
			11. SPONSOR/MONITOR'S REPORT NUMBER(S) N/A		
12. DISTRIBUTION / AVAILABILITY STATEMENT DISTRIBUTION A. Approved for public release: distribution unlimited.					
13. SUPPLEMENTARY NOTES					
14. ABSTRACT: The Lightweight Innovations for Tomorrow (LIFT) project entitled, Robust Distortion Control Methods and Implementation for Construction of Lightweight Metallic Structures - ICME Extension to Advanced Alloys, sought to address distortion issues with thin-plate steel fabrication of U.S. Navy ships. Integrated Computational Materials Engineering (ICME)-based tools and techniques were identified as the best path forward for distortion mitigation through computational simulation of the welding process. ICME tools require temperature-dependent material properties to achieve accurate computational results for distortion and residual stress. Properties of note include specific heat, thermal conductivity, coefficient of thermal expansion (CTE), elastic modulus, yield strength, and flow stress of alloys from room temperature to near melting. In addition, the temperatures associated with on-heating and on-cooling phase transformations and their variation with heating rate, cooling rate, and peak temperature are also important for the prediction of stress and distortion evolution. The integrated project team (IPT) made generating pedigreed, temperature-dependent material property databases of Navy-relevant steels a key task within the LIFT project. The testing plan included some of the most common marine steels used in the construction of U.S. Naval vessels; namely, DH36, HSLA-65, HSLA-80, HSLA-100, HY-80, and HY-100. Material testing for each of the six steel grades was performed jointly by the Welding Engineering Program within the Department of Materials Science and Engineering at the Ohio State University (OSU) and the Welding, Processing, and Nondestructive Evaluation Branch at the Naval Surface Warfare Center, Carderock Division (NSWCCD). The temperature-dependent material property data was then sent to ESI for adaptation for use in their welding-based, finite-element analysis (FEA) software colloquially known as SYSWELD. This report is part of a seven-part series detailing the pedigreed steel data. The first six reports will report and discuss the material properties for each of the individual steel grades, whereas the final report will compare and contrast the measured steel properties across all six steels, while also comparing them to the available literature data. This report will focus specifically on the data associated with HSLA-100 steel.					
15. SUBJECT TERMS ICME, CWM, SYSWELD, Computational Simulation, Steel, Welding, Material Database, HSLA-100					
16. SECURITY CLASSIFICATION OF:			17. LIMITATION OF ABSTRACT	18. NUMBER OF PAGES 92	19a. RESPONSIBLE PERSON Charles Fisher
a. REPORT UNCLASSIFIED	b. ABSTRACT UNCLASSIFIED	c. THIS PAGE UNCLASSIFIED			19b. TELEPHONE NUMBER (301) 227-4969

UNCLASSIFIED

CONTENTS

	<i>Page</i>
FIGURES	iv
TABLES	ix
ADMINISTRATIVE INFORMATION	xi
ACKNOWLEDGEMENTS	xi
EXECUTIVE SUMMARY	1
BACKGROUND	1
APPROACH	3
Material Testing Program	3
Chemical Composition.....	3
Heat Affected Zone Phase Transformation Analysis.....	3
Thermo-Physical Property Analysis	5
Thermo-Mechanical Property Analysis	6
Fabrication of Welded Specimens	9
Microstructural Analysis.....	11
RESULTS AND DISCUSSION	11
Chemical Composition.....	11
Solidus and Liquidus Analysis.....	11
Base Metal Microstructure.....	12
Heat Affected Zone Phase Transformation Analysis.....	13
Dilation Curve Analysis Method	13
Austenite Transformation Temperature Measurement	14
Continuous Cooling Transformation Diagrams.....	15
Weldment Microstructures.....	25
Thermo-Physical Property Analysis	30
Thermo-Mechanical Property Analysis	34
CONCLUSIONS	41
APPENDIX	42
Appendix A: Plate Conformance Certificate and Chemical Composition for HSLA-10042	
Appendix B: Continuous Cooling Transformation Curves	45
Appendix C: Representative Microstructures of HSLA-100 CCT Specimens.....	59
Appendix D: Microhardness Measurements.....	65

Appendix E: Thermo-Physical Property Datasets for HSLA-100.....83
Appendix F: Thermo-Mechanical Properties.....85
REFERENCES.....91

FIGURES

	<i>Page</i>
Figure 1. Photographs of the Gleeble-based dilatometry experimental set-up.	5
Figure 2. Tensile specimens for Gleeble-based mechanical testing of HSLA-100 steel: a) dimensions for single-reduced gauge section, b) sample speckle pattern for DIC testing	7
Figure 3. Specimen dimensions for Gleeble-based mechanical testing of HSLA-100 steel for a double-reduced gauge section.	8
Figure 4. Photographs of the Gleeble-based mechanical testing experimental set-up.	9
Figure 5. Representative a) butt and b) tee joint weldments of HSLA-100 material investigated for plate, weld, and HAZ microstructures.	10
Figure 6. Representative micrograph of HSLA-100 steel plate base metal microstructure at 1000x magnification using LOM.....	13
Figure 7. Representative on-heating dilatometry curve for HSLA-100 steel, showing the linear extrapolation and derivative curve methods for evaluating the ferrite to austenite reaction.....	14
Figure 8. Variation in austenite transformation start and finish temperatures with heating rate for HSLA-100 material.	15
Figure 9. CCT diagram for HSLA-100 heated to peak temperature of 790 °C (1454 °F).	16
Figure 10. CCT diagram for HSLA-100 heated to peak temperature of 1000 °C (1832 °F).	16
Figure 11. CCT diagram for HSLA-100 heated to peak temperature of 1150 °C (2102 °F).	17
Figure 12. CCT diagram for HSLA-100 heated to peak temperature of 1350 °C (2462 °F).	17
Figure 13. Variation of start temperature for the ferrite transformation shown in Figures 9-12.	18
Figure 14. Variation of start temperature for the bainite transformation shown in Figures 9-12.	18
Figure 15. Variation of start temperature for the martensite transformation shown in Figures 9-12.	19

Figure 16. Measured Vickers microhardness for HSLA-100 dilatometry specimens as a function of peak temperature and cooling rate.....20

Figure 17. Representative microstructures of the second pass fusion zone for the **a)** butt joint and **b)** tee joint configuration.26

Figure 18. Representative light optical micrographs of the second pass of the HSLA-100 butt joint **a)** CGHAZ, **b)** FGHAZ close to the CGHAZ, **c)** FGHAZ close to the ICHAZ, and **d)** ICHAZ.....27

Figure 19. Composite image of light optical micrographs of the HSLA-100 butt joint overlaid with contour map of microhardness values in units of HV₂₀₀.28

Figure 20. Composite image of light optical micrographs of the HSLA-100 butt joint overlaid with contour map of microhardness values in units of HV₂₀₀, with color scale that represents full range of values.28

Figure 21. Representative light optical micrographs of the second pass of the HSLA-100 tee joint **a)** CGHAZ, **b)** FGHAZ close to the CGHAZ, **c)** FGHAZ close to the ICHAZ, and **d)** ICHAZ.....29

Figure 22. Composite image of light optical micrographs of the HSLA-100 fillet overlaid with contour map of microhardness values in units of HV₂₀₀.30

Figure 23. Representative on-heating dilatometry curve for HSLA-100, showing typical CTE analysis and results.31

Figure 24. Density of HSLA-100 steel as a function of temperature. LIFT data measured using analysis of Gleeble-based dilation curves in accordance with **Equations 2** and **3**.32

Figure 25. Measured specific heat for HSLA-100 steel at various temperatures.....32

Figure 26. Measured thermal diffusivity for HSLA-100 steel at various temperatures.....33

Figure 27. Calculated thermal conductivity for HSLA-100 steel at various temperatures.....33

Figure 28. Assumed elevated temperature elastic modulus for HSLA-100 steel as adapted from references [31] [32].....34

Figure 29. Measured elevated temperature 0.2% offset yield strength for HSLA-100 steel.35

Figure 30. Measured elevated temperature ultimate tensile strength (UTS) for HSLA-100 steel.35

Figure 31.	Yield strength of simulated HSLA-100 CGHAZs after heating to 1350 °C (2462 °F) and cooling at different rates as compared with base material yield strength.....	36
Figure 32.	On-heating flow stress behavior for HSLA-100 steel at various temperatures.....	38
Figure 33.	On-heating flow stress behavior for HSLA-100 steel at testing temperatures above the austenitic phase transformation.	39
Figure 34.	Flow stress behavior at various temperatures for HSLA-100 steel after cooling at 1 °C/s (1.8 °F/s) from a peak temperature of 1350 °C (2462 °F).	39
Figure 35.	Flow stress behavior at various temperatures for HSLA-100 steel after cooling at 10 °C/s (18 °F/s) from a peak temperature of 1350 °C (2462 °F).	40
Figure 36.	Flow stress behavior at various temperatures for HSLA-100 steel after cooling at 25 °C/s (45 °F/s) from a peak temperature of 1350 °C (2462 °F).	40
Figure 37.	Flow stress behavior at various temperatures for HSLA-100 steel after cooling at 100 °C/s (180 °F/s) from a peak temperature of 1350 °C (2462 °F).	41
Figure 38.	Dilation curve from a HSLA-100 Gleeble sample heated to a peak temperature of 790 °C and cooled at 1 °C/s.....	46
Figure 39.	Dilation curve from a HSLA-100 Gleeble sample heated to a peak temperature of 790 °C and cooled at 5 °C/s.....	47
Figure 40.	Dilation curve from a HSLA-100 Gleeble sample heated to a peak temperature of 790 °C and cooled at 10 °C/s.....	47
Figure 41.	Dilation curve from a HSLA-100 Gleeble sample heated to a peak temperature of 790 °C and cooled at 25 °C/s.....	48
Figure 42.	Dilation curve from a HSLA-100 Gleeble sample heated to a peak temperature of 790 °C and cooled at 100 °C/s.....	48
Figure 43.	Dilation curve from a HSLA-100 Gleeble sample heated to a peak temperature of 790 °C and cooled at 200 °C/s.....	49
Figure 44.	Dilation curve from a HSLA-100 Gleeble sample heated to a peak temperature of 1000 °C and cooled at 1 °C/s.....	49
Figure 45.	Dilation curve from a HSLA-100 Gleeble sample heated to a peak temperature of 1000 °C and cooled at 5 °C/s.....	50

Figure 46.	Dilation curve from a HSLA-100 Gleeble sample heated to a peak temperature of 1000 °C and cooled at 10 °C/s.....	50
Figure 47.	Dilation curve from a HSLA-100 Gleeble sample heated to a peak temperature of 1000 °C and cooled at 25 °C/s.....	51
Figure 48.	Dilation curve from a HSLA-100 Gleeble sample heated to a peak temperature of 1000 °C and cooled at 100 °C/s.....	51
Figure 49.	Dilation curve from a HSLA-100 Gleeble sample heated to a peak temperature of 1000 °C and cooled at 200 °C/s.....	52
Figure 50.	Dilation curve from a HSLA-100 Gleeble sample heated to a peak temperature of 1150 °C and cooled at 1 °C/s.....	52
Figure 51.	Dilation curve from a HSLA-100 Gleeble sample heated to a peak temperature of 1150 °C and cooled at 5 °C/s.....	53
Figure 52.	Dilation curve from a HSLA-100 Gleeble sample heated to a peak temperature of 1150 °C and cooled at 10 °C/s.....	53
Figure 53.	Dilation curve from a HSLA-100 Gleeble sample heated to a peak temperature of 1150 °C and cooled at 25 °C/s.....	54
Figure 54.	Dilation curve from a HSLA-100 Gleeble sample heated to a peak temperature of 1150 °C and cooled at 100 °C/s.....	54
Figure 55.	Dilation curve from a HSLA-100 Gleeble sample heated to a peak temperature of 1150 °C and cooled at 200 °C/s.....	55
Figure 56.	Dilation curve from a HSLA-100 Gleeble sample heated to a peak temperature of 1350 °C and cooled at 1 °C/s.....	55
Figure 57.	Dilation curve from a HSLA-100 Gleeble sample heated to a peak temperature of 1350 °C and cooled at 5 °C/s.....	56
Figure 58.	Dilation curve from a HSLA-100 Gleeble sample heated to a peak temperature of 1350 °C and cooled at 10 °C/s.....	56
Figure 59.	Dilation curve from a HSLA-100 Gleeble sample heated to a peak temperature of 1350 °C and cooled at 25 °C/s.....	57
Figure 60.	Dilation curve from a HSLA-100 Gleeble sample heated to a peak temperature of 1350 °C and cooled at 100 °C/s.....	57
Figure 61.	Dilation curve from a HSLA-100 Gleeble sample heated to a peak temperature of 1350 °C and cooled at 200 °C/s.....	58

Figure 62. Representative microstructures from HSLA-100 dilatometry specimens heated to a peak temperature of 790 °C (1454 °F) and continuously cooled at various rates. **(a-f):** 1, 5, 10, 25, 100, and 200 °C/s (1.8, 9, 18, 45, 180, and 360 °F/s).....59

Figure 63. SEM images showing representative microstructures of HSLA-100 dilatometry specimens heated to a peak temperature of 790 °C (1454 °F) and continuously cooled at **a)** 100 °C/s (180 °F/s), and **b)** 200 °C/s (360 °F/s).....60

Figure 64. Representative microstructures from HSLA-100 dilatometry specimen heated to a peak temperature of 1000 °C (1832 °F) and continuously cooled at various rates. **(a-f):** 1, 5, 10, 25, 100, and 200 °C/s (1.8, 9, 18, 45, 180, and 360 °F/s).....61

Figure 65. SEM images showing representative microstructures of HSLA-100 dilatometry specimens heated to a peak temperature of 1000 °C (1832 °F) and continuously cooled at: **a, b)** 25 °C/s (45 °F/s), **c)** 100 °C/s (180 °F/s), and **d)** 200 °C/s (360 °F/s).....62

Figure 66. Representative microstructures from HSLA-100 dilatometry specimens heated to a peak temperature of 1150 °C (2102 °F) and continuously cooled at various rates. **(a-f):** 1, 5, 10, 25, 100, and 200 °C/s (1.8, 9, 18, 45, 180, and 360 °F/s).....63

Figure 67. Representative microstructures from HSLA-100 dilatometry specimens heated to a peak temperature of 1350 °C (2462 °F) and continuously cooled at various rates. **(a-f):** 1, 5, 10, 25, 100, and 200 °C/s (1.8, 9, 18, 45, 180, and 360 °F/s).....64

Figure 68. Uniaxial tension stress-strain curves from Gleeble tensile samples thermally cycled to a peak temperature of 1350 °C (2462 °F), cooled at 1 °C/s (1.8 °F/s), then reheated to the test temperature.89

Figure 69. Uniaxial tension stress-strain curves from Gleeble tensile samples thermally cycled to a peak temperature of 1350 °C (2462 °F), cooled at 10 °C/s (18 °F/s), then reheated to the test temperature.89

Figure 70. Uniaxial tension stress-strain curves from Gleeble tensile samples thermally cycled to a peak temperature of 1350 °C (2462 °F), cooled at 25 °C/s (45 °F/s), then reheated to the test temperature.90

Figure 71. Uniaxial tension stress-strain curves from Gleeble tensile samples thermally cycled to a peak temperature of 1350 °C (2462 °F), cooled at 100 °C/s (180 °F/s), then reheated to the test temperature.90

TABLES

	<i>Page</i>
Table 1. Test Matrix for HAZ CCT Diagram Development.....	4
Table 2. Nominal Welding Parameters used to Fabricate HSLA-100 Butt and Tee Joints	10
Table 3. Chemical Composition of HSLA-100 Material (wt.%).....	12
Table 4. Measured Phase Fraction of HSLA-100 CCT Specimens Thermally Cycled to a Peak Temperature of 790 °C (1454 °F).....	21
Table 5. Measured Phase Fraction of HSLA-100 CCT Specimens Thermally Cycled to a Peak Temperature of 1000 °C (1832 °F).....	23
Table 6. Measured Phase Fraction of HSLA-100 CCT Specimens Thermally Cycled to a Peak Temperature of 1150 °C (2102 °F).....	24
Table 7. Measured Phase Fraction of HSLA-100 CCT Specimens Thermally Cycled to a Peak Temperature of 1350 °C (2462 °F).....	25
Table 8. Chemical Composition of HSLA-100 Base Plate as Measured by OSU.....	44
Table 9. Austenite Transformation Temperatures as Illustrated in Figure 8	45
Table 10. Experimentally Measured On-Cooling Transformation Temperatures for HSLA-100 Dilatometry Specimens Cooled from 790 °C (1454 °F).....	45
Table 11. Experimentally Measured On-Cooling Transformation Temperatures for HSLA-100 Dilatometry Specimens Cooled from 1000 °C (1832 °F).....	45
Table 12. Experimentally Measured On-Cooling Transformation Temperatures for HSLA-100 Dilatometry Specimens Cooled from 1150 °C (2102 °F).....	46
Table 13. Experimentally Measured On-Cooling Transformation Temperatures for HSLA-100 Dilatometry Specimens Cooled from 1350 °C (2462 °F).....	46
Table 14. Vickers Microhardness of HSLA-100 as a Function of Peak Temperature and Cooling Rate.....	65
Table 15. Vickers Microhardness Measurements across the Experimental Butt Joint Weldment Illustrated in Figure 20	66
Table 16. Vickers Microhardness Measurements across the Experimental Tee Joint Weldment Illustrated in Figure 22	74
Table 17. Experimentally Measured Specific Heat of HSLA-100	83

Table 18.	Experimentally Measured Thermal Properties of HSLA-100	84
Table 19.	Assumed Elevated Temperature Elastic Modulus for HSLA-100 Base Material.	85
Table 20.	Elevated Temperature Mechanical Properties of HSLA-100 Base Material.....	85
Table 21.	Yield Strength of Simulated HSLA-100 CGHAZs after Heating to 1350 °C (2462 °F) and Cooling at Different Rates.....	86
Table 22.	On-Heating Flow Behavior of HSLA-100 Base Material. Note: Data as shown in Figures 32-33	86
Table 23.	Flow Stress of Simulated HSLA-100 CGHAZs after Heating to 1350 °C (2462 °F) and Cooling at 1 °C/s (1.8 °F/s)	87
Table 24.	Flow Stress of Simulated HSLA-100 CGHAZs after Heating to 1350 °C (2462 °F) and Cooling at 10 °C/s (18 °F/s)	87
Table 25.	Flow Stress of Simulated HSLA-100 CGHAZs after Heating to 1350 °C (2462 °F) and Cooling at 25 °C/s (45 °F/s)	87
Table 26.	Flow Stress of Simulated HSLA-100 CGHAZs after Heating to 1350 °C (2462 °F) and Cooling at 100 °C/s (180 °F/s)	88
Table 27.	Engineering Fracture Strain for the Specimens Shown in Figures 34-36	88

ADMINISTRATIVE INFORMATION

The work described in this report was performed by the Welding, Processing, and Nondestructive Evaluation Branch (Code 611) of the Platform Integrity Department at the Naval Surface Warfare Center, Carderock Division (NSWCCD) and by the Department of Materials Science and Engineering at the Ohio State University. The work was funded in FY18-19 by the Office of Naval Research (ONR), in support of the Lightweight Innovations for Tomorrow (LIFT) Institute's program entitled *Robust Distortion Control Methods and Implementation for Construction of Lightweight Metallic Structures – ICME Extension to Advanced Alloys*.

ACKNOWLEDGEMENTS

The authors would like to thank the other members of the LIFT Joining-R4-3 integrated project team, including other engineers at the Naval Surface Warfare Center, Carderock Division (Matthew Sinfield, Maria Posada, and Johnnie Deloach), Huntington Ingalls Industries – Ingalls Shipbuilding (T.D. Huang, Randy Johnson, Yu-Ping Yang, Steve Scholler, Charlotte Merritt, Shannon Dolese, Anthony Copeland, Andrew Nicholson, Lance Carnahan, Stacey Merritt, Win Delancey, Dianna Genton, and John Walks), the University of Michigan (Pingsha Dong, Jack Hu, Theodor Freiheit), the Ohio State University (Colleen Hilla and Chris Cathis), ESI (Yogendra [San] Gooroochan and Mark Doroudian), and LIFT (Melvin Hawke, Alan Taub, and Hadrian Rori), for their technical assistance in the completion of this work.

This page intentionally left blank

EXECUTIVE SUMMARY

The Lightweight Innovations for Tomorrow (LIFT) project entitled, Robust Distortion Control Methods and Implementation for Construction of Lightweight Metallic Structures – ICME Extension to Advanced Alloys, sought to address distortion issues with thin-plate steel fabrication of U.S. Navy ships. Integrated Computational Materials Engineering (ICME)-based tools and techniques were identified as the best path forward for distortion mitigation through computational simulation of the welding process. ICME tools require temperature-dependent material properties to achieve accurate computational results for distortion and residual stress. Properties of note include specific heat, thermal conductivity, coefficient of thermal expansion (CTE), elastic modulus, yield strength, and flow stress of alloys from room temperature to near melting. In addition, the temperatures associated with on-heating and on-cooling phase transformations and their variation with heating rate, cooling rate, and peak temperature are also important for the prediction of stress and distortion evolution.

The integrated project team (IPT) made generating pedigreed, temperature-dependent material property databases of Navy-relevant steels a key task within the LIFT project. The testing plan included some of the most common marine steels used in the construction of U.S. Naval vessels; namely, DH36, HSLA-65, HSLA-80, HSLA-100, HY-80, and HY-100. Material testing for each of the six steel grades was performed jointly by the Welding Engineering Program within the Department of Materials Science and Engineering at the Ohio State University (OSU) and the Welding, Processing, and Nondestructive Evaluation Branch at the Naval Surface Warfare Center, Carderock Division (NSWCCD). The temperature-dependent material property data was then sent to ESI for adaptation for use in their welding-based, finite-element analysis (FEA) software colloquially known as SYSWELD.

This report is part of a seven-part series detailing the pedigreed steel data. The first six reports will report and discuss the material properties for each of the individual steel grades, whereas the final report will compare and contrast the measured steel properties across all six steels, while also comparing them to the available literature data. This report will focus specifically on the data associated with HSLA-100 steel.

BACKGROUND

The Lightweight Innovations for Tomorrow (LIFT) project entitled, *Robust Distortion Control Methods and Implementation for Construction of Lightweight Metallic Structures – ICME Extension to Advanced Alloys*, is a collaborative research project to address the complex fabrication problems that arise from the use of thin, high-strength steel panels for ship construction. The importance of lightweighting in the commercial and military shipbuilding sectors has gained attention in recent decades as a way to increase the performance capabilities of products while also reducing total ownership costs. Over the past decade, the production ratio of thin plate (10 mm [3/8-in.] or less) to thicker plate structures for steel construction at Huntington Ingalls Industries – Ingalls Shipbuilding has risen to over 80% in the Coast Guard’s National Security Cutter (NSC) program. Modern naval vessel designs also make greater use of complex panels with inserts and cutouts, further increasing the fabrication complexity to achieve weight savings while meeting structural requirements.

European shipbuilding research suggests that 30% of hull fabrication costs can be attributed to rework and fit-up issues due to distortion [1]. Integrated Computational Materials Engineering (ICME)-

based prediction tools can be used to quantify distortions associated with the fabrication process of complex stiffened panels or other lightweight structures. These tools, once validated on selected product forms, could be used to establish recommended fitting, fixturing, welding, and assembly sequencing for optimized distortion control in thin-plate steel construction.

These ICME tools require detailed, reliable databases of temperature-dependent material properties in order to increase the accuracy of calculated distortion and residual stresses in welded metallic structures. Of highest importance to the fidelity of such models are the thermo-physical and thermo-mechanical properties of the material(s) being joined. The properties of note include specific heat, thermal conductivity, coefficient of thermal expansion (CTE), elastic modulus, yield strength, and flow stress of the alloy, from room temperature to near melting. The temperatures associated with on-heating and on-cooling phase transformations and their variation with heating rate, cooling rate, and peak temperature are also important for the prediction of stress and distortion evolution.

While some of these data exist for the most common Navy steels, these are generally not suitable for use in high-fidelity welding-focused computational models for several reasons. First, the methods of data generation are inconsistent because the testing was completed over many decades by separate researchers and programs. Also, significant gaps exist in the data, especially at temperatures above approximately 400 °C (~750 °F). Additionally, some available data are restricted against public distribution. Finally, the data are, in general, subject to reliability issues because of changes in material fabrication and testing practices that have occurred in the decades since the data were generated. To combat this lack of comprehensive and consistent data, the integrated project team (IPT) made generating pedigreed, temperature-dependent material property databases of Navy-relevant steels a key task within the LIFT project. A major portion of the tasking involved analysis of heat-affected zone (HAZ) microstructures, as this region of rapidly changing microstructure results in significant changes in resultant mechanical properties. These varied HAZ region microstructures of Navy-relevant also do not have well-established mechanical property data, especially as a function of temperature and heating or cooling rate.

The testing plan included some of the most common marine steels used in the construction of U.S. Naval vessels; namely DH36, HSLA-65, HSLA-80, HSLA-100, HY-80, and HY-100. HSLA is short for “high-strength low-alloy,” whereas HY stands for “high yield.” The number designation behind HSLA and HY is the minimum yield strength of the plate material in units of ksi. Current (as of this writing) specifications for these alloys can be found in references [2] [3] [4]. Material testing for each of the six steel grades was performed jointly by the Welding Engineering Program within the Department of Materials Science and Engineering at the Ohio State University (OSU) and the Welding, Processing, and Nondestructive Evaluation Branch at the Naval Surface Warfare Center, Carderock Division (NSWCCD). The temperature-dependent material property data was then sent to ESI for adaptation for use in their welding-based, finite-element analysis (FEA) software colloquially known as *SYSWELD*.

This report is part of a seven-part series based on the pedigreed steel data. The first six reports will focus on establishing the material properties for each of the individual steel grades, whereas the final report will compare and contrast the measured steel properties across all six steels, while also comparing them to the available literature data. Follow-on reports detailing use of these temperature-dependent material databases within the LIFT-funded program are also expected. While this report focuses on HSLA-100 data, the citation for the previous report on DH36 is [5], HSLA-65 is [6], and HSLA-80 is [7].

APPROACH

Material Testing Program

The material property assessment program was developed through inputs from welding engineers at NSWCCD, researchers at OSU, and modeling experts at ESI. The program focused on generating the types of data required to develop Navy-relevant material databases for use by ESI's commercial software, *SYSWELD*. The raw data could also be adapted for use by other FEA tools, such as Hexagon's *Simufact Welding* or the welding module for *Abaqus*. Specific data included thermo-physical and mechanical properties of the alloys of interest, from room temperature up to near-melting. Density, heat capacity, thermal conductivity, and coefficient of thermal expansion (CTE) were identified as the most important thermo-physical properties. Mechanical properties of interest included the elastic modulus, yield strength, and flow stress.

Material from a single HSLA-100 steel plate procured to NAVSEA Technical Publication T9074-BD-GIB-010/0300 (Tech Pub 300) [4] was analyzed for this project. The nominally 4.76 mm (3/16-in.) thick plate was acquired by Huntington Ingalls Industries – Ingalls Shipbuilding (HII – Ingalls). The room temperature yield strength and elongation requirements for the alloy are 690-828 MPa (100-120 ksi) and 17% in 50 mm (2-in.), respectively [4]. There are no ultimate tensile strength requirements for HSLA-100 plate procured to Tech Pub 300 [4]. The plate conformance certification sheet for the material investigated in this study is given in **Appendix A**. A portion of this plate was cut into 610 mm by 305 mm (24-in. by 12-in.) pieces and shipped to both NSWCCD and OSU for determination of temperature-dependent material properties.

Chemical Composition

The chemical composition of the base material was measured at OSU using optical emission spectroscopy in accordance with ASTM E415 [8].

Heat Affected Zone Phase Transformation Analysis

Phase transformations of HSLA-100 as a function of austenitization temperature and cooling rate were assessed via dilatometry. Continuous cooling transformation (CCT) diagrams were developed for four regions of the heat affected zone (HAZ) that are subject to microstructural transformation during welding: the intercritical region (ICHAZ); the low-temperature, fine-grained region (FGHAZ1); the high-temperature, fine-grained region (FGHAZ2); and the coarse-grained region (CGHAZ).

Heating and cooling rates for these regions in HSLA-100 were assumed to be the similar those for DH36 weldments [5]. As part of the DH36 effort [5], the heating and cooling rates were defined by combining typical heat inputs used in the fabrication of DH36 weldments, from 0.4 to 2.6 kJ/mm (10 to 65 kJ/in) as suggested by Ingalls engineers, with numerical simulation of the heat flow using the *SmartWeld* program from Sandia National Laboratories [9]. From these calculations, it was determined that peak temperatures (T_{peak}) between 790 and 1350 °C (1454 and 2462 °F), in combination with cooling rates between 1 and 200 °C/s (1.8 and 360 °F/s), would provide information covering a sufficiently broad range of phase transformation behavior relevant to both slowly-cooled welds (*e.g.*, high heat input welds on thin plate) and rapidly-cooled welds (*e.g.*, low heat input welds on thick plate). These CCT diagrams informed the temperature-dependent mechanical property testing program as well, specifically for heating and cooling rates, peak temperatures, and various testing temperatures.

In addition to the on-cooling CCT diagram development, this portion of the testing program also involved a detailed assessment of the on-heating austenite transformation as a function of heating rate. Just as on-cooling transformation temperatures vary with cooling rate, so does on-heating austenitization temperature (A_{c1} and A_{c3}). Heating rates between 10 and 2000 °C/s (18 and 3632 °F/s) were used to study these variations. **Table 1** shows the full test matrix utilized for HAZ CCT diagram development.

Table 1. Test Matrix for HAZ CCT Diagram Development

Test Type	Region	Peak Temperature, °C (°F)	Heating Rate, °C/s (°F/s)	Soak Time, s	Cooling Rate, °C/s (°F/s)
A_{c1}/A_{c3} Determination	N/A	1200 (2192)	10 (18) 100 (180) 200 (360) 500 (900) 1000 (1800) 2000 (3600)	N/A	N/A
CCT Diagram Development	ICHAZ	790 (1454)	200 (360)	2	1 (1.8)
	FGHAZ1	1000 (1832)			5 (9)
	FGHAZ2	1150 (2102)			10 (18)
	CGHAZ	1350 (2462)			25 (45)
					100 (180)
					200 (360)

Execution of this test matrix was performed at NSWCCD by employing a Gleeble 3500 thermo-mechanical simulation apparatus to apply the prescribed heating and cooling rates. The Gleeble operates on the principles of resistive heating, conductive cooling through water-cooled fixturing, and rapid (50 kHz) control system feedback to apply precise thermal cycles even at rapid heating and cooling rates that cannot be easily achieved by other apparatus. The Gleeble 3500 system, in combination with the apparatus's standard 'Pocket Jaw' setup, used full contact copper grips and 70 mm (2.76-in.) long specimens with 3 mm (0.118-in.) diameters. A linear variable differential transformer (LVDT)-type contact extensometer was used to measure diametric dilation of the specimens during heating and cooling. All dilatometry specimens were extracted perpendicular to the rolling direction of the plate, and all dilatometry tests were performed in an argon atmosphere. The typical experimental setup for the dilatometry testing is shown in **Figure 1**.

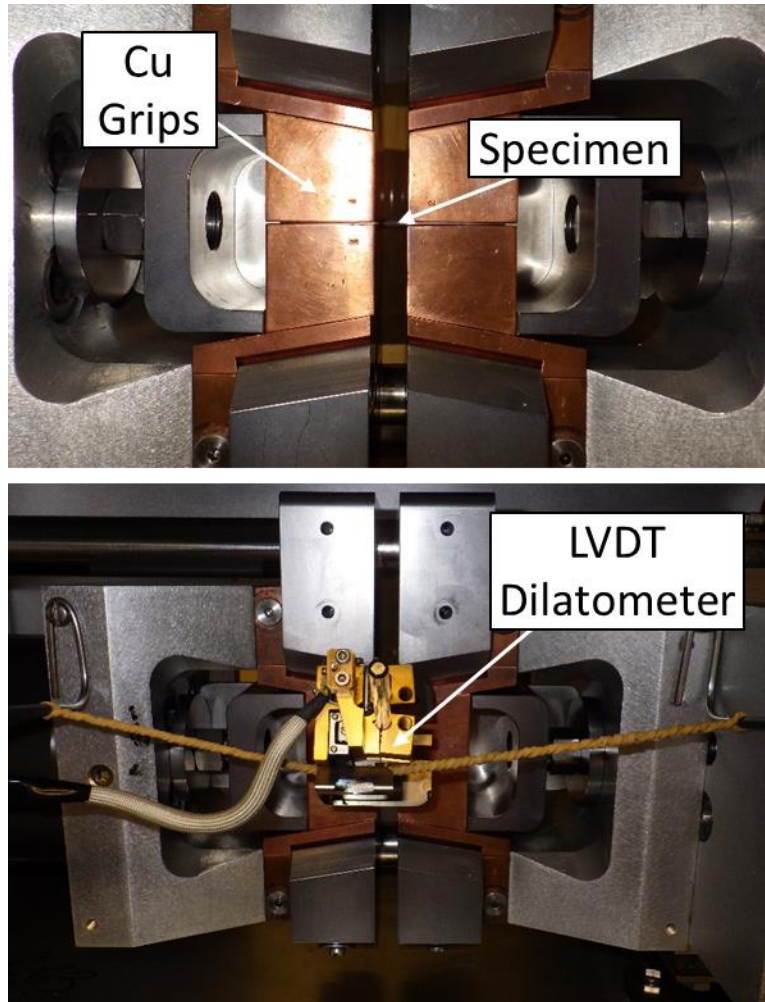


Figure 1. Photographs of the Gleeble-based dilatometry experimental set-up.

Thermo-Physical Property Analysis

Specimens were sent to the Thermophysical Properties Research Laboratory, Inc. (TPRL) in West Lafayette, IN for analysis of thermal diffusivity (α) and specific heat (C_p). Thermal diffusivity was measured using the laser flash method according to ASTM E1461 [10]. Specific heat was measured using differential scanning calorimetry (DSC) methods according to ASTM E1269 [11]. Coefficient of thermal expansion (CTE) was measured from the on-heating Gleeble dilatometry data in two regimes: 240 to 690 °C (464 to 1274 °F) for the base material microstructure, and 860 to 1100 °C (1580 to 2012 °F) for austenite. No attempt was made to determine CTE during the on-heating transformation. CTE calculations were either performed by linear fitting or by discrete analysis using the dilation data endpoints from each temperature range in conjunction with **Equation 1**. The material was assumed to be isotropic.

$$\alpha_T = \left(\frac{\Delta d}{d_0}\right) \left(\frac{1}{\Delta T}\right) \quad (1)$$

where $\alpha_T \equiv$ Linear coefficient of thermal expansion [$^{\circ}\text{C}^{-1}$]
 $\Delta d \equiv$ Change in specimen diameter over the chosen temperature range [cm]

$d_0 \equiv$ Initial specimen diameter [cm]
 $\Delta T \equiv$ Temperature range [$^{\circ}\text{C}$]

The temperature-dependent density (ρ) was calculated using a theoretical cubic volume element under the assumption of isotropic thermal expansion:

$$\rho(T) = \frac{\rho_0 V_0}{V(T)} \quad (2)$$

where $\rho(T) \equiv$ Density at temperature T [g/cm^3]
 $\rho_0 \equiv$ Room temperature density provided by TPRL [g/cm^3]
 $V_0 \equiv$ Room temperature volume of the theoretical cubic element [cm^3]
 $V(T) \equiv$ Volume of the theoretical cubic element at temperature T [cm^3]

V_0 was calculated assuming a side length equal to the room temperature width of the dilatometry specimens. This value was chosen because, as shown in **Figure 1**, it corresponds to the starting gauge length for the dilatometer used to measure thermal expansion. A theoretical cubic volume element was chosen instead of the actual specimen dimensions to subvert potential complications with measuring dimensions that were not directly measured by the dilatometer (*e.g.*, the effect of thermal gradients on measurement of the specimen's longitudinal expansion). V_T was simply calculated by:

$$V(T) = [w(T)]^3 \quad (3)$$

where $w(T) \equiv$ Dilatometer-measured specimen width at temperature T [cm]

This method allowed calculation of the density through the austenite transformation. Finally, thermal conductivity (λ) as a function of temperature was then calculated by using **Equation 4**:

$$\lambda = \rho \cdot C_p \cdot \alpha \quad (4)$$

where $\lambda \equiv$ Thermal conductivity [$\text{W}/\text{cm}\cdot^{\circ}\text{C}$]
 $C_p \equiv$ Specific heat capacity [$\text{J}/\text{g}\cdot^{\circ}\text{C}$]
 $\rho_0 \equiv$ Room temperature density [g/cm^3]
 $\alpha \equiv$ Thermal diffusivity [cm^2/s]

Thermo-Mechanical Property Analysis

Tensile specimens were machined from the HSLA-100 plates according to the dimensions shown in **Figure 2a**. All specimens were extracted with their length perpendicular to the rolling direction of the plate. Elastic modulus, yield strength, and flow stress were identified as the required mechanical properties from room temperature up to near-melting. On-heating tension testing of the HSLA-100 base material at temperatures between 22 and 1100 $^{\circ}\text{C}$ (72 and 2012 $^{\circ}\text{F}$) was performed by The Ohio State University using the Gleeble 3800. Specimens were spray painted with an yttrium oxide (Y_2O_3) solvent-based paint to provide a contrast between the black speckle pattern sprayed onto the face of specimens, as shown in **Figure 2b**. Tensile testing was carried out using digital image correlation in lieu of a contact extensometer. Room temperature testing was performed in accordance with ASTM A370 [12], and elevated temperature testing was performed in accordance with ASTM E21 [13].

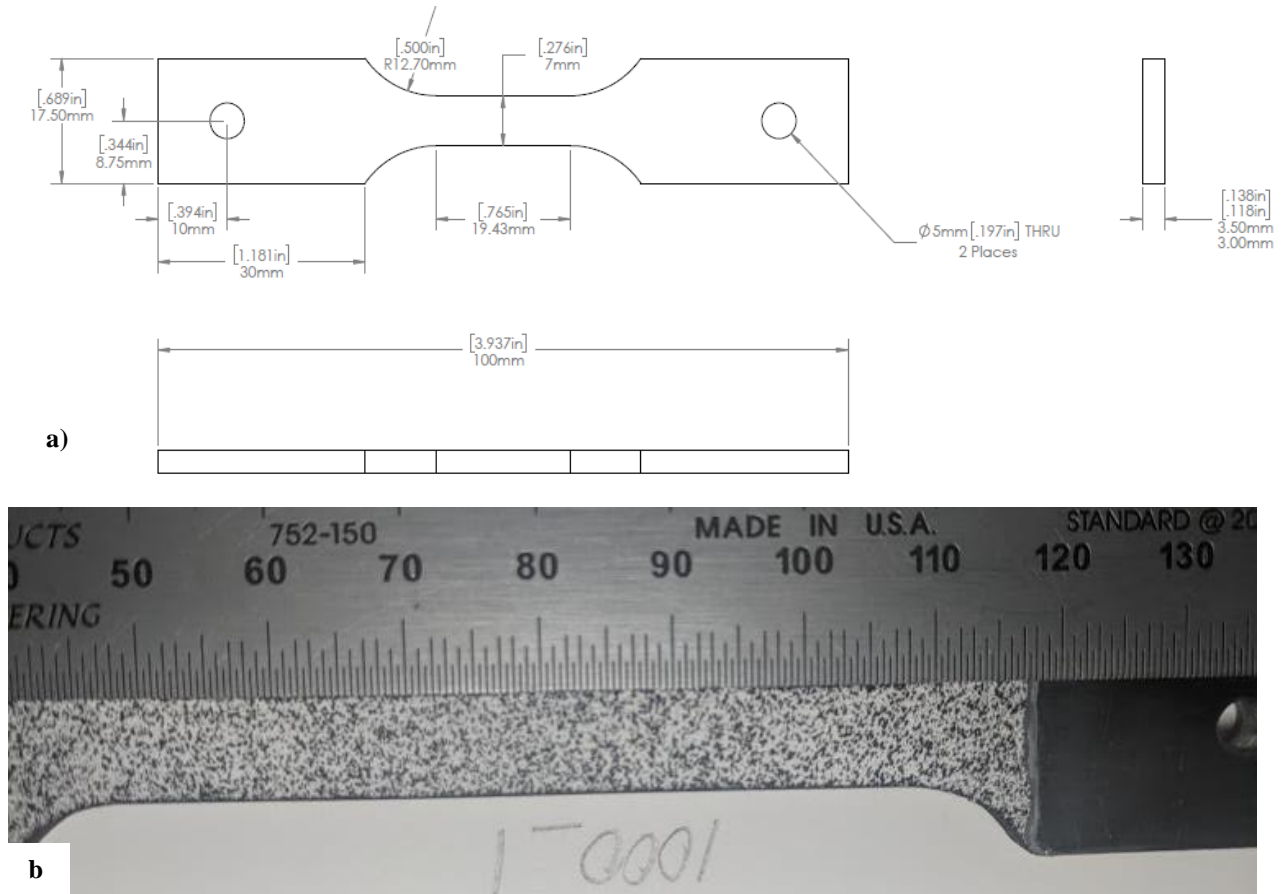


Figure 2. Tensile specimens for Gleeble-based mechanical testing of HSLA-100 steel: **a)** dimensions for single-reduced gauge section, **b)** sample speckle pattern for DIC testing (dimensions in mm).

On-cooling mechanical properties were measured using the Gleeble 3500 at NSWCCD. Prior to mechanical testing, the specimens were thermally cycled to generate different initial microstructures based on the results of the CCT diagram development described above. For HSLA-100, microstructural analysis indicated that substantially different microstructures formed when the material was cooled at 1, 10, 25, and 100 °C/s (1.8, 18, 45, and 180 °F/s). Because of programmatic time constraints, only a peak temperature of 1350 °C (2462 °F) was applied to the tensile specimens. All specimens were heated in an argon atmosphere, and forced air was used to meet cooling rates of 10 °C/s (18 °F/s) and above. All specimens were cooled to room temperature, and thereafter a contact longitudinal extensometer was affixed. The specimens were then reheated to the test temperature at a rate of 10 °C/s (18 °F/s) and soaked for 10 seconds before being pulled to failure in crosshead control mode at strain rates targeting those prescribed in ASTM E21 [13]. The crosshead displacement rate used was 0.30 mm/min (0.012 in/min). It is acknowledged that this is not the most representative method of testing for welding-related applications because the stresses that develop during welding do so rapidly and while the material is cooling and undergoing phase transformations. However, given the programmatic intent of establishing the mechanical behavior of specific microstructures and the need to avoid exposing the strain measurement device to exceedingly high temperatures, the method of cooling to room temperature and tension testing after reheating was determined to be an acceptable compromise. In cases where the induced

microstructure was stronger than the base material, a second reduced gauge section was machined in the specimen prior to testing to ensure specimen fracture in the region of interest. This revised specimen geometry is shown in **Figure 3**.

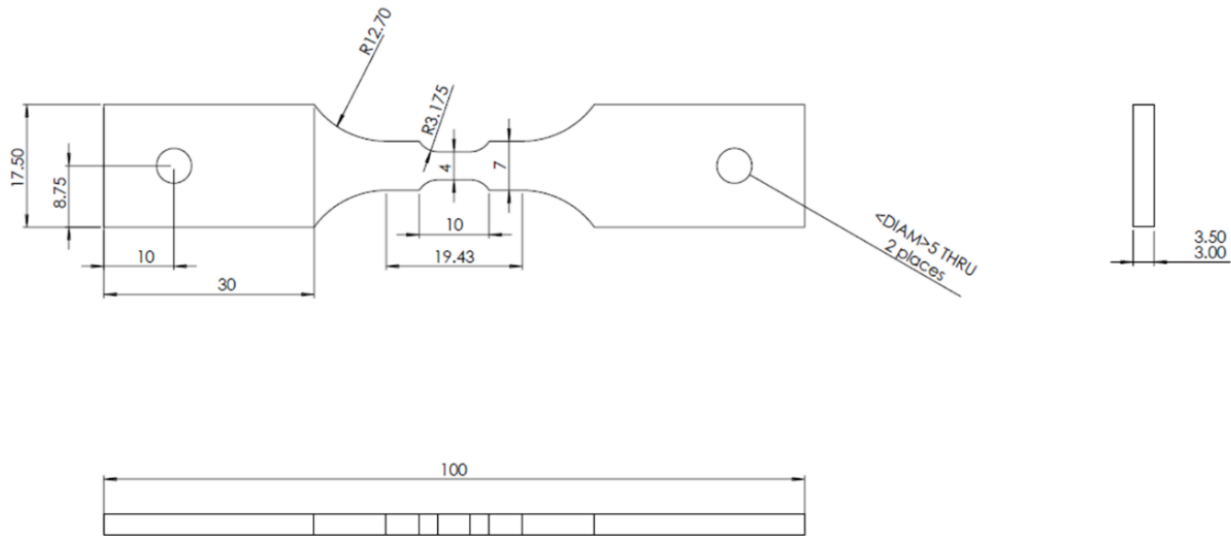


Figure 3. Specimen dimensions for Gleeble-based mechanical testing of HSLA-100 steel for a double-reduced gauge section (dimensions in mm).

Thermal cycling and subsequent tensile testing were performed using the apparatus's "Pocket Jaw" setup with minimal contact stainless steel grips used to fixture the specimen. These grips were selected to minimize the longitudinal thermal gradient in the gauge length of the specimens during testing. Graphite foil was inserted between the specimen and the grips to further minimize the thermal gradient. Strain in the specimens was measured using a contact longitudinal extensometer, and the initial gauge length for the tests varied between 8 and 10 mm (0.31 and 0.39 in.). Elevated temperature tension tests were performed in an argon atmosphere. Preliminary testing as part of the DH36 test program [5] indicated that for this setup, the temperature variation across the initial gauge length was 10 to 30 °C (18 to 54 °F). The typical experimental setup for the dilatometry testing is shown in **Figure 4**.

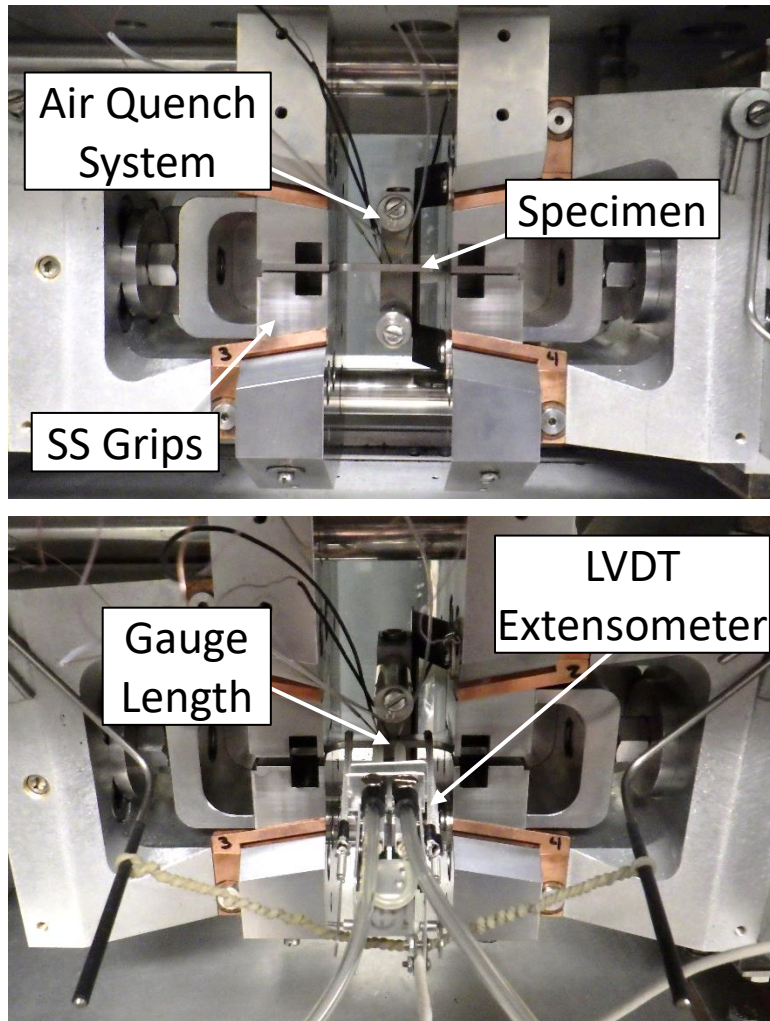


Figure 4. Photographs of the Gleeble-based mechanical testing experimental set-up.

Fabrication of Welded Specimens

Additionally, two sets of HSLA-100 plates were welded together at Ingalls and sent to OSU to investigate the plate, weld, and heat-affected zone (HAZ) microstructures. The first set of plates were welded using submerged arc welding (SAW) in a two-sided butt joint configuration, as shown in **Figure 5a**. The second set of plates were welded using flux cored arc welding (FCAW) in a two-sided tee-joint configuration, as shown in **Figure 5b**. Welding parameters for both scenarios are given in **Table 2**. These weldments enabled correlation of the microstructures generated through thermal simulations for the CCT curves with those produced from arc welding. Each weldment is representative of two primary types of joints used at Ingalls for structural welds: seaming butt joints and fillet joint stiffener welds. These joint types were also the focus of larger fabrication efforts described in other tasks within the greater LIFT project as described in [14].

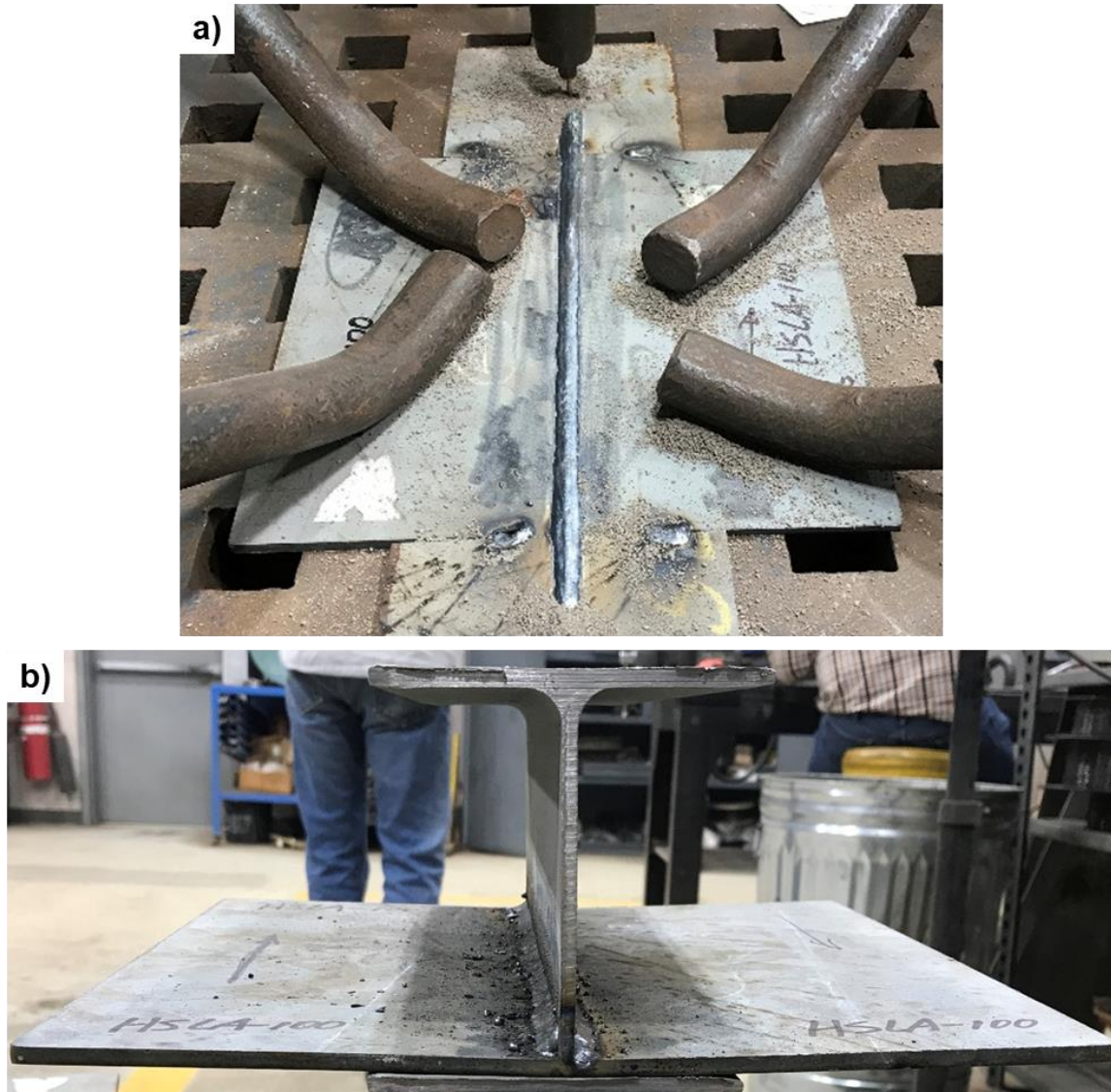


Figure 5. Representative a) butt and b) tee joint weldments of HSLA-100 material investigated for plate, weld, and HAZ microstructures.

Table 2. Nominal Welding Parameters used to Fabricate HSLA-100 Butt and Tee Joints

	Butt Joint	Tee Joint
Welding Process	Submerged arc (SAW)	Flux cored arc (FCAW)
Current (A)	325 / 350 (1 st / 2 nd Pass)	160-165
Voltage (V)	30	27
Travel Speed (mm/s [in/min])	10.6 (25)	6.35 (15)
Heat Input (kJ/mm [kJ/in])	0.92 / 0.99 (23.4 / 25.2)	0.68-0.70 (17.3-17.8)
Consumable Designation(s)	MIL-E-23765/2E; MIL-100S-1	AWS A5.20 E71T-1
Filler Wire Diameter (mm [in])	3.175 (0.125)	1.32 (0.052)
Interpass Temperature, Max. (°C [°F])	38 (100)	54 (130)

Microstructural Analysis

To quantify and characterize the HSLA-100 weldment microstructures, a cross-section of each of the weldments represented in **Figure 5** was analyzed. Each specimen was metallographically prepared to a final polish of 0.05 μm using standard techniques and etched by immersion in 4% Picral (4 g picric acid dissolved in 100 mL ethanol) for approximately 10 seconds followed by immersion in 2% Nital (2 mL nitric acid in 98 mL of ethanol) for 5 seconds. Metallographic preparation was followed by light optical microscopy (LOM) and scanning electron microscopy (SEM) analysis. Vickers microhardness values measured using a load of 200 g (7.05 oz.) were taken from the fusion zone through the HAZ to the base material for both weldments.

Thermally cycled specimens from the HAZ CCT diagram development were metallographically prepared using the same procedure. Identification and phase fraction measurement of the microstructural constituents in each specimen were evaluated using image analysis through LOM and SEM. Vickers microhardness testing was also used to determine the hardness of the constituent(s) in each CCT specimen. This analysis facilitated proper CCT analysis, provided phase fraction input for the HSLA-100 material property database, and helped determine which thermal cycles were the most appropriate for application in the mechanical testing portion of the program described above.

RESULTS AND DISCUSSION

Chemical Composition

Table 3 shows the averaged results of three base material chemistry measurements for the HSLA-100 plate, plus manufacturer's plate certification values (shown in **Appendix A**), the NAVSEA Tech Pub 300 HSLA-100 specifications for Composition 1 grade [4], and results from a study conducted as part of a Navy Manufacturing Technology (ManTech) program with the Naval Metalworking Center from the mid-2000s [15]. This data is labeled "CTC" for Concurrent Technologies Corporation, where the testing was conducted for a plate of 25.4 mm (1.0 in.) nominal thickness. As expected, the measured chemical composition values generally agreed with the manufacturer's plate certification and were well within the NAVSEA specifications. The carbon equivalency number (CEN) was calculated according to Yurioka *et al.* [16]. The individual measurements made by OSU to obtain the average composition values are located in **Appendix A**.

Solidus and Liquidus Analysis

Solidus and liquidus temperatures were not experimentally measured for HSLA-100 base material as part of this project. The CTC report [15] states a measured solidus temperature of 1510 $^{\circ}\text{C}$ (2750 $^{\circ}\text{F}$) and liquidus temperature of 1525 $^{\circ}\text{C}$ (2777 $^{\circ}\text{F}$).

Table 3. Chemical Composition of HSLA-100 Material (wt.%)

Type	C	Mn	P	S	Si	Ni	Cr	Mo	Cu
Measured Avg.	0.031	0.88	0.007	0.0009	0.28	1.94	0.59	0.32	1.13
Plate Certificate	0.04	0.91	0.007	0.002	0.29	1.66	0.60	0.32	1.18
Tech Pub 300 [4]	<0.06	0.75 – 1.15	<0.020	<0.004	<0.40	1.50-2.00	0.45-0.75	0.30-0.55	1.00-1.30
CTC [15]	0.05	0.90-0.91	0.005	0.002	0.24	1.59-1.61	0.56	0.37-0.38	1.13-1.14

Type	Nb	Al	Ti	As	Sb	V	Sn	N	Fe	CEN [16]
Measured Avg.	0.027	0.028	0.002	---	---	0.003	0.0012	---	Bal	0.298
Plate Certificate	0.028	0.024	0.002	0.0040	0.0020	0.001	0.011	0.0064	Bal	0.308
Tech Pub 300 [4]	0.02-0.06	>0.015	<0.02	<0.025	<0.025	<0.03	<0.030	---	Bal	---
CTC [15]	0.029-0.030	0.038-0.041	0.002	0.0030	0.0010	0.02-0.03	0.007-0.008	0.0090-0.0093	Bal	0.322

Base Metal Microstructure

The microstructure of the HSLA-100 base metal is shown in the light optical micrograph of **Figure 6**. The microstructure is entirely quasipolygonal ferrite. As the base metal was subjected to a precipitation aging heat treatment by the manufacturer, the presence of ϵ -Cu precipitates is presumed, but they could not be resolved via LOM. The average Vickers microhardness of the base metal was 257 ± 9.7 HV₃₀₀. In comparison, Yue *et al.* [17] measured HSLA-100 base metal to be 284 HV, albeit with a 1 kg load instead of 300 g load as used in this testing.

Observing the HSLA-100 base metal in both the longitudinal and transverse planes revealed irregular grains with no evidence of anisotropy. The grain size was measured using the “intercept method” detailed in ASTM E1382 [18]. Using this technique, a circle is drawn at random locations within a micrograph, and the number of times a grain boundary intercepts that circle is used to calculate the average grain size. Using a circle instead of a line ensured that the presence of anisotropy (*e.g.*, rolling texture) did not bias results. Measurements were taken four times on a sample of base metal with the average ASTM grain size calculated to be $G = 11.24$.

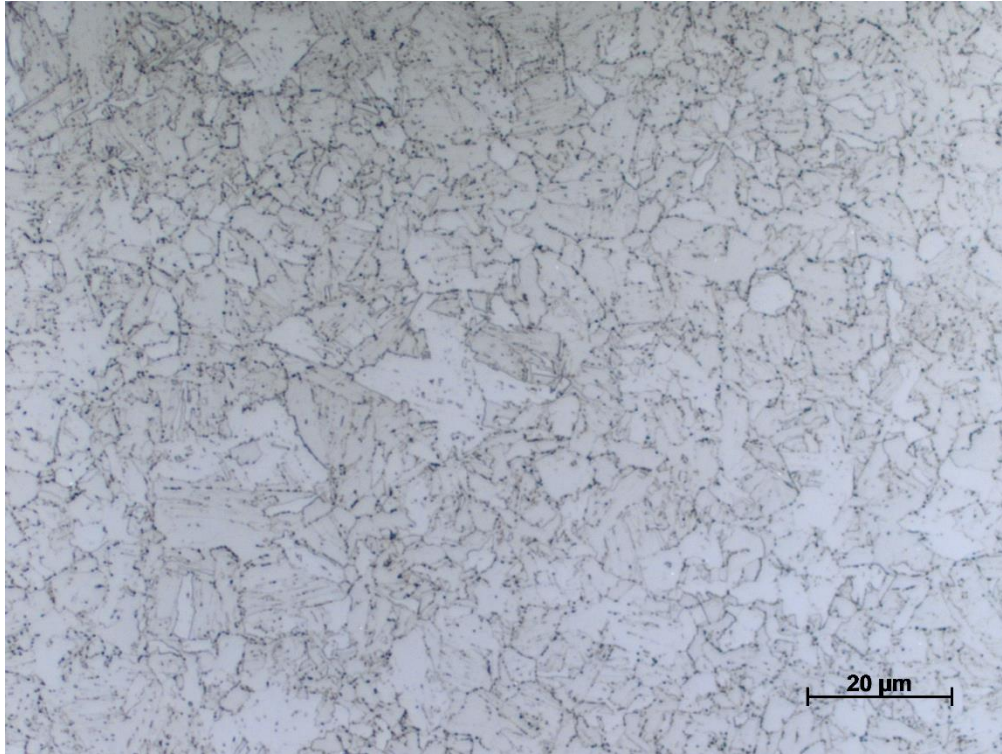


Figure 6. Representative micrograph of HSLA-100 steel plate base metal microstructure at 1000x magnification using LOM.

Heat Affected Zone Phase Transformation Analysis

Dilation Curve Analysis Method

Figure 7 shows a representative on-heating portion of a Gleeble-produced dilatometry curve generated by NSWCCD. The black curve (left axis) represents the change in sample diameter (*i.e.*, dilation) with temperature, with non-linearity in the black dilation curve corresponding to a phase transformation. Instances at which non-linearity occurs can be highlighted by graphing the derivative of the dilation curve with respect to temperature, shown by the red curve (right axis). Simple linear extrapolations of the black dilation curve are shown by the blue lines as a secondary method for pinpointing the temperatures at which nonlinearity occurs. In this case, the transformation of interest is that of the HSLA-100 base metal microstructure to austenite.

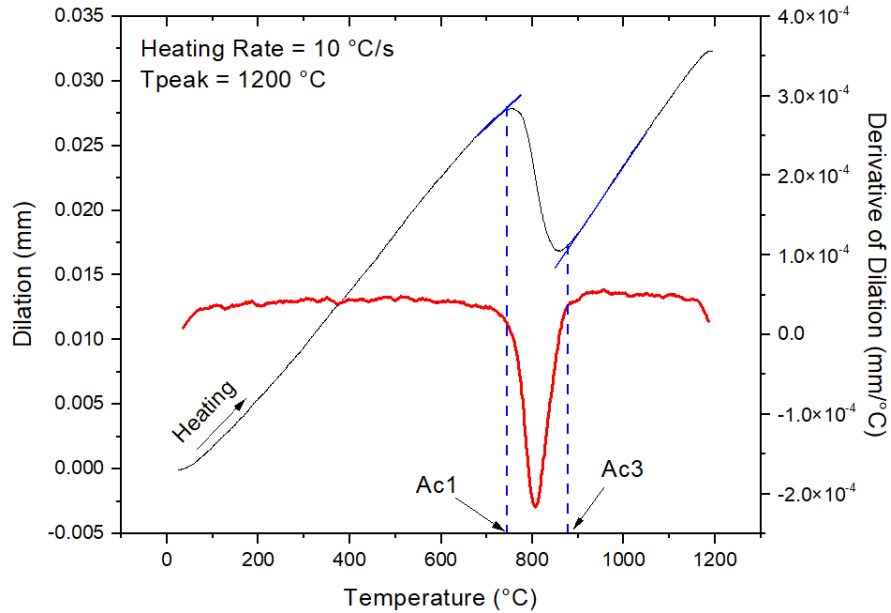


Figure 7. Representative on-heating dilatometry curve for HSLA-100 steel, showing the linear extrapolation and derivative curve methods for evaluating the ferrite to austenite reaction. Black curve, left axis: dilation data. Red curve, right axis: derivative of dilation data. Blue lines: extrapolation lines for determining transformation start (A_{c1}) and finish (A_{c3}) temperatures.

Two methods for extracting start and finish temperatures for phase transformations from Gleeble dilatometry data are commonly used. The first method involves superimposing a straight line of matching slope along the low temperature portion of the dilation curve and extrapolating it past the transformation. The point at which the experimental data begins to deviate from the straight line is then taken as the transformation start temperature. The same technique is then used to find the transformation finish temperature, with the straight line being extrapolated from the high-temperature portion of the curve after the transformation. The second method involves calculating and plotting the derivative of the dilation curve. Then the points at which the derivative begins to deviate from a constant value are taken as the transformation start and finish temperatures. Both methods for determining phase transformation temperatures are inherently somewhat subjective, and both also have advantages and disadvantages. The linear extrapolation method is faster and easier to interpret but is difficult to use when multiple transformations occur. The derivative method is more quantitative and can more easily distinguish multiple transformations but can be difficult to interpret when the dilation data is noisy. For this work, the linear extrapolation method was chosen as the primary method of data analysis, and the derivative method was used as a complementary technique for distinguishing concurrent phase transformations. Both methods are shown in **Figure 7**, where the derivative curve is displayed in red and the linear extrapolations are displayed in blue.

Austenite Transformation Temperature Measurement

Figure 8 presents the variation in austenite transformation behavior as a function of heating rate for HSLA-100 base material. As shown, the austenite transformation start temperature (A_{c1}) increases significantly as heating rate increases toward 200 °C/s (360 °F/s). This is a consequence of thermal diffusion during heating outpacing the mass diffusion required for the transformation to take place. In contrast, the austenite transformation finish temperature (A_{c3}) remains more stable across the

experimental heating rate range. Researchers who have investigated similar behavior in other ferrous materials have associated heating rate dependencies of the austenite transformation with those of the controlling diffusion mechanism (*i.e.*, volume carbon diffusion or grain boundary substitutional element diffusion), the ferrite recrystallization process, and/or austenite nucleation and growth rates [19] [20] [21]. These data are important for the refinement of welding simulation results because different regions of a weldment and its HAZ are subject to significantly different heating rates during the welding process. The on-heating transformation behavior must be incorporated in order to accurately predict which areas around the weld will transform to austenite and will therefore be subject to re-transformation (and associated changes in mechanical properties and residual stresses) during cooling. Data from CTC as part of the Navy ManTech program [15] and from Yue *et al.* [17] are included for comparison. It should be noted that the Yue data was an average value across 12 specimens all heated at 200 °C/s (360 °F/s). The raw data points for **Figure 8** can be found in **Table 9** within **Appendix B**.

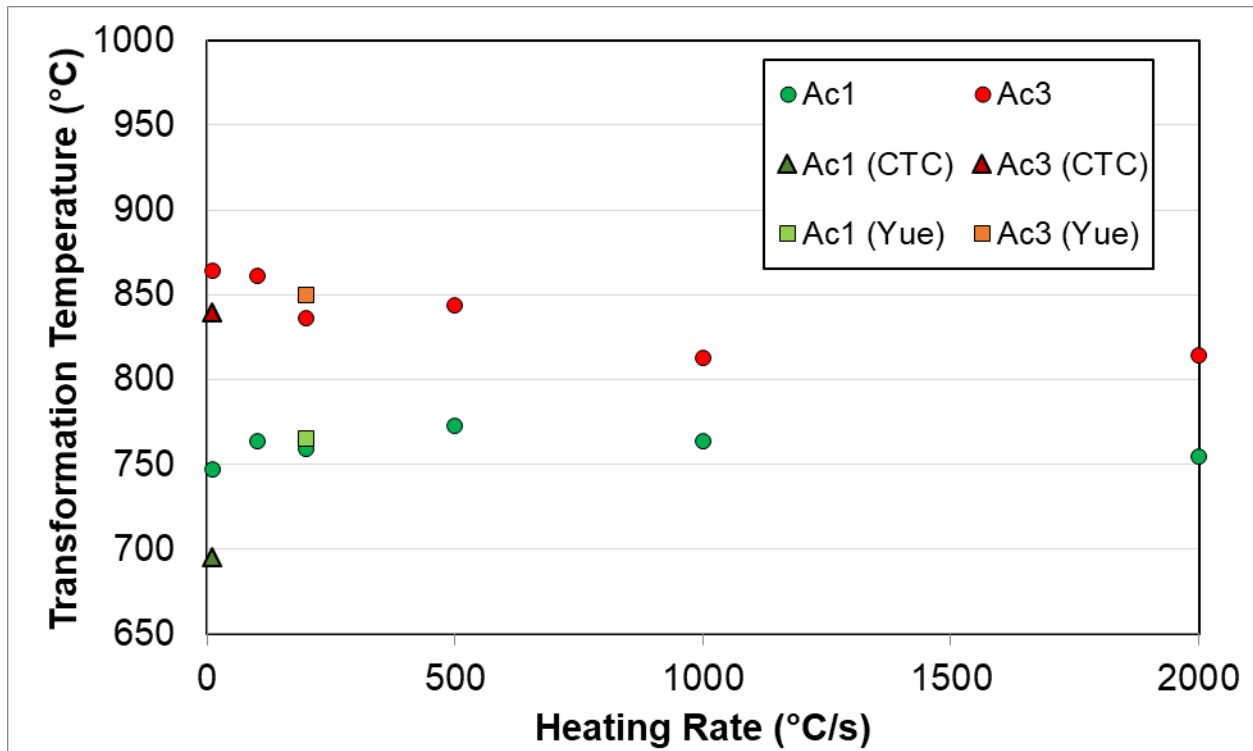


Figure 8. Variation in austenite transformation start and finish temperatures with heating rate for HSLA-100 material.

Continuous Cooling Transformation Diagrams

CCT diagrams assembled from dilatometry of HSLA-100 thermally cycled to peak temperatures representative of the four selected HAZ regions are given in **Figures 9-12**. The austenite transformation temperatures described above resulted in selection of an ICHAZ simulation temperature of 790 °C (1454 °F) for HSLA-100, which was 35 °C (95 °F) lower than that used for HSLA-65 [6] and HSLA-80 [7], and 85 °C (185 °F) lower than the temperature used for DH36 [5]. The A_{c1} and A_{c3} temperatures labeled on the CCT diagrams are averages calculated from the individual A_{c1} and A_{c3} values for all of the CCT specimens. The black curves are the actual specimen cooling curves. The target cooling rates for all specimens except those cooled at 100 and 200 °C/s (180 and 360 °F/s) were maintained through the on-cooling phase transformations. The latent heat released during low temperature transformation slowed the

cooling rates of both the 100 °C/s (180 °F/s) and the 200 °C/s (360 °F/s) tests for all peak temperatures. As a result the target cooling rate was maintained until the start of the transformation, but was slowed as the transformations occurred for 100 and 200 °C/s (180 and 360 °F/s) tests. The raw data for these figures are given in **Table 10-13** of **Appendix B**, and the individual dilation curves are given in **Figures 38-61** of **Appendix B**.

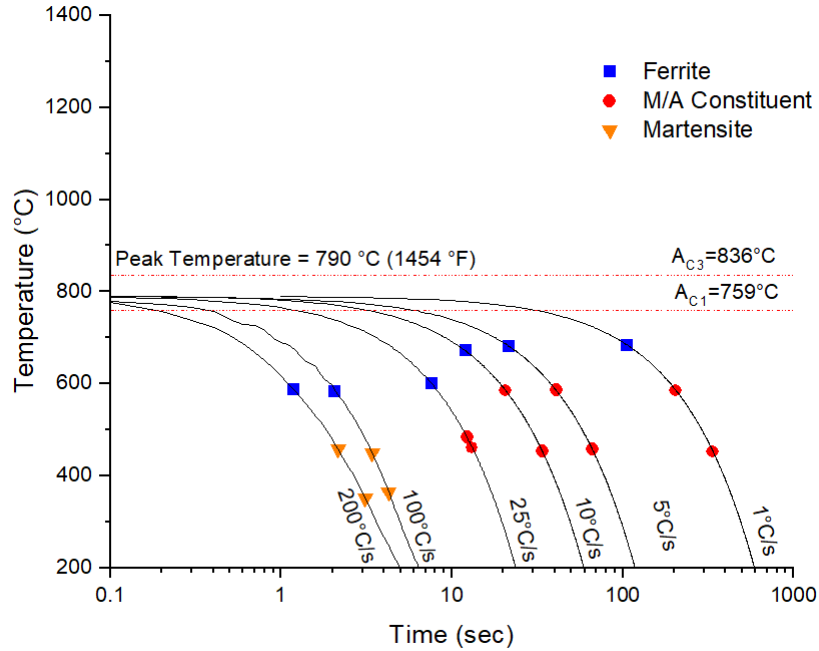


Figure 9. CCT diagram for HSLA-100 heated to peak temperature of 790 °C (1454 °F).

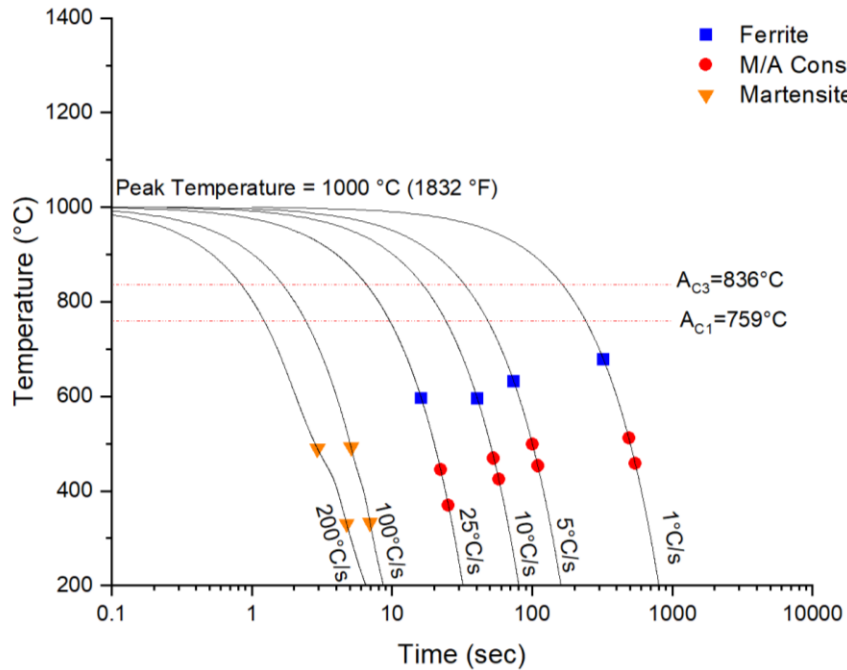


Figure 10. CCT diagram for HSLA-100 heated to peak temperature of 1000 °C (1832 °F).

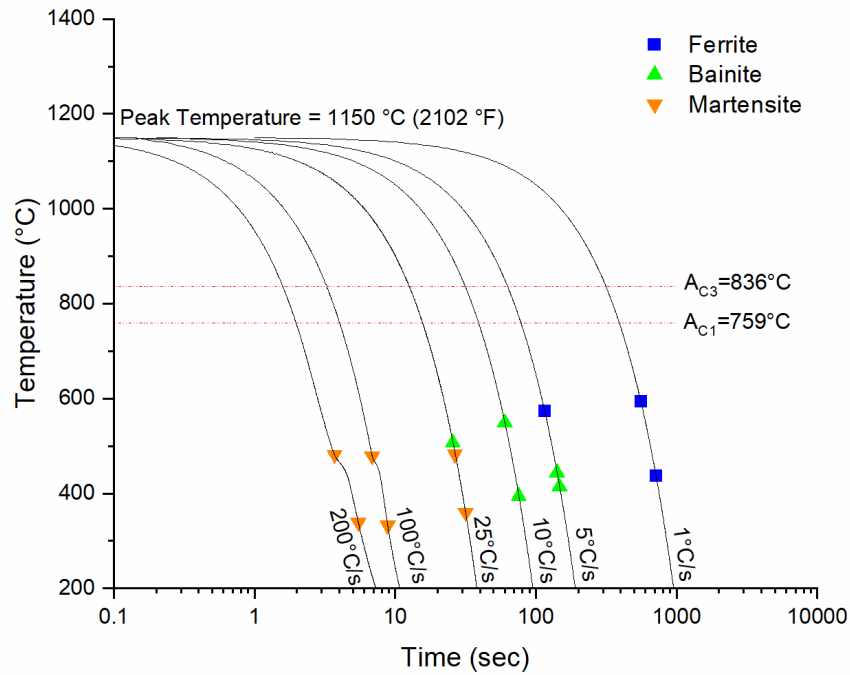


Figure 11. CCT diagram for HSLA-100 heated to peak temperature of 1150 °C (2102 °F).

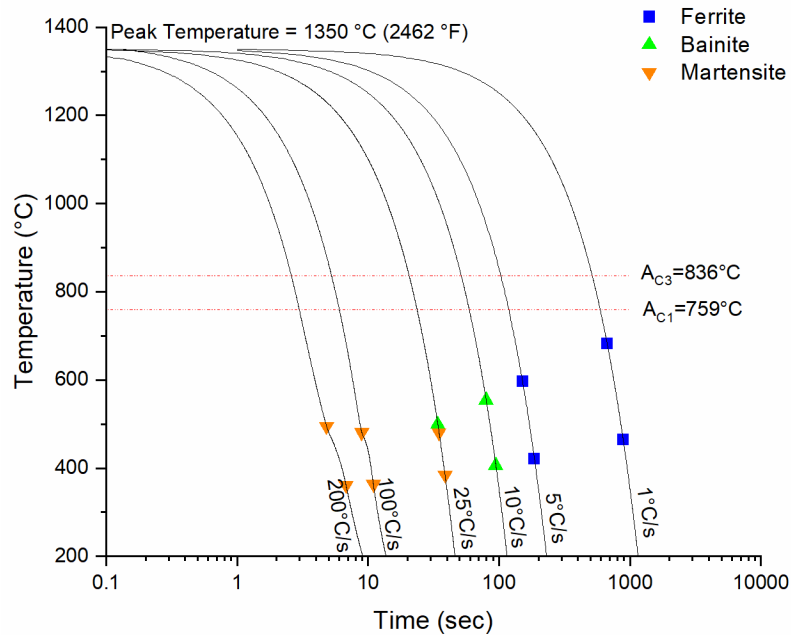


Figure 12. CCT diagram for HSLA-100 heated to peak temperature of 1350 °C (2462 °F).

The colored symbols in **Figures 9-12** correspond to the start and finish temperatures for the various on-cooling phase transformations. Simulated HAZ regions were subject to up to three regimes of on-cooling transformation start temperatures across the cooling rate range assessed in this work as shown in **Figure 13-Figure 15**. The first occurred at high temperatures and was associated with ferrite

formation, which was observed for slowly-cooled samples at every peak temperature tested, as illustrated below in **Figure 13**. In general, ferrite start transformation temperatures were suppressed as cooling rate increased, which is expected for a diffusion-based transformation mechanism. Though ferrite was not represented for every combination of cooling rate and peak temperature, for a given cooling rate, transformation temperatures decreased as the peak temperature increased.

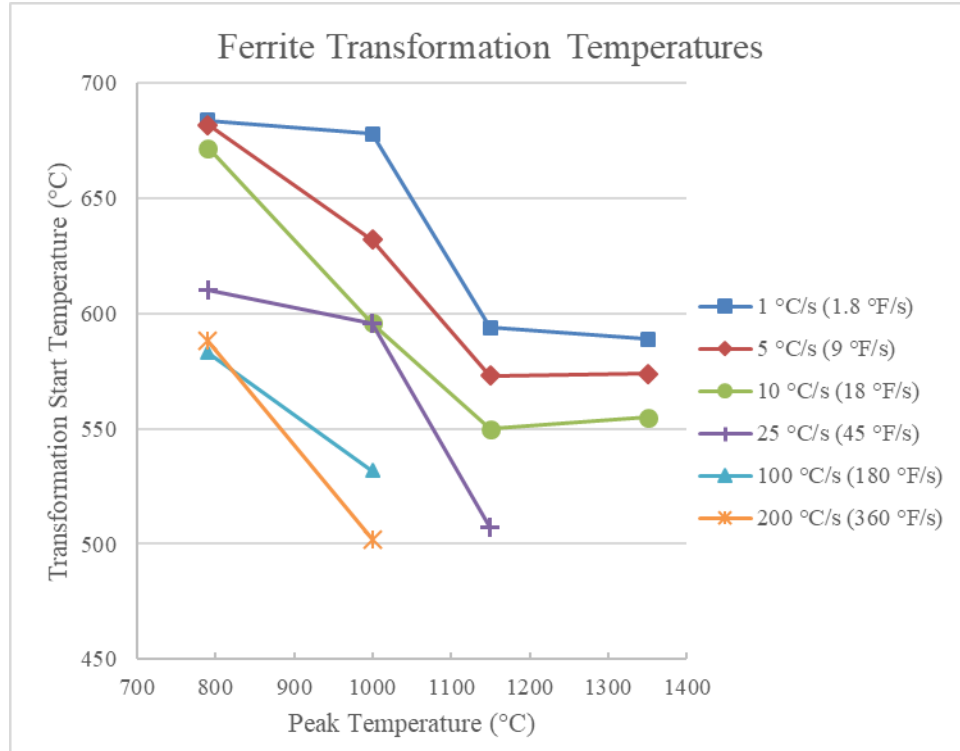


Figure 13. Variation of start temperature for the ferrite transformation shown in **Figures 9-12**.

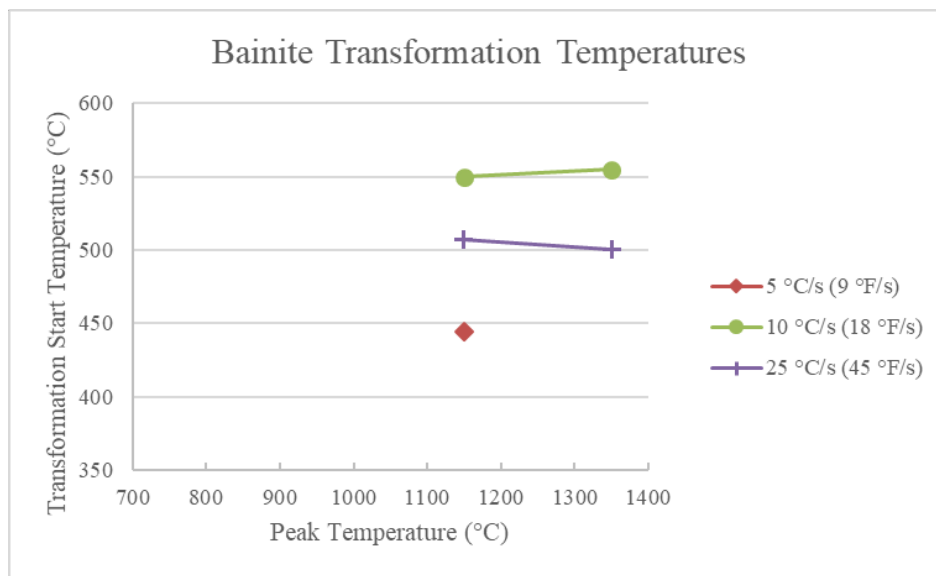


Figure 14. Variation of start temperature for the bainite transformation shown in **Figures 9-12**.

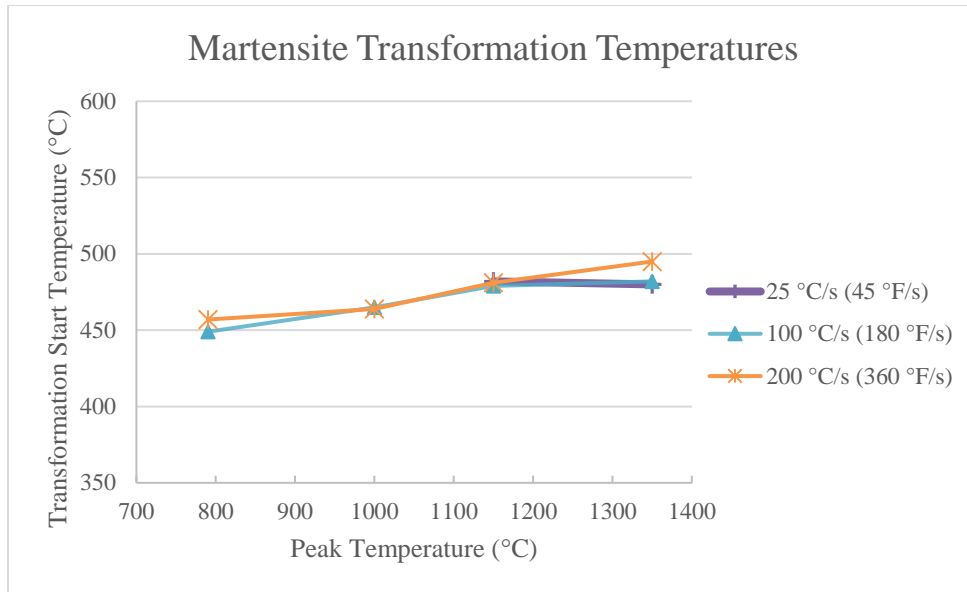


Figure 15. Variation of start temperature for the martensite transformation shown in **Figures 9-12**.

Bainite was present in a small number of samples, appearing only at moderate cooling rates (from 5-25 °C/s [9-45 °F/s]) and in samples brought to high peak temperatures, as shown in **Figure 14**. Martensite was a more common transformation product in the low temperature regime, only present in samples cooled at rates of 25 °C/s (45 °F/s) and higher but represented in each simulated HAZ sub-region, illustrated in **Figure 15**. As shown, M_s temperature rose slightly with increasing peak temperature, falling between 449 and 495 °C (840 and 923 °F).

In order to confidently establish the identities of the on-cooling phase transformations, LOM was performed on all dilatometry specimens, and select specimens were analyzed via SEM. Micrographs collected from the dilatometry specimens are given in **Figures 62-67** of **Appendix C**. Additionally, the measured microhardness for each specimen is given in **Figure 16** and **Table 14** of **Appendix D**. For this discussion, the following definitions for the morphology of microstructural constituents are adopted, based on references [22] [23] [24] [25] [26]. The typical definitions for crystal structure and composition of the constituents are also assumed.

Primary ferrite (F_P) – Carbide-free grain boundary or intragranular allotriomorphic or idiomorphic ferrite

Acicular ferrite (AF) – Fine, interlocking structure formed by impingement of multiple Widmanstätten plates growing from intragranular inclusions

Martensite-austenite constituent (M/A) – Structure represented by a combination of martensite and residual austenite

Bainite (B) – General term for fine aggregates of ferrite laths or plates and cementite particles

Lath martensite (M_L) – Martensite laths with highly dislocated substructure which are grouped into larger packets

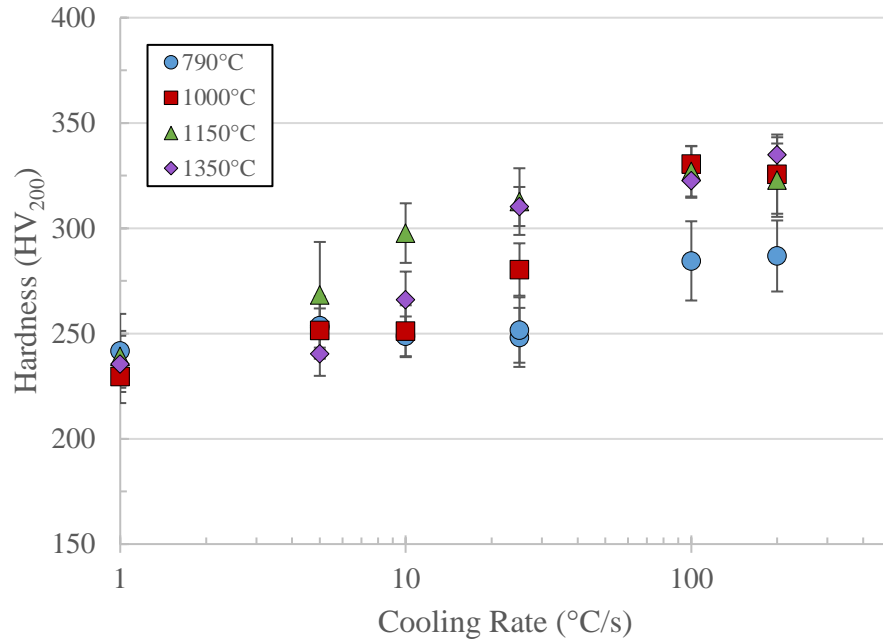


Figure 16. Measured Vickers microhardness for HSLA-100 dilatometry specimens as a function of peak temperature and cooling rate. Error bars are one standard deviation. Values are the average of 5-65 indents.

Representative micrographs of all CCT specimens heated to 790 °C (1454 °F) are shown in **Figure 62 of Appendix C**. This temperature falls between A_{c1} and A_{c3} (759 and 836 °C [1398 and 1537 °F], respectively) and was chosen in order to achieve partial transformation to austenite prior to cooling. This partial transformation is expected to occur via austenite nucleation at the triple points and grain boundaries as the ferrite equilibrium temperature is exceeded [24].

Slowly cooled samples heated to ICHAZ peak temperature did not retain microstructures from the original base material. The samples subjected to 1, 5, 10, and 25 °C/s (1.8, 9, 18, and 45 °F/s) cooling rates (shown in **Figure 62a-d**) all exhibited a mixture of primary ferrite with quasipolygonal morphology and M/A constituent. Determination of the proportions of martensite and austenite in the M/A constituents could not be determined through optical microscopy and was not attempted with electron microscopy. Ferrite transformation start temperatures dropped from 684 °C (1263 °F) to 601 °C (1114 °F) as cooling rates of these samples increased from 1 to 25 °C/s (1.8 to 45 °F/s). This depression of transformation temperatures for diffusion-based transformations is expected as cooling rates increase. A secondary transformation was detected at lower temperatures, presumed to correspond with formation of M/A constituent. For all four samples this began at approximately 585 °C (1085 °F), but finish temperatures for the slower cooling rates of 1-25 °C/s (1.8-45 °F/s) fell within a narrow range of 452 and 461 °C (846 and 862 °F). Due to the fine and fragmented morphology of the M/A constituent shown in the micrographs, it is difficult to quantify fraction ferrite, but there does not appear to be a significant difference in the proportion of ferrite present in the samples cooled at 5-25 °C/s (9-45 °F/s). This is supported by microhardness, as all three samples fell within the narrow range of 249-254 HV₂₀₀. The etching response of the M/A constituent bears a close resemblance to martensite, but the low cooling rates coupled with low microhardness values (between 242 and 254 HV₂₀₀) support identification as M/A constituent. *SYSWELD* does not explicitly account for M/A constituent, so phase fractions of these specimens were reported to be entirely ferrite, as shown in **Table 4**.

Table 4. Measured Phase Fraction of HSLA-100 CCT Specimens Thermally Cycled to a Peak Temperature of 790 °C (1454 °F)

Cooling Rate		Peak Temperature = 790 °C (1454 °F)		
°C/s	°F/s	F + M/A	B	M
1	1.8	1	0	0
5	9	1	0	0
10	18	1	0	0
25	45	1	0	0
100	180	0.64	0	0.36
200	360	0.38	0	0.62

A large number of precipitates were present in all samples heated to intercritical temperatures, particularly concentrated in regions adjacent to M/A constituent. It is unclear whether these precipitates persisted from the base material or if additional precipitates had formed on-heating. Ferritic regions were comparatively precipitate-free, indicating dissolution during thermal cycling. The identity of the precipitates was not explored, though their visibility in optical micrographs suggests they are some form of carbides or carbonitrides. ϵ -Cu precipitates in HSLA-80 have been reported to be less than 5 nm in size [27], and it is presumed that the same precipitates in HSLA-100 are on a similar scale. A study by Sun *et al.* examined the effect of aging time on precipitate size in a Cu-bearing marine steel, similar to HSLA-100 but with slightly higher Cu and Ni content [28]. This steel was subjected to controlled rolling thermomechanical processing conditions consistent with those used to produce HSLA steels. The authors found that when this material was subjected to isothermal aging at 500 °C (932 °F) for 1 and 3 hours, Cu precipitates with average size of 5.6 and 19.3 nm, respectively, could be identified via TEM. Any precipitates that may have formed during a 0.5 hour aging regimen were too small for positive identification [28]. A study by Das *et al.* examined another steel similar to HSLA-100 with slightly higher than allowable Cu and Ni content, but without the aging step carried out by Sun *et al.* [29]. Das *et al.* used TEM to find that when the material was cooled at 0.68 °C/s (33 °F/s) from 800 °C (1472 °F), the average size of Cu precipitates fell between 10-18 nm, with the largest identified having a size of 50 nm. The extremely small Cu precipitate size reported in various literature makes it unlikely that any precipitates shown in the simulated HAZ optical or SEM micrographs were ϵ -Cu. Any volumetric change associated with precipitate dissolution was not large enough to identify on dilation curves.

For HSLA-80, the dissolution of second phases (including ϵ -Cu) was determined in tests at CTC to finish at 880 °C (1616 °F) at slow heating rates [30]. Further, a study by Bhagat *et al.* indicated that under isothermal aging conditions, dissolution of copper precipitates in an HSLA steel sample began at 650 and 700 °C (1202 and 1292 °F) after being held for 20 and 4 minutes, respectively, as evidenced by an increase in experimentally measured resistivity [27]. The sample studied by Bhagat *et al.* had a composition that was similar to that of HSLA-100, but the Ni content of 3.39 wt.% was more representative of that allowed for thick plate than the 1.94 wt.% measured in the material analyzed in this report. Thermo-Calc 2020b and the TCFE9 database [31] were used in this study to calculate an equilibrium ϵ -Cu dissolution temperature of approximately 700 °C (1292 °F) for the HSLA-100 composition reported in **Table 3**. It is therefore unlikely that ϵ -Cu precipitates persisted at the 790 °C (1454 °F) ICHAZ peak temperature, with the possible exception of rapidly cooled samples, and complete dissolution was expected for all higher peak temperature samples. As is the case with M/A constituent, precipitates are not considered in *SYSWELD*, so despite their presence these microstructures are simply described as ferrite.

The average size of the M/A constituent appeared to decrease as cooling rate increased. This is consistent with reduced time for prior austenite grain growth. Evidence of M/A constituent banding was present in the 1 °C/s (1.8 °F/s) and was slightly discernible in the samples cooled at 5, 10, and 25 °C/s (9, 18, and 45 °F/s). M/A constituent formation requires local carbon enrichment. Austenite has a significantly higher solubility for carbon than ferrite does, so partial transformation of the ferritic base material into austenite would have encouraged diffusion of carbon from ferritic regions to austenitic ones. Further, banding of alloying elements or impurities is a common phenomenon in rolled plate. Calculations performed using Thermo-Calc 2020b and the TCFE9 thermodynamic database [31] predict that the chemical potential of carbon will be lower in areas where remnant macrosegregation results in a higher than nominal concentration of substitutional alloying elements, further driving diffusion towards those areas.

Transformation finish temperatures for the samples cooled at 100 and 200 °C/s (180 and 360 °F/s) extend significantly below those of the more slowly cooled specimens. It is likely that in addition to the ferrite observed in samples cooled at and below 25 °C/s (45 °F/s), phases such as bainite or martensite are present. Other studies have found an M_s temperature of approximately 420 °C (788 °F) [32] [33]. This is lower than the temperature range at which martensite was observed to begin transformation, even for higher peak temperatures. This discrepancy can be explained by chemical composition. Though HSLA-100 was studied in each case, most literature sourced material from thicker material than the 4.76 mm (3/16-in.) thick plates examined in this report. In contrast with the measured 1.94 wt.% Ni in the samples studied here, thick sections have a Ni content between 3.35-3.65 wt.% as by Tech Pub 300 [4]. The resulting difference in carbon equivalent is significant, as calculated using the formula developed by Yurioka *et al.* [16]. The material studied in this report had a carbon equivalent of 0.30, compared to values of 0.39 and 0.44 reported by Shome *et al.* and Spanos *et al.*, who each reported an M_s of 420 °C (788 °F) [32] [33]. The compositions studied in literature have more austenite stabilizing elements, which allow austenite to persist at lower temperatures before transforming to martensite, decreasing M_s . Therefore, it is likely that M_s temperatures for the HSLA-100 composition in this report are simply higher than those reported in other studies due to lower proportion of austenite stabilizing alloying elements.

Various constitutive equations for predicting the start temperatures for bainite and martensite transformations based on alloy chemistry are available in the literature [34] [35]. Such models are generally oversimplifications and often are only accurate for alloys similar to those used to create them, but they can act as a guide for reasonable temperatures at which to expect formation of intermediate and low temperature phases. As such, the models developed by Capdevilla *et al.* [36] and Kirkaldy [37] were applied to the measured HSLA-100 composition given in **Table 3**:

$$M_s = 491.05 - 302.6w_C - 30.6w_{Mn} - 16.6w_{Ni} - 8.9w_{Cr} + 2.4w_{Mo} - 11.3w_{Cu} + 8.58w_{Co} + 7.4w_W - 14.5w_{Si} \quad (5)$$

$$B_s = 656 - 57.7w_C - 75w_{Si} - 35w_{Mn} - 15.3w_{Ni} - 32w_{Cr} - 41.2w_{Mo} \quad (6)$$

where M_s ≡ martensite start temperature (°C)
 B_s ≡ bainite start temperature (°C)
 w_i ≡ concentration of element i (wt%)

From **Equations 5** and **6**, the M_s and B_s temperatures for HSLA-100 are predicted to be 401 °C (755 °F) and 541 °C (1005 °F), respectively. The same formulas predict M_s temperatures of 369 and 360 °C (696 and 680 °F) for the more highly-alloyed literature compositions, which both reported an experimental M_s temperature of 420 °C (788 °F) [32] [33]. From this it can be concluded that **Equation 5** substantially underestimates transformation temperatures for this class of material.

Two transformations were detected in the dilation curves for the samples cooled at 100 and 200 °C/s (180 and 360 °F/s). The first, higher temperature transformations began at 583 and 588 °C (1081 and 1090 °F) and finished at 449 and 457 °C (840 and 855 °F) for the two samples, respectively. Though this falls within the predicted bainite temperature regime, optical and SEM micrographs in **Figures 62 and 63** of **Appendix C** revealed only polygonal ferrite and martensite, suggesting that these transformations were associated with ferrite formation. The second, lower temperature transformations took place over 449 to 364 °C (840 to 687 °F) when cooled at 100 °C/s (180 °F/s) and over 457 to 352 °C (855 to 666 °F) when cooled at 200 °C/s (360 °F/s). These low temperature transformations were associated with martensite, as evidenced by the high microhardness values (285 and 287 HV₂₀₀) and consistency with measured M_s for higher peak temperature samples.

The next simulated HAZ region was the FGHAZ, with a peak temperature of 1000 °C (1832 °F). Representative micrographs are presented in **Figures 64 and 65** of **Appendix C**, with measured phase fractions reported in **Table 5**. Samples cooled at 1 to 25 °C/s (1.8 to 45 °F/s) were all composed of a mixture of polygonal ferrite and M/A constituent. The slowly cooled samples spent more time in the high temperature regime that allowed for precipitate dissolution and grain growth, which is reflected in the coarse microstructures in the sample cooled at 1 °C/s (1.8 °F/s) and progressively finer microstructures and higher number of precipitates as cooling rate increased to 25 °C/s (45 °F/s). Average microhardness increased with cooling rate, from 230 to 280 HV₂₀₀. In ICHAZ samples, the presence of M/A constituent was accompanied with a corresponding distinct inflection point in dilation curves. This was not the case for samples heated to higher peak temperatures. It is likely that time spent at high peak temperatures allowed for more thorough dissolution of alloying elements associated with M/A formation. This could have decreased the extent of M/A formation that formed upon cooling to a volume no longer measurable by the dilatometer. Transformation temperatures followed a strong trend of decreasing as cooling rate increased, with ferrite start temperatures falling steadily from 678 to 592 °C (1252 to 1105 °F) as cooling rate increased from 1 to 25 °C/s (1.8 to 45 °F/s). Ferrite transformation finish temperatures followed the same trend, falling from 458 °C (856 °F) for the sample cooled at 1 °C/s (1.8 °F/s) to 369 °C (696 °F/s) when cooling rate was increased to 25 °C/s (45 °F/s).

Table 5. Measured Phase Fraction of HSLA-100 CCT Specimens Thermally Cycled to a Peak Temperature of 1000 °C (1832 °F)

Cooling Rate		Peak Temperature = 1000 °C (1832 °F)		
°C/s	°F/s	F + M/A	B	M
1	1.8	1	0	0
5	9	1	0	0
10	18	1	0	0
25	45	1	0	0
100	180	0.35	0	0.65
200	360	0.23	0	0.77

Samples cooled at 100 and 200 °C/s (180 and 360 °F/s) were primarily composed of martensite, with optical and SEM micrographs revealing a small proportion of ferrite between martensite packets. Ferrite start transformation temperatures were 532 and 502 °C (990 and 936 °F) for the two samples, respectively. Martensite transformation took place from 465 to 333 °C (869 to 631 °F) when cooled at 100 °C/s (180 °F/s), and from 464 to 331 °C (867 to 628 °F) for the sample cooled at 200 °C/s (360 °F/s). Microhardness was measured to be 331 and 326 HV₂₀₀ for the two specimens. As is expected with the introduction of martensite, these values were substantially higher than the microhardness associated with more slowly cooled samples.

The third peak temperature investigated was also representative of the FGHAZ, but with a slightly higher peak temperature of 1150 °C (2102 °F). Representative micrographs are shown in **Figure 66** in **Appendix C**, with measured phase fractions reported in **Table 6**. It is clear from micrographs of the sample cooled at 1 °C/s (1.8 °F/s) that this peak temperature was sufficient for grain-pinning precipitates to dissolve, as demonstrated by the large prior austenite grains compared to samples with lower peak temperatures. The microhardness of 239 HV₂₀₀ was only slightly higher than samples reaching lower peak temperatures and cooled at the same rate. Despite the larger prior austenite grains, the phases present were the same as those observed in lower peak temperature samples: a mix of polygonal ferrite and M/A constituent. As with FGHAZ samples heated to 1000 °C (1832 °F), only the transformation associated with ferrite was identified on dilation curves. Ferrite transformation took place between 594 and 437 °C (1101 and 809 °F) for the sample cooled at 1 °C/s (1.8 °F/s).

Table 6. Measured Phase Fraction of HSLA-100 CCT Specimens Thermally Cycled to a Peak Temperature of 1150 °C (2102 °F)

Cooling Rate		Peak Temperature = 1150 °C (2102 °F)		
°C/s	°F/s	F + M/A	B	M
1	1.8	1	0	0
5	9	0.87	0.13	0
10	18	0	1	0
25	45	0	0.12	0.88
100	180	0	0	1
200	360	0	0	1

Increasing the cooling rate to 5 °C/s (9 °F/s) introduced bainite to the mixture of polygonal ferrite and M/A constituent. The measured ferrite transformation temperature decreased from 573 to 444 °C (1063 to 831 °F) and bainite formed between 444 and 414 °C (831 and 777 °F). This was accompanied by an increase in microhardness to 268 HV₂₀₀. Further increasing the cooling rate to 10 °C/s (18 °F/s) precluded ferrite formation, leaving only a bainitic microstructure with microhardness of 298 HV₂₀₀. Bainite transformation took place between 550 and 394 °C (1022 and 741 °F). The 25 °C/s (45 °F/s) cooled sample formed a small amount of bainite from 507 to 482 °C (945 to 900 °F) but was primarily composed of martensite, which formed from 482 to 360 °C (900 to 680 °F). Microhardness values reached an average of 313 HV₂₀₀. Samples cooled at 100 and 200 °C/s (180 and 360 °F/s) were entirely martensitic, with microhardness values of 327 and 323, respectively. The martensite transformation took place across essentially the same temperature range – from 479 to 333 °C (894 to 631 °F) and from 481 to 339 (898 to 642 °F) for samples cooled at 100 and 200 °C/s (180 and 360 °F/s), respectively.

The final simulated region was the CGHAZ, with a peak temperature of 1350 °C (2462 °F). Representative micrographs are shown in **Figure 67** in **Appendix C**, with measured phase fractions reported in **Table 7**. Samples cooled at both 1 and 5 °C/s (1.8 and 9 °F/s) were composed entirely of polygonal ferrite and M/A constituent. The higher peak temperature afforded even more prior austenite grain growth than observed in the samples heated to 1150 °C (2102 °F). Microhardness values were 236 and 240 HV₂₀₀. Ferrite transformation began at 589 and 574 °C (1092 and 1065 °F) and completed at 449 and 402 °C (840 and 756 °F) for samples cooled at 1 and 5 °C/s (1.8 and 9 °F/s), respectively.

Table 7. Measured Phase Fraction of HSLA-100 CCT Specimens Thermally Cycled to a Peak Temperature of 1350 °C (2462 °F)

Cooling Rate		Peak Temperature = 1350 °C (2462 °F)		
°C/s	°F/s	F + M/A	B	M
1	1.8	1	0	0
5	9	1	0	0
10	18	0	1	0
25	45	0	0.10	0.90
100	180	0	0	1
200	360	0	0	1

Phases present in samples heated to 1350 °C (2462 °F) and rapidly cooled were the same as those in corresponding samples heated to 1150 °C (2102 °F). The sample cooled at 10 °C/s (18 °F/s) was entirely bainitic, with microhardness of 266 HV₂₀₀ and transformation taking place between 555 and 406 °C/s (1031 and 763 °F/s). Increasing cooling rate to 25 °C/s (45 °F/s) introduced martensite alongside the bainite, raising microhardness to 308 HV₂₀₀ while dropping bainite start temperatures to 555 °C (932 °F) and forming martensite between 480 and 385 °C (896 and 725 °F). The two samples cooled at 100 and 200 °C/s (180 and 360 °F/s) were cooled too rapidly to allow for bainite formation, instead forming entirely martensitic microstructures. Transformation temperatures matched well between the two, with martensite formation taking place between 482 and 362 °C (900 and 684 °F) for the sample cooled at 100 °C/s (180 °F/s) and between 495 and 361 °C (923 and 682 °F) for the sample cooled at 200 °C/s (360 °F/s).

The phase transformation information developed here is critically important for ensuring that weld simulation software can draw on thermo-physical and thermo-mechanical property information from the appropriate phases at the appropriate times during calculations. The results in **Figure 9-15** highlight the importance of developing multiple HAZ-related CCT diagrams.

Weldment Microstructures

Metallographic specimens were removed from both weldments and analyzed in a manner similar to the Gleeble specimens. Discussion of the microstructures present correspond to the HAZ of the second pass for each weldment, as the reheating experienced by the first pass confounded the analysis and do not directly correlate with thermal cycles undergone by Gleeble CCT specimens, making them unsuitable for the intended purpose of experimental validation.

The fusion zone for each joint configuration was a mixture of coarse primary ferrite, acicular ferrite, and unidentified carbides. **Figure 17** presents representative micrographs for the butt joint and tee joint fusion zones. Microhardness values ranged from approximately 190-240 HV₂₀₀.

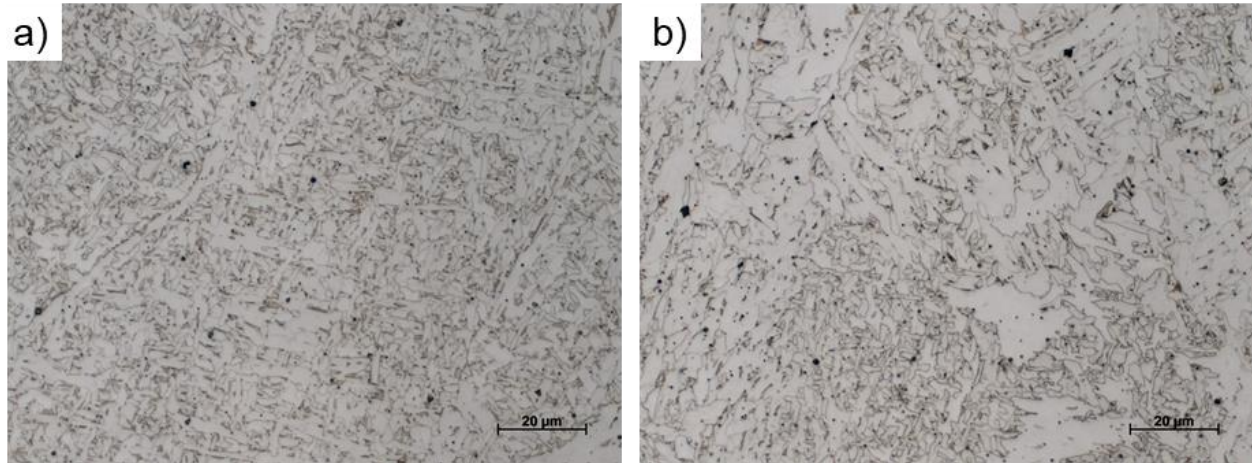


Figure 17. Representative microstructures of the second pass fusion zone for the a) butt joint and b) tee joint configuration.

Representative HAZ microstructures for the second pass of the HSLA-100 butt joint are presented in **Figure 18**. A microhardness map with truncated color scale is provided in **Figure 19**. This limited scale excludes the highest microhardness values, which were present in a single local region and discussed below. The selected color scale shows more granular differences across the weldment and serves as a direct comparison to the color map representing the tee joint microhardnesses shown in **Figure 22**. Each map shows measurements values for indents spaced at intervals of 250 µm in both the horizontal and vertical directions, with numerical values provided in **Table 15** in **Appendix D**. The CGHAZ of the butt joint, shown in **Figure 18a**, was comprised of large grains of coarse bainite, with microhardness values near 240 HV₂₀₀. It appeared that instead of carbides, the aligned secondary phase was instead M/A constituent. The large prior austenite grain size indicated that the region reached sufficient temperatures to dissolve precipitates that would otherwise have pinned the grain boundaries and suppressed grain growth. As distance increased from the fusion line and peak temperature decreased, grain size decreased. This is characteristic of the shift into the FGHAZ, with the region closer to the CGHAZ shown in **Figure 18b**.

Microhardness was higher in the FGHAZ than the CGHAZ, reaching approximately 275 HV₂₀₀ in most regions and achieving local maximums on the order of 350 HV₂₀₀ near the centerline of the plate, where solute banding during the rolling process enriched the microstructure and increased hardenability. Microhardness values above 330 HV₂₀₀ were only identified on the left side of the butt joint, but the relatively low resolution of the microhardness map makes it likely that a corresponding hard region was present on the right side and simply fell between indentations. This hard region is represented in **Figure 20**, which shows a microhardness map with the full range of microhardness values and emphasizes the locally hard region. The microhardness of the FGHAZ generally decreased as distance from the fusion line increased, with values falling to approximately 250 HV₂₀₀ near the ICHAZ. Grain size decreased and microstructure changed from coarse bainite to entirely quasipolygonal ferrite interspersed with islands of M/A constituent, illustrated in **Figure 18c**. The outer edge of the HAZ, adjacent to the base metal, is the ICHAZ, with a representative micrograph shown in **Figure 18d**. Grain size decreased further in the ICHAZ, which was comprised of extremely fine quasipolygonal ferrite interspersed with very small islands of M/A constituent and unidentified precipitates. Microhardness was slightly lower in the ICHAZ than in the FGHAZ, with values near 230-240 HV₂₀₀.

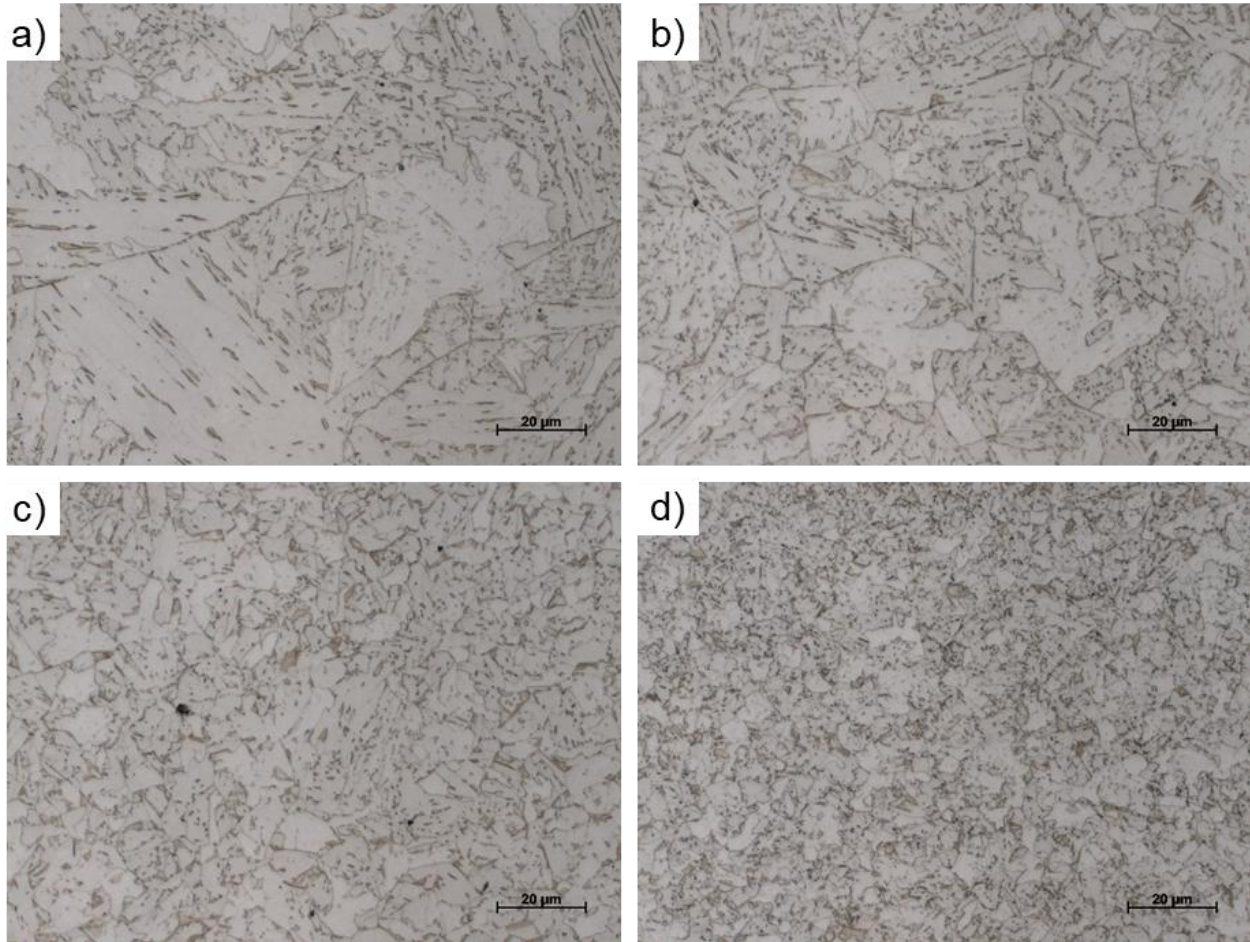


Figure 18. Representative light optical micrographs of the second pass of the HSLA-100 butt joint **a)** CGHAZ, **b)** FGHAZ close to the CGHAZ, **c)** FGHAZ close to the ICHAZ, and **d)** ICHAZ.

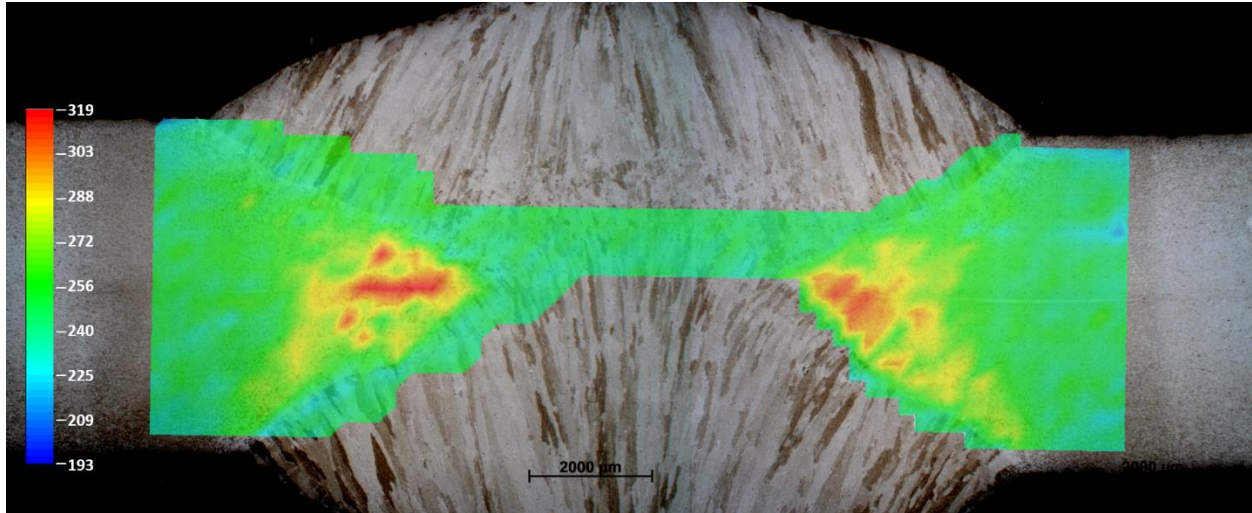


Figure 19. Composite image of light optical micrographs of the HSLA-100 butt joint overlaid with contour map of microhardness values in units of HV_{200} . Color scale adjusted to match the one shown in **Figure 22** for a direct comparison of the two joint configurations.

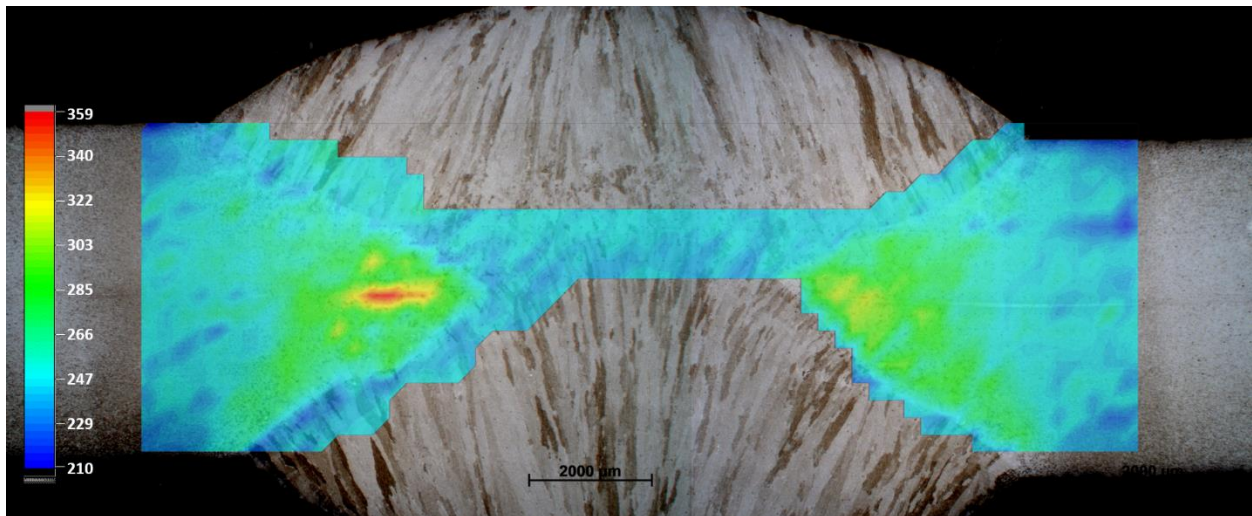


Figure 20. Composite image of light optical micrographs of the HSLA-100 butt joint overlaid with contour map of microhardness values in units of HV_{200} , with color scale that represents full range of values.

Representative HAZ microstructures for the second pass of the HSLA-100 tee joint are presented in **Figure 21**. A microhardness map with full-range color scale is provided in **Figure 22**, showing a map of indents spaced at intervals of $250\ \mu\text{m}$ in both the horizontal and vertical directions. Numerical values are provided in **Table 16** in **Appendix D**. Trends for the HAZ microhardness were consistent for microhardness traverses measured in comparable locations of each bead, with relatively low hardness values in the fusion zone and in the CGHAZ adjacent to the fusion line and dramatically increasing above $300\ HV_{200}$ in the FGHAZ. Microhardness values peaked in the FGHAZ, decreasing again towards approximately $240\ HV_{200}$ in the ICHAZ and then rising slightly to $257\ HV_{200}$ in the base metal, with regions reaching microhardness values as high as $280\ HV_{200}$.

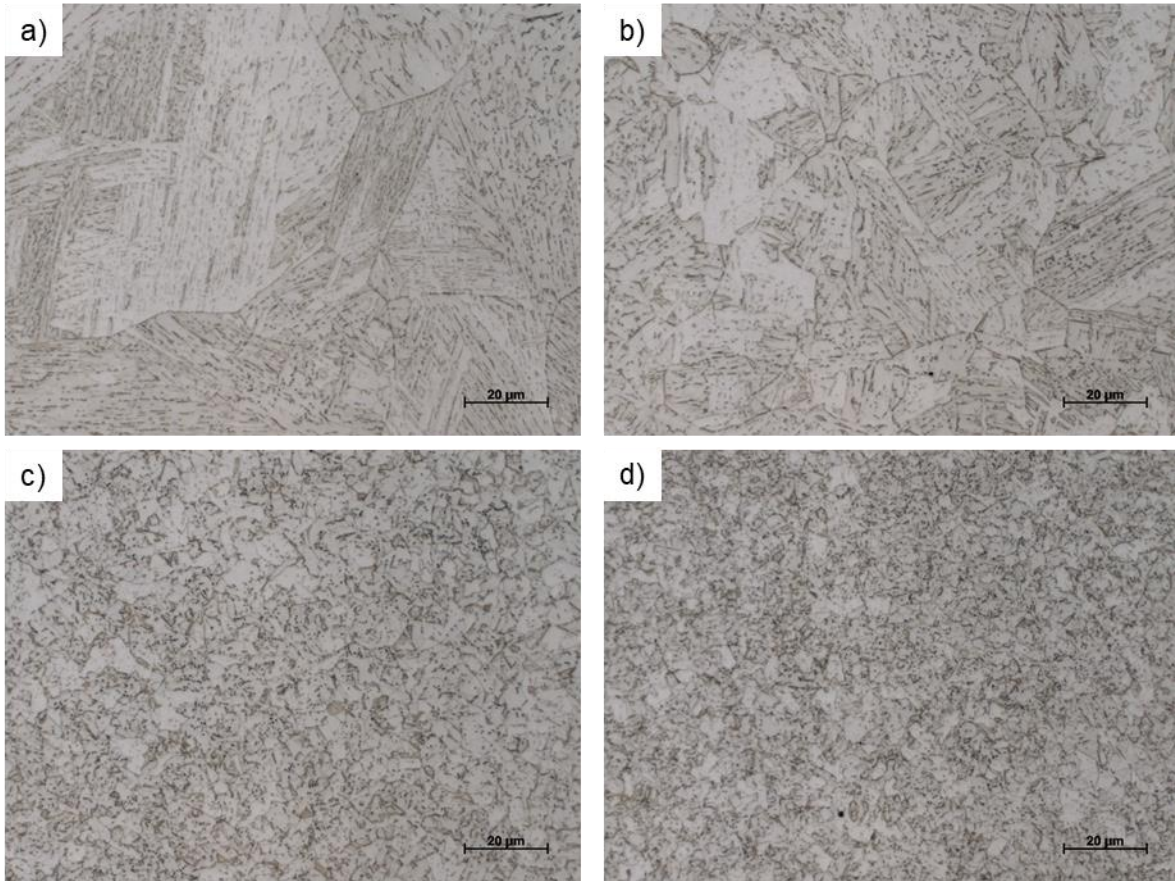


Figure 21. Representative light optical micrographs of the second pass of the HSLA-100 tee joint **a)** CGHAZ, **b)** FGHAZ close to the CGHAZ, **c)** FGHAZ close to the ICHAZ, and **d)** ICHAZ.

Gleeble simulated samples that compared most favorably to the weldment CGHAZ, FGHAZ, and ICHAZ were as follows. The CGHAZ was well-approximated by the sample heated to 1350 °C (2432 °F) and cooled at 10 °C/s (18 °F/s). The microstructures both seemed to be a mixture of bainite and martensite, with qualitatively comparable prior austenite grain size. Microhardness values also matched well, with the Gleeble sample measuring 266 HV₂₀₀ and the region of the tee joint pictured in **Figure 21a** measuring 269 HV₂₀₀. The FGHAZ close to the CGHAZ of the tee joint (see **Figure 21b**) matched well with the Gleeble sample heated to 1150 °C (2102 °F) and cooled at 5 °C/s (9 °F/s). Each microstructure was composed of a mixture of bainite and ferrite, with microhardness of 268 HV₂₀₀ and 274 HV₂₀₀ measured for the Gleeble sample and the weldment FGHAZ region in **Figure 21b**, respectively. Prior austenite grain size seemed slightly smaller in the weldment, which may explain the higher hardness value.

The region of the weldment FGHAZ far from the CGHAZ matched well with the sample heated to 1000 °C (1832 °F) and cooled at 5 °C/s (9 °F/s). Each was composed of a mixture of M/A constituent and ferrite with similar grain size. Microhardness values compared favorably as well, with the region of the weldment shown in **Figure 21c** measuring 261 HV₂₀₀ and the Gleeble sample measuring 251 HV₂₀₀. The ICHAZ of the weldment did not match as well with simulated Gleeble samples. The sensitivity of HSLA-100 to precipitate behavior, particularly ε-Cu precipitates, makes this region difficult to approximate without knowing the experimental thermal history undergone by the weldment. This is

particularly true as ϵ -Cu is expected to dissolve close to AC1, meaning that small deviations from the thermal history experienced by the weldment may produce an inaccurate simulated ICHAZ sample. Nevertheless, a rough approximation of the ICHAZ was seen in the sample heated to 790 °C (1454 °F) and cooled at 5 °C/s (9 °F/s). Each microstructure was composed of a mixture of ferrite and M/A constituent, though the region of the weldment shown in **Figure 21d** was associated with a microhardness of 267 HV₂₀₀, which is higher than the value of 250 HV₂₀₀ associated with the Gleeble sample. There was substantial variation in microhardness values measured throughout the ICHAZ of experimental weldments. Micrographs were taken on cross-sections near the surface of the plate, where the HAZ was relatively shallow. Though the same phases and morphologies were identified elsewhere, microhardness trended lower near this edge.

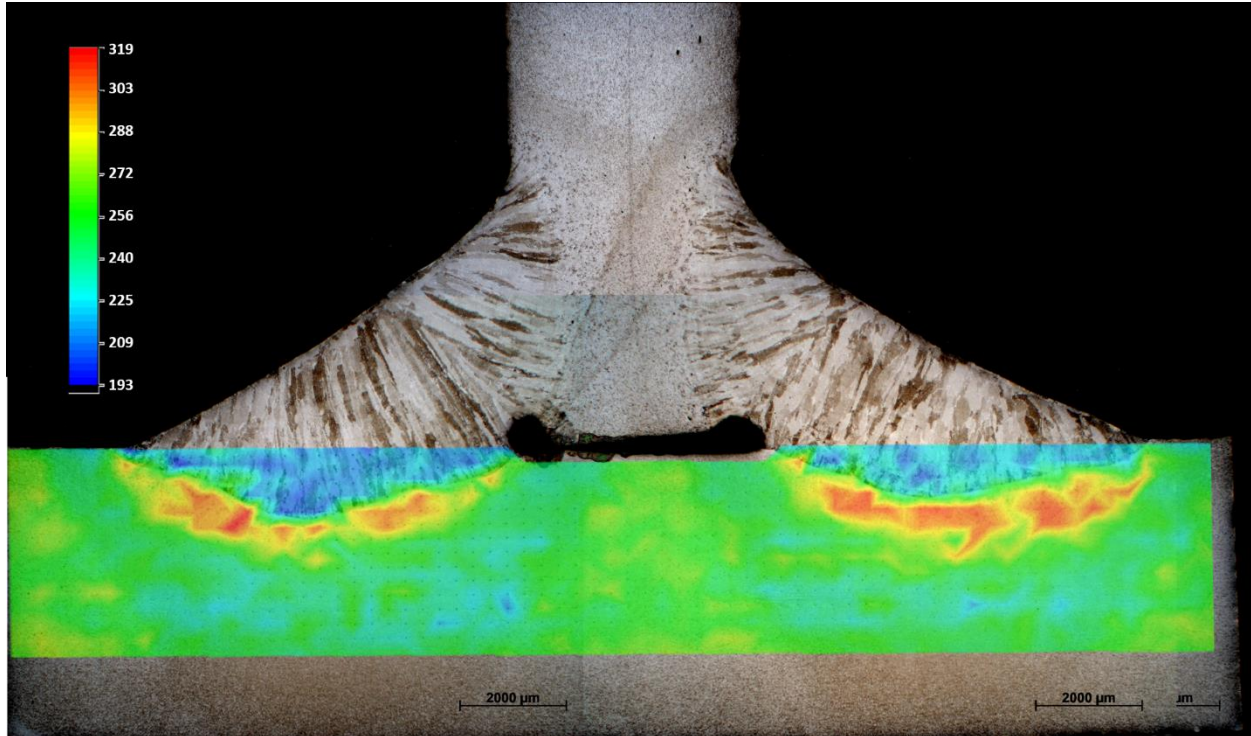


Figure 22. Composite image of light optical micrographs of the HSLA-100 fillet overlaid with contour map of microhardness values in units of HV₂₀₀.

Microhardness values measured in the butt joint matched well with those in the tee joint, though the butt joint weld metal was substantially harder than that of the tee joint. This is likely due to the reheating of metal in the butt joint, as these two weld beads overlapped whereas the geometry of the tee joint thermally isolated the two weld beads somewhat. The mechanism behind the fusion zone hardness differences were outside the scope of investigation but is speculated to relate to re-precipitation and/or coarsening of precipitates within the harder regions, which were effectively heat treated by the second weld pass.

Thermo-Physical Property Analysis

The CTE values measured from the dilation curves ($n=3$) were $1.5 \times 10^{-5} \pm 1.6 \times 10^{-7} \text{ } ^\circ\text{C}^{-1}$ ($8.6 \times 10^{-6} \pm 8.9 \times 10^{-8} \text{ } ^\circ\text{F}^{-1}$) for the untransformed base metal below 690 °C (1274 °F) and $2.2 \times 10^{-5} \pm 7.8 \times 10^{-7}$

$^{\circ}\text{C}^{-1}$ ($1.2 \times 10^{-5} \pm 4.4 \times 10^{-7} \text{ }^{\circ}\text{F}^{-1}$) for austenite above $860 \text{ }^{\circ}\text{C}$ ($1580 \text{ }^{\circ}\text{F}$). A representative graph showing the CTE measurement is given in **Figure 23**.

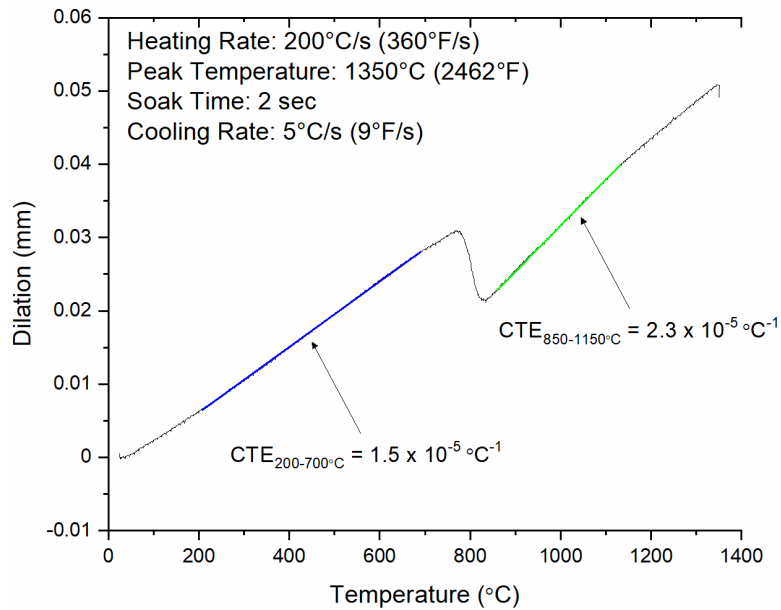


Figure 23. Representative on-heating dilatometry curve for HSLA-100, showing typical CTE analysis and results.

Temperature-dependent density values are shown in **Figure 24**. A comparison dataset from a Navy ManTech study conducted at the Naval Metalworking Center from the mid-2000s is also included in the figure [15]. This data is labeled “CTC” for Concurrent Technologies Corporation, where the testing was conducted. Since the slopes of the lines (*i.e.*, the CTE) are nearly identical, differences between the data can be primarily attributed to a difference in the measured room temperature density between the two studies.

The measured specific heat and thermal diffusivity data for HSLA-100 can be found in **Figures 25-26**. The peaks or cusps in the data correspond to the effects of thermal energy absorption during phase transformations, particularly during the austenitic transformation between approximately 700 to $900 \text{ }^{\circ}\text{C}$ (1292 to $1652 \text{ }^{\circ}\text{F}$). As shown, the data from this program compare very well with the data generated in the Navy ManTech study at CTC [15].

Finally, the data from **Figures 24-26** were used in conjunction with **Equation 4** to calculate the temperature-dependent thermal conductivity as shown in **Figure 27**. Once again, the data coincides fairly well with the previous reporting from CTC. The raw data points for all of the thermo-physical property graphs can be found in **Appendix E**.

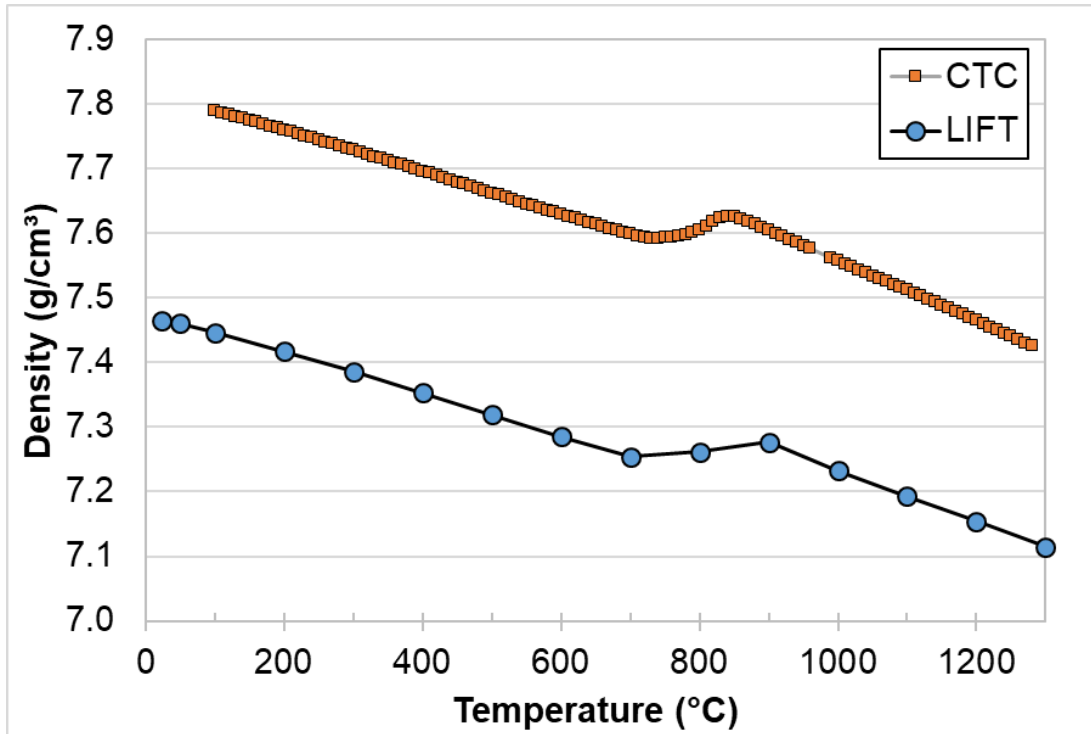


Figure 24. Density of HSLA-100 steel as a function of temperature. LIFT data measured using analysis of Gleeble-based dilation curves in accordance with **Equations 2 and 3**. CTC data is adapted from reference [15].

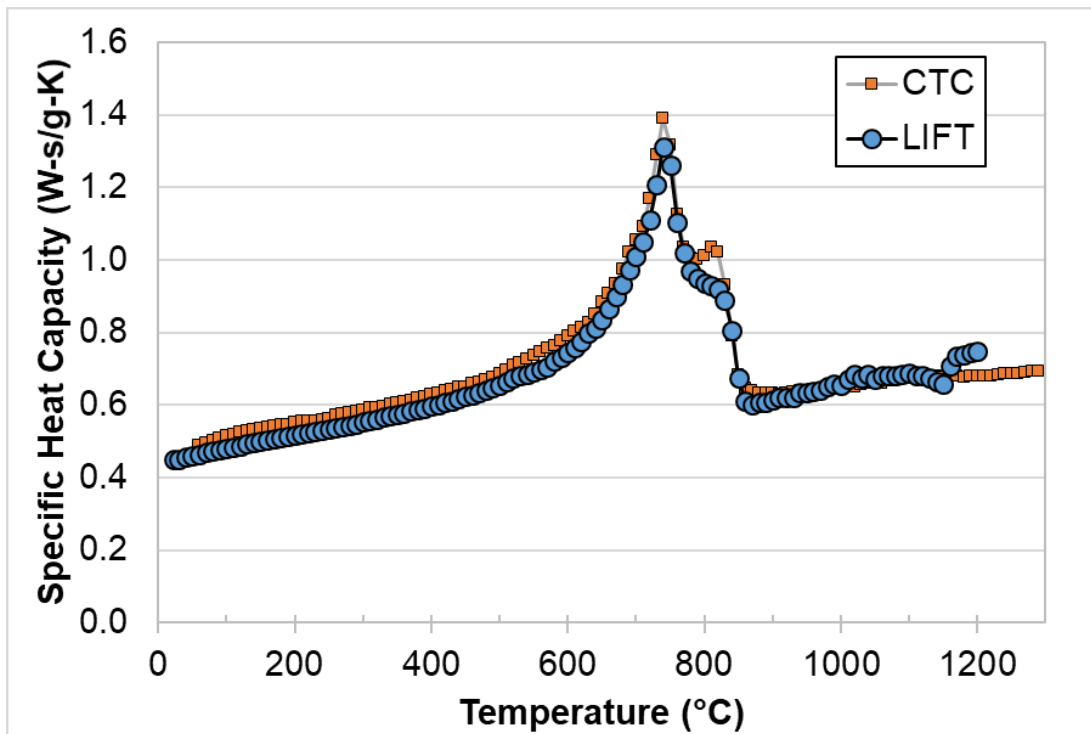


Figure 25. Measured specific heat for HSLA-100 steel at various temperatures. CTC data adapted from reference [15].

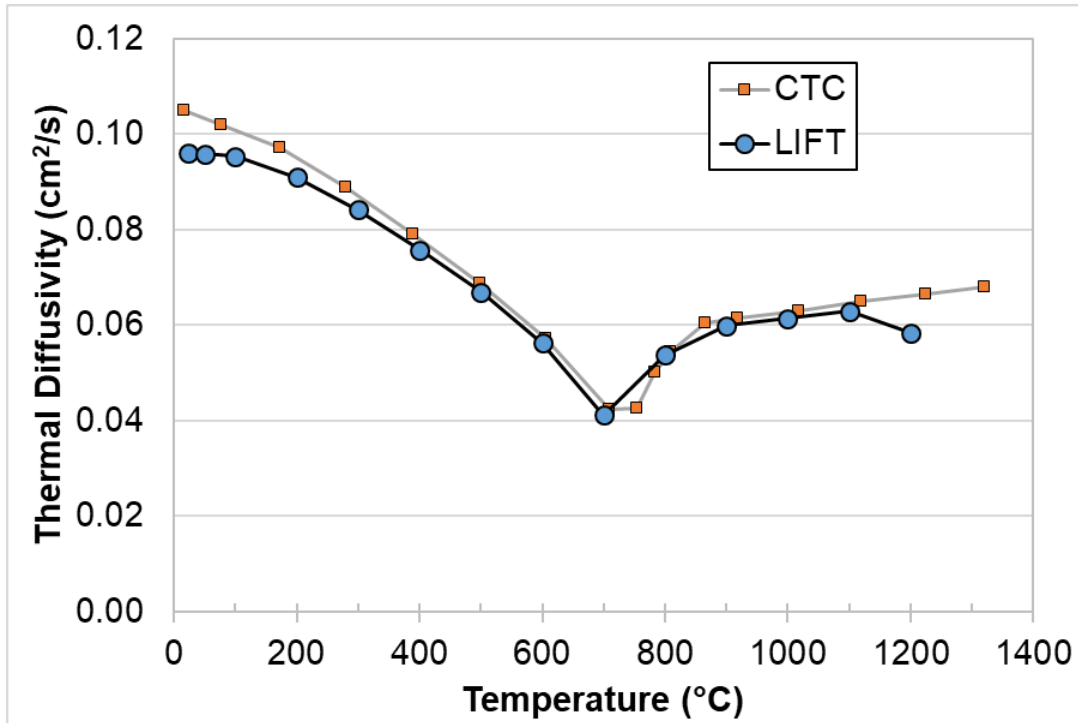


Figure 26. Measured thermal diffusivity for HSLA-100 steel at various temperatures. CTC data adapted from reference [15].

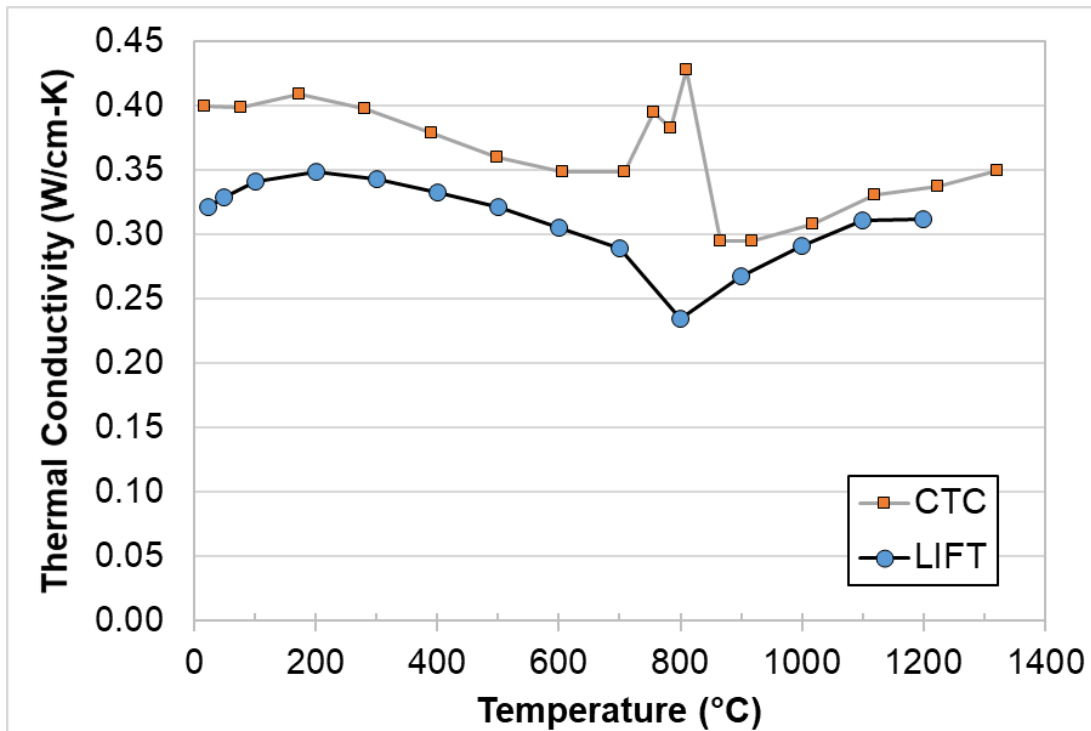


Figure 27. Calculated thermal conductivity for HSLA-100 steel at various temperatures. CTC data adapted from reference [15].

Thermo-Mechanical Property Analysis

Figure 28 shows the values for elastic modulus as a function of temperature that were assumed in this work. The elevated temperature mechanical testing described above was performed in accordance with ASTM E21 [13] rather than the more appropriate ASTM E111 [38], which is prescribed when elastic modulus measurements are to be made. As such, it was determined that the experimentally measured elevated temperature elastic moduli were likely inaccurate. In order to provide elevated temperature modulus values for a HSLA-100 property database, the data in **Figure 28** were adapted from the European standard for fire design of steel structures [39] [40]. Of the potential sources for this information, the European standard contained the most complete data covering temperatures relevant to this study. A room temperature elastic modulus of 210 GPa (30.5 Msi) was assumed [39], as it had been previously for DH36 [5], HSLA-65 [6], and HSLA-80 [7] steel. It was also assumed that rigorously measured elastic moduli for HSLA-100 steel would be very similar to data presented in **Figure 28** because elastic properties tend to be consistent within a given material system (*e.g.*, steel).

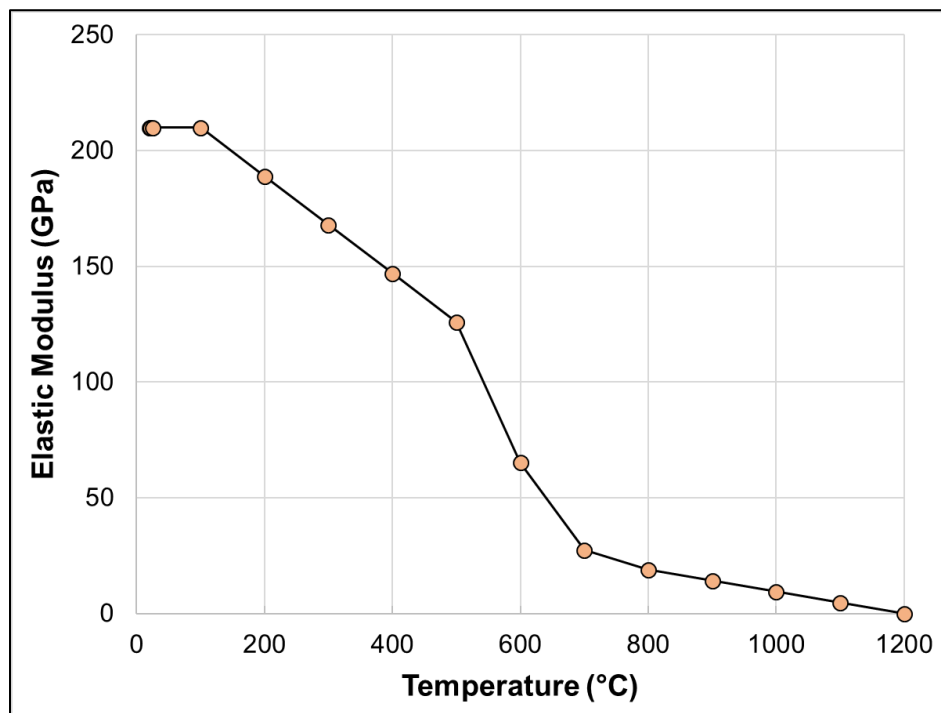


Figure 28. Assumed elevated temperature elastic modulus for HSLA-100 steel as adapted from references [39] [40].

Figure 29 shows the experimentally measured temperature-dependent 0.2% offset yield strength for HSLA-100 base material, and **Figure 30** shows the measured temperature-dependent ultimate tensile strength (UTS). This data was calculated from the DIC analysis at OSU after converting to engineering stress and strain values. As expected, increased temperatures result in significant strength loss. At temperatures above 800 °C (1472 °F), the base metal microstructure is completely transformed to the weaker austenite phase, resulting in relatively minor differences in strength with increasing temperature. As shown, the data from this program compare very well with the data generated in the Navy ManTech study at CTC [15].

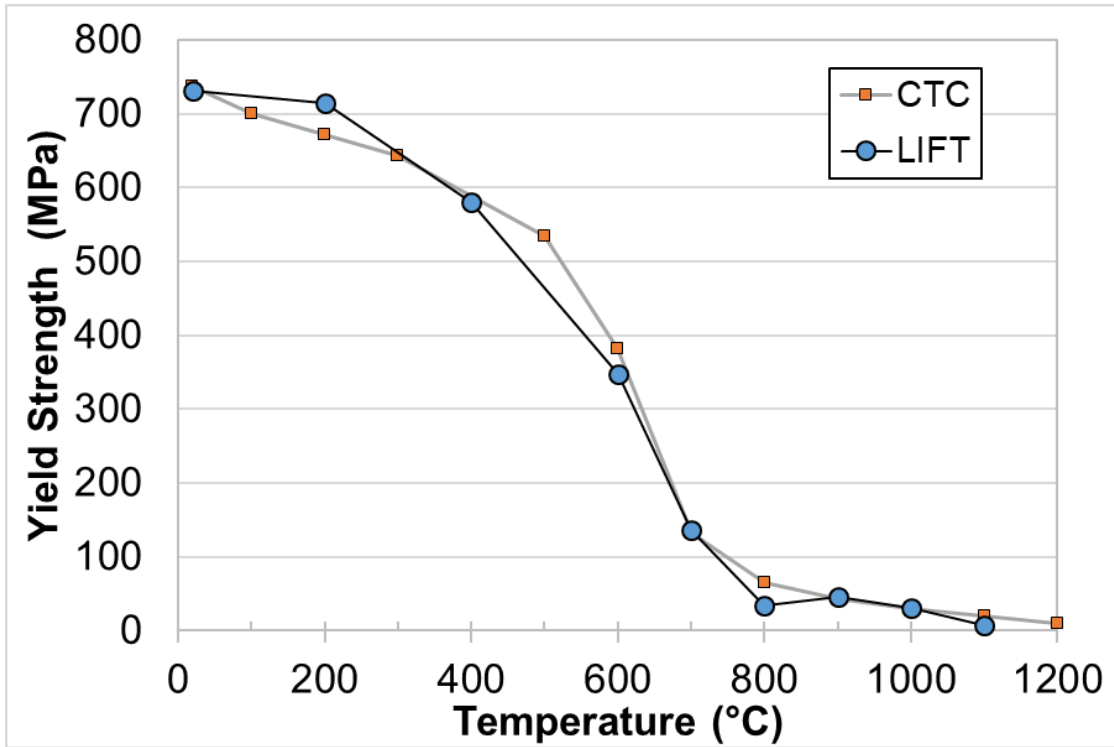


Figure 29. Measured elevated temperature 0.2% offset yield strength for HSLA-100 steel. CTC data adapted from reference [15].

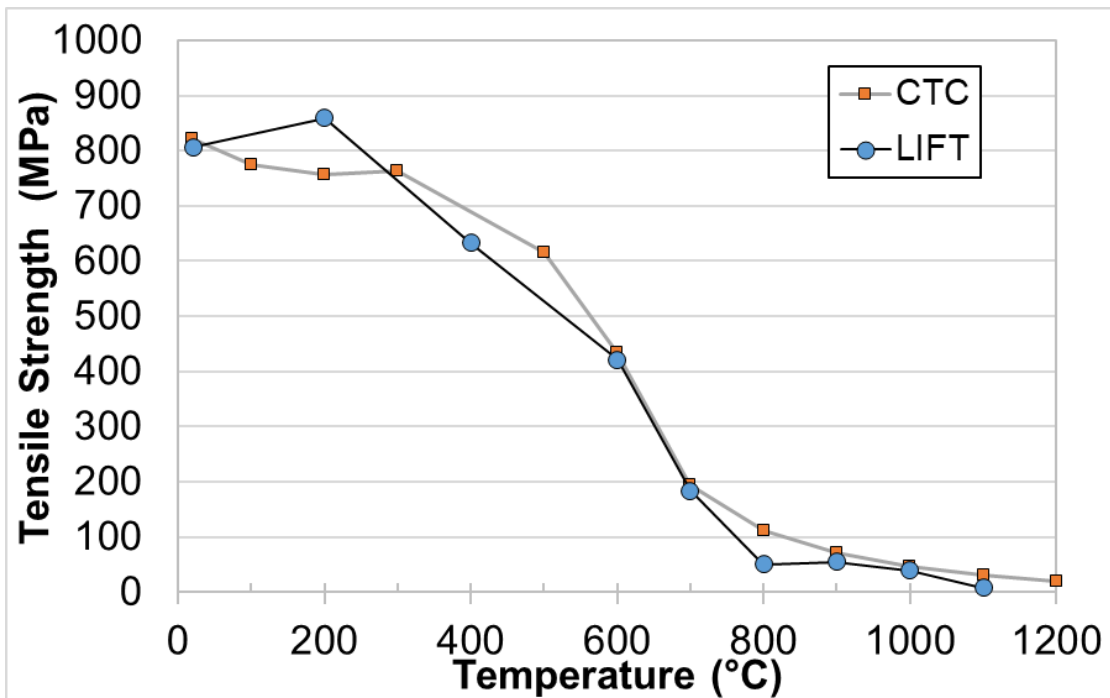


Figure 30. Measured elevated temperature ultimate tensile strength (UTS) for HSLA-100 steel. CTC data adapted from reference [15].

The measured 0.2% offset yield strengths from specimens cycled to a peak temperature of 1350 °C (2462 °F) is shown in **Figure 31**, along with those of the base metal on-heating for comparison. The stress-strain curves associated with the data are given in **Figures 68-71** of **Appendix F**. At room temperature, higher yield strength correlated with higher cooling rates. Only the specimen cooled at 1 °C/s (1.8 °F/s) had lower strength than the base metal at temperatures below 600 °C (1112 °F). Specimens cooled at 10 °C/s (18 °F/s) and above formed bainitic and/or martensitic microstructures, which are typically expected to yield at higher loads than the ferritic base material. The specimen cooled at 1 °C/s (1.8 °C/s) was also composed of a ferritic microstructure, though excessive grain growth created a microstructure that underperformed that of the base material until reaching the 600 °C (1112 °F) test temperature. It is likely that precipitates from the original base material microstructure experienced dissolution during the thermal cycling of the HAZ tensile specimens. The study by Sun *et al.* indicated that significant re-precipitation is unlikely to occur with less than 0.5 hours spent in an appropriate aging temperature regime (approximately 500 °C [932 °F]) [28]. As such, the high strength of the base material as compared to the sample cooled at 1 °C/s (1.8 °F/s) can be attributed to both Hall-Petch effect (due to the refined grain size) and by the persistence of ϵ -Cu precipitates from the original material processing, which increase strength by resisting dislocation motion.

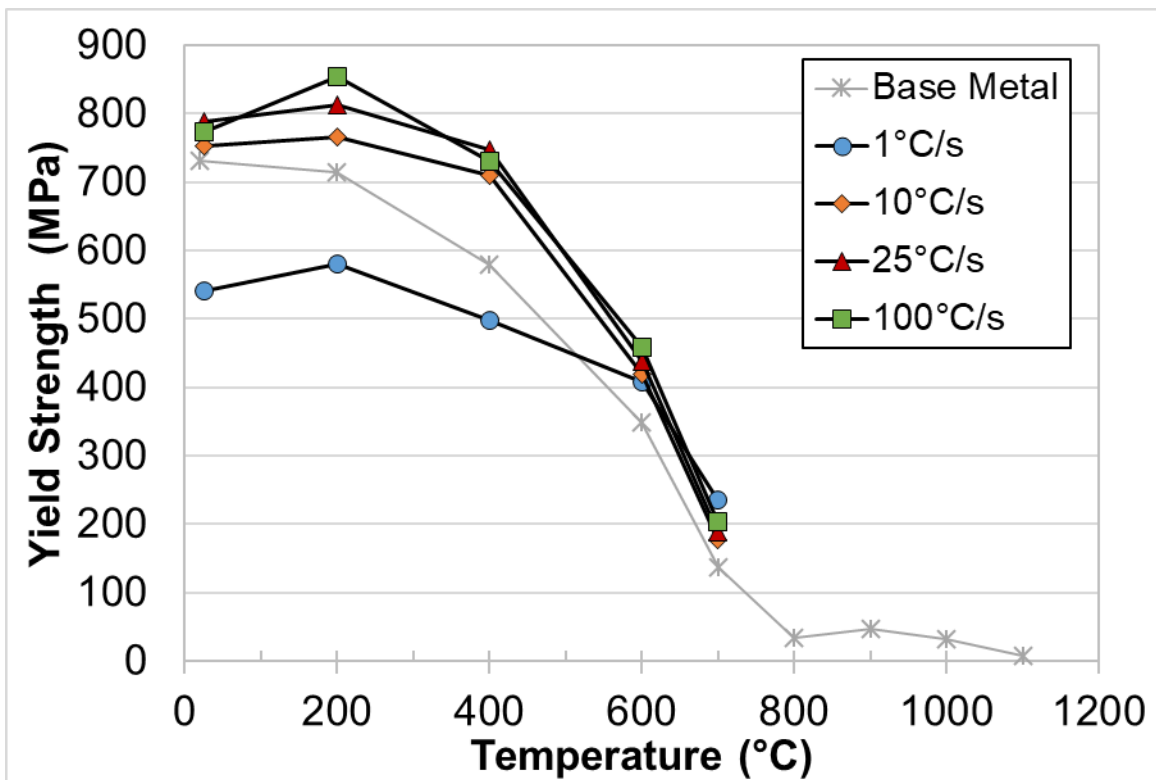


Figure 31. Yield strength of simulated HSLA-100 CGHAZs after heating to 1350 °C (2462 °F) and cooling at different rates as compared with base material yield strength.

Yield strength for all thermally cycled specimens increased slightly from 25 °C to 200 °C, then steadily decreased with further temperature increases. In contrast, base metal strength showed a monotonic decrease in strength. Yield strength of the three rapidly cooled samples converged to approximately 718 MPa (104 ksi) at a testing temperature of 400 °C, with all thermally cycled specimens converging at higher test temperatures. The base metal yield strength remained approximately 100 MPa (14.5 ksi) below the average thermally cycled yield strength when the four samples converged. It is

unclear why the base material yield strength did not converge with the thermally cycled samples. The difference in yield strength may indicate that thermally cycling the HAZ specimens caused precipitation of a carbide that persisted to high temperatures during subsequent tensile tests, or it may simply be an artifact of the different test methods used to gather data for the base material and HAZ specimens.

On-heating flow stress measurements for the HSLA-100 base material are shown in **Figure 32** for all temperatures, and **Figure 33** highlights the flow behavior for tests at temperatures of 800 °C (1472 °F) and above. The raw data points for these graphs can be found in **Appendix F**. The data are true stresses and strains as generated by the DIC analysis from OSU. In several cases, the data seemed to show indefinite work hardening, *i.e.*, there was no plateau of stress values as strain increased. The experimental mechanism behind this behavior was unclear, but it was judged to be an artifact of the test method rather than a reflection of actual material behavior. In these cases the UTS values were unclear, but the best estimates are provided in **Appendix F**. As expected, increasing the test temperature tends to flatten the flow stress curves, since work hardening is made more difficult by dynamic recovery and/or recrystallization effects.

Flow stress curves for the thermally cycled HSLA-100 are given in **Figures 34-37**. Once again, the data are true stresses and strains calculated by conversion from engineering stress-strain data as generated by testing at NSWCCD. Such conversions are invalid past the onset of necking, so the terminal data points in **Figures 34-37** are at the UTS. All raw data points for these figures, along with the engineering fracture strains for the specimens, are found in **Appendix F**.

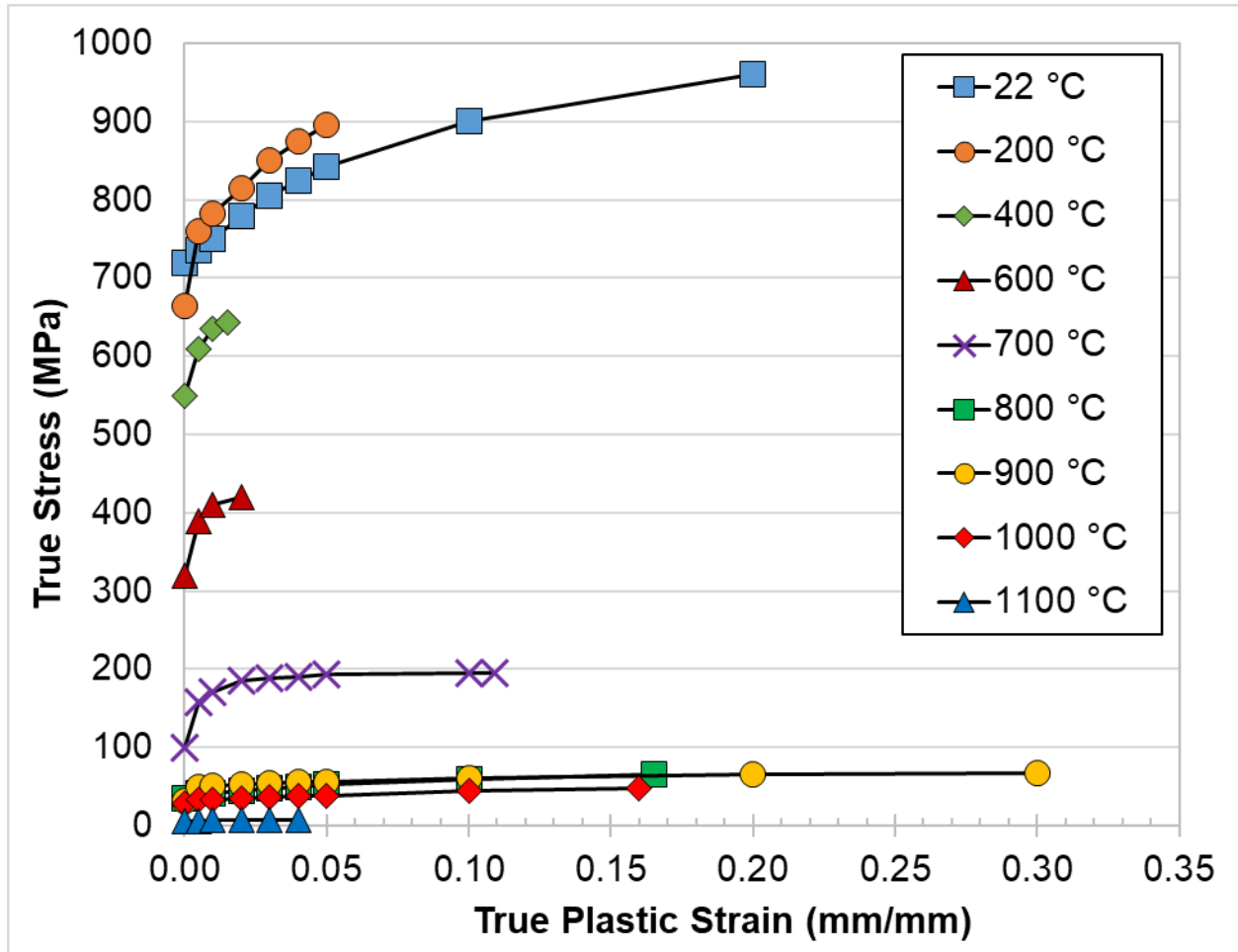


Figure 32. On-heating flow stress behavior for HSLA-100 steel at various temperatures.

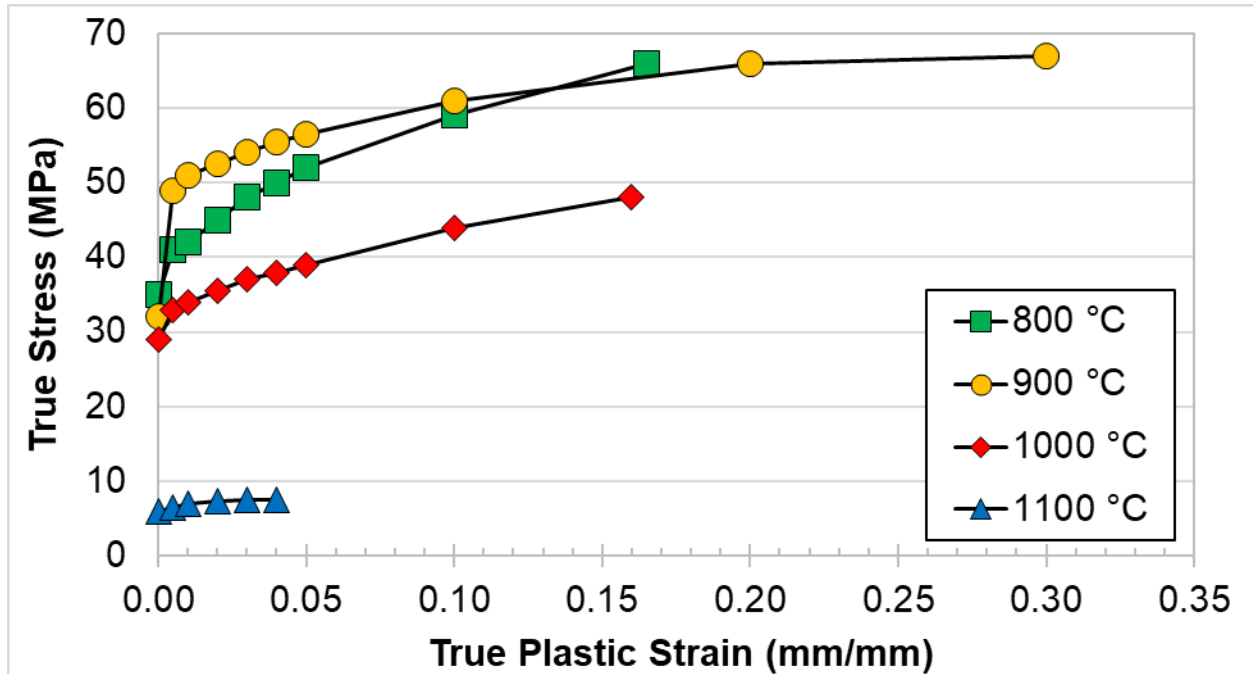


Figure 33. On-heating flow stress behavior for HSLA-100 steel at testing temperatures above the austenitic phase transformation.

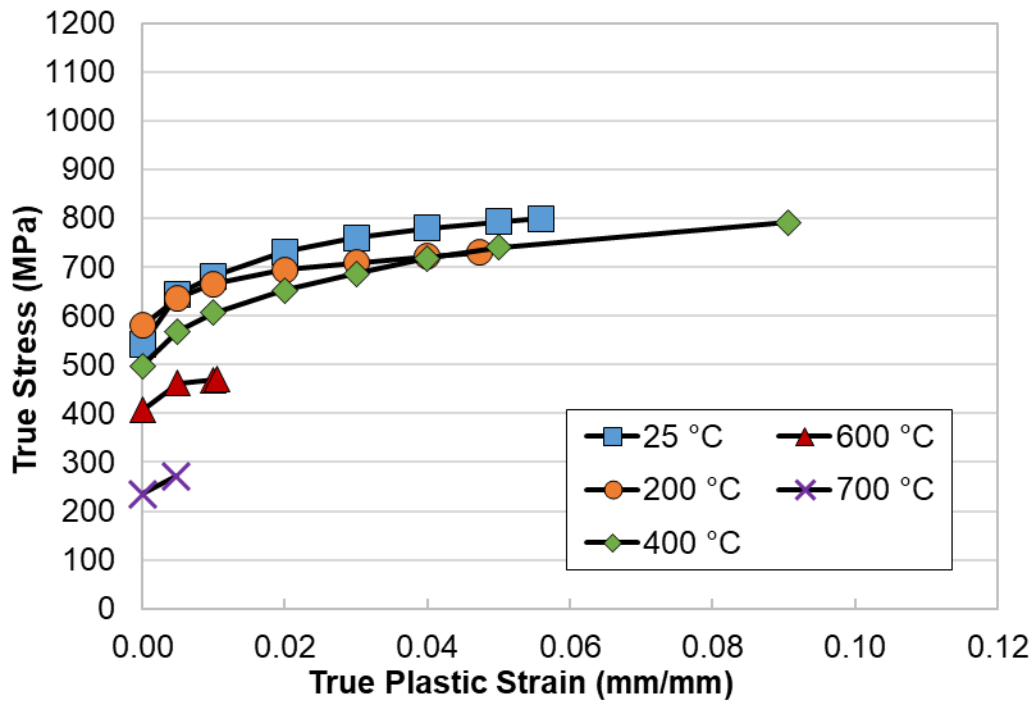


Figure 34. Flow stress behavior at various temperatures for HSLA-100 steel after cooling at 1 °C/s (1.8 °F/s) from a peak temperature of 1350 °C (2462 °F). Terminal data points are at the UTS.

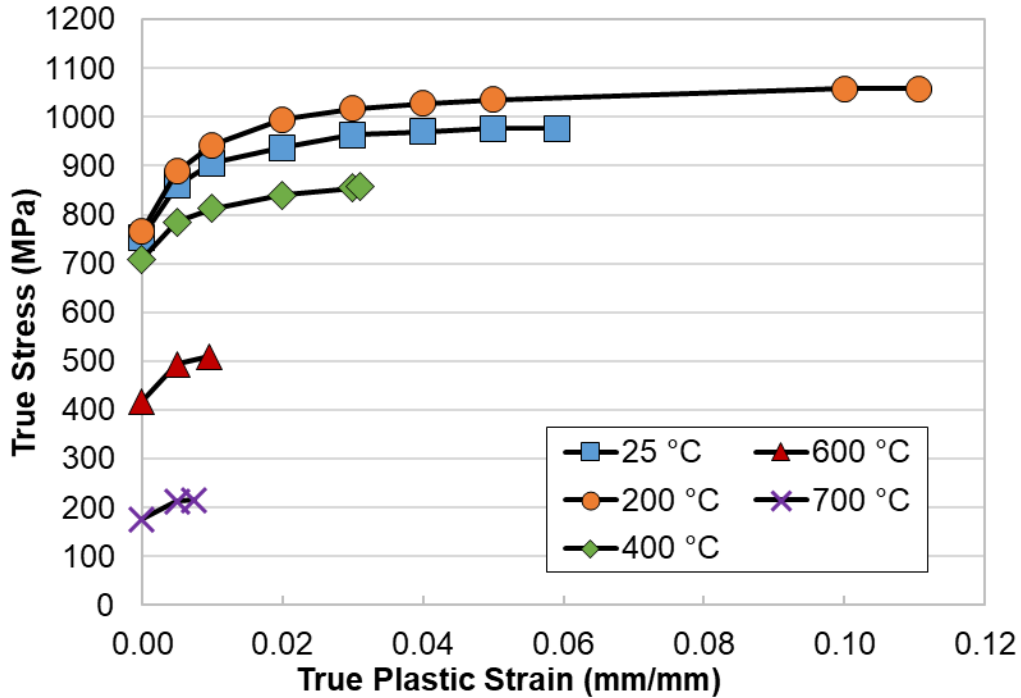


Figure 35. Flow stress behavior at various temperatures for HSLA-100 steel after cooling at 10 °C/s (18 °F/s) from a peak temperature of 1350 °C (2462 °F). Terminal data points are at the UTS.

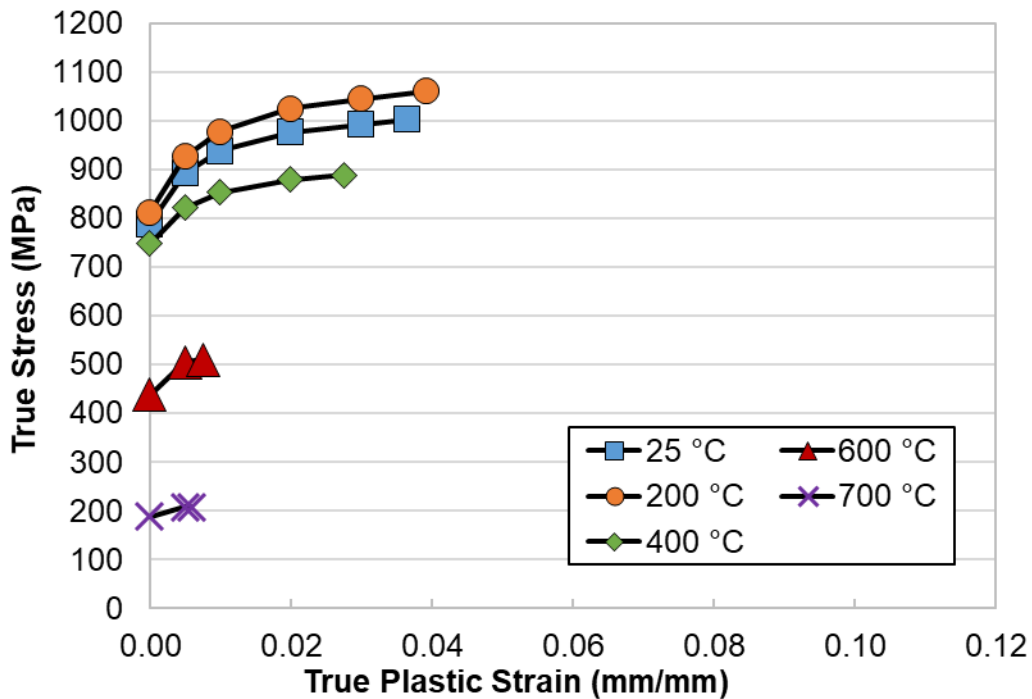


Figure 36. Flow stress behavior at various temperatures for HSLA-100 steel after cooling at 25 °C/s (45 °F/s) from a peak temperature of 1350 °C (2462 °F). Terminal data points are at the UTS.

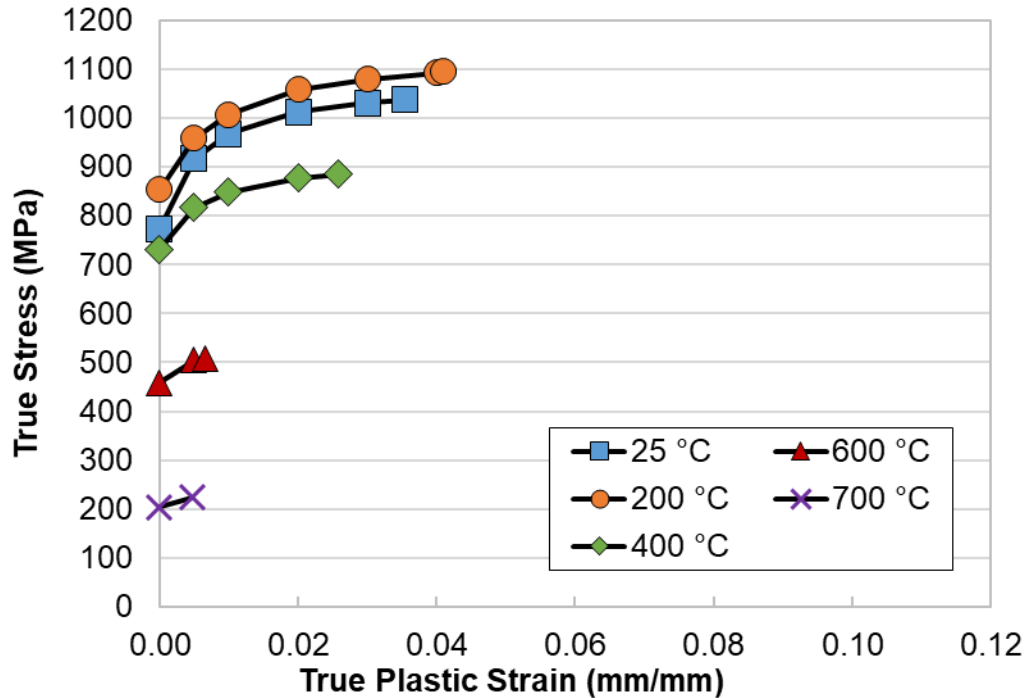


Figure 37. Flow stress behavior at various temperatures for HSLA-100 steel after cooling at 100 °C/s (180 °F/s) from a peak temperature of 1350 °C (2462 °F). Terminal data points are at the UTS.

CONCLUSIONS

Temperature-dependent material property data of a pedigreed plate of HSLA-100 steel from room temperature up to nearly the steel's melting point were determined. The thermo-physical properties investigated include specific heat, thermal diffusivity, thermal conductivity, CTE, and density. Thermo-mechanical properties including yield strength, UTS, and flow stress were also measured. The temperatures associated with on-heating and on-cooling phase transformations and their variation with heating rate, cooling rate, and peak temperature were determined and used to develop welding-focused CCT diagrams. Investigation of HAZ microstructures from the CCT specimens and arc welds concluded the analysis. This effort is essential for increasing the fidelity of finite element models used to predict welding-induced distortion and residual stress in marine structures. The data generated in this program have been provided to ESI for immediate incorporation into their *SYSWELD* software. A machine-readable version of the collected data will be uploaded to the University of Michigan's *Materials Commons* data repository <<https://materialscommons.org>> at a later date.

APPENDIX

Appendix A: Plate Conformance Certificate and Chemical Composition for HSLA-100



TEST CERTIFICATE

SHIP TO: ARCELORMITTAL PLATE LLC
 RONSON TECHNICAL PRODUCTS
 C/O HUDSON METAL PROCESSING
 1500 NATIONAL CEMETERY ROAD
 FLORENCE SC 29506

PAGE NO: 01 OF 02
 FILE NO: 2822-01-02
 MILL ORDER NO: 83506-001
 MELT NO: D2773
 SLAB NO: 39AA
 DATE: 06/08/18

SOLD TO: ENERGY & PROCESS CORPORATION
 A FERGUSON ENTERPRISE
 P.O. BOX 125
 TUCKER GA 30085-0125

SEND TO:

01-C

STEEL PLATE DIMENSIONS / DESCRIPTION

TOTAL QTY	GAUGE	WIDTH	LENGTH	DESCRIPTION	PIECE WEIGHT
1	3/16"	96"	240"	RECTANGLE	1225#

CUSTOMER INFORMATION

CUSTOMER PO: R257-210 ADD# 2
 PART NO. SP-HSLA100316N

SPECIFICATION (S)

THIS MATERIAL HAS BEEN MANUFACTURED AND TESTED IN ACCORDANCE WITH PURCHASE ORDER REQUIREMENTS AND SPECIFICATION(S).

NAVSE TECH-PUB-T9074 REV 2 YR 12 CL 3 HSLA100-TYI
 MIL S-24645A(SH) AMEND#1 CL 3 GR HSLA100-TY.I
 TECH PUB T9074-BD-GIB-010/0300 HSLA100
 DATED 12/18/12

THE MANAGEMENT SYSTEMS FOR MANUFACTURE OF THIS PRODUCT ARE CERTIFIED TO ISO 9001:2008 (CERTIFICATE NO. 30130) AND ISO 14001:2004 (CERTIFICATE NO. 49009).

CHEMICAL COMPOSITION (WT%) FOR ALL ELEMENTS EXCEPT H (PPM)

	C	MN	P	S	CU	SI	NI	CR	MO
MELT:D2773	.04	.90	.007	.001	1.12	.28	1.59	.60	.32
PROD ANALYSIS	.04	.91	.007	.002	1.18	.29	1.66	.60	.32
	V	TI	AL	CB	SB	AS	SN	N	LOC
MELT:D2773	.002	.003	.025	.026	.0010	.0040	.010	.0061	
PROD ANALYSIS	.001	.002	.024	.028	.0020	.0040	.011	.0064	BOT

MANUFACTURE

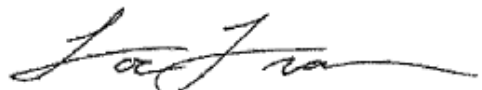
ELECTRIC FURNACE QUALITY - FINELINE - VACUUM DEGASSED - FINE GRAIN PRACTICE

HEAT TREAT CONDITION

MATL OR TEST	HEAT TREAT DESCRIPTION	NOM TEMP	HOLD MINS	COOL MTHD
PL/TEST	HARDEN	1675F	14	W. QUENCH
PL/TEST	PRECIP. AGED	1160F	28	AIR COOL

WE HEREBY CERTIFY THE ABOVE INFORMATION IS CORRECT:

ARCELORMITTAL PLATE LLC
 QUALITY ASSURANCE LABORATORY
 139 MODENA ROAD
 COATESVILLE, PA 19320


 SUPERVISOR - TEST REPORTING
 LOC TRAN

TEST CERTIFICATE

PAGE NO: 02 OF 02
 FILE NO: 2822-01-02
 MILL ORDER NO: 83506-001
 MELT NO: D2773
 SLAB NO: 39AA
 DATE: 06/08/18

TENSILE PROPERTIES

SLAB NO.	LOC	DIR	YIELD STRENGTH PSI X 1000	TENSILE STRENGTH PSI X 1000	ELONGATION AFTER FRACTURE GAGE LGTH	%
39AA	BOT.	TRANS.	113	115	2.00"	21.0
39AA	TOP	TRANS.	112	114	2.00"	21.0

GENERAL INFORMATION

ALL STEEL HAS BEEN MELTED AND MANUFACTURED IN THE U.S.A.
 PRODUCED IN ACCORDANCE WITH INSPECTION SYSTEM
 REQUIREMENTS OF MIL-I-45208A AMEND #1.
 A.B.S. CERTIFICATE QA 2799196-A
 A.B.S. CERTIFICATE QA 2799196-B
 MATERIAL HAS BEEN VACUUM DEGASSED AND CALCIUM TREATED
 FOR SULFIDE SHAPE CONTROL. FINELINE MOD FOR SULPHUR
 THE TEST RESULTS SHOWN IN THIS REPORT ARE THE
 RESULTS OF TESTING PERFORMED BY OUR ORGANIZATION.
 NO WELD REPAIR PERFORMED BY ARCELORMITTAL PLATE LLC.
 ALL STEEL HAS BEEN MANUFACTURED IN THE U.S.A.
 MERCURY OR MERCURY COMPOUNDS ARE NOT USED IN THE MANUFACTURE
 OF ARCELORMITTAL PLATE LLC PRODUCTS.
 ACID SOLUBLE ALUMINUM
 FOR MORE INFORMATION AND PROCESSING GUIDELINES, REFER TO
 WWW.USA.ARCELORMITTAL.COM/PLATE

LOW MELTING ALLOYS/LOW MELTING COMPOUNDS ARE NOT USED IN THE MFG. OF
 ARCELORMITTAL PLATE LLC PRODUCTS OTHER THAN AS DEOXIDIZING AGENTS.

KNOWINGLY AND WILLFULLY FALSIFYING OR CONCEALING A MATERIAL FACT ON THIS
 FORM, OR MAKING FALSE, FICTITIOUS OR FRAUDULENT ENTRIES OR REPRESENTATIONS
 HEREIN, COULD CONSTITUTE A FELONY PUNISHABLE UNDER FEDERAL STATUTES.

CERTIFICATE OF CONFORMANCE - ALL ITEMS FURNISHED IN THE SHIPMENT ARE IN
 FULL CONFORMANCE WITH ALL P.O. AND SPEC. REQ.; AND THAT THE T.R.'S
 REPRESENT THE ACTUAL ATTRIBUTES OF THE ITEMS FURNISHED ON THE ORDER, AND
 THAT THE TEST RESULTS ARE IN FULL CONFORMANCE WITH ALL P.O. & SPEC. REQ.
 RECORDS TO SUBSTANTIATE THE ABOVE ARE ON FILE IN

OUR PLANT AND WILL BE MAINTAINED FOR A PERIOD OF 7 YRS. FROM THE DATE OF
 THE SHIPMENT UNLESS FURNISHED TO THE PURCHASER IN ADVANCE OF OR AT TIME OF
 SHIPMENT. WHEN RECORDS ARE RETAINED BY US, WE AGREE TO FURNISH SAME TO THE
 PURCHASER AT ANY TIME DURING THE ABOVE PERIOD UPON REQUEST.

B/L #34436 P&S TRANSPORTATION INC.

WE HEREBY CERTIFY THE ABOVE
 INFORMATION IS CORRECT:

ARCELORMITTAL PLATE LLC
 QUALITY ASSURANCE LABORATORY
 139 MODENA ROAD
 COATESVILLE, PA 19320

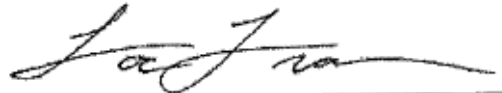

 SUPERVISOR - TEST REPORTING
 LOC TRAN

Table 8. Chemical Composition of HSLA-100 Base Plate as Measured by OSU

Element	Wt	Test 1	Test 2	Test 3	Average
C	%	0.034	0.031	0.027	0.031
Si	%	0.28	0.28	0.28	0.28
Mn	%	0.89	0.88	0.88	0.88
P	%	0.008	0.007	0.007	0.007
S	%	0.0009	0.0009	0.0008	0.0009
Cr	%	0.59	0.58	0.59	0.59
Mo	%	0.32	0.32	0.32	0.32
Ni	%	1.95	1.94	1.94	1.94
Al	%	0.029	0.028	0.028	0.028
Cu	%	1.13	1.13	1.13	1.13
Nb	%	0.027	0.027	0.027	0.027
Ti	%	0.002	0.002	0.002	0.002
V	%	0.003	0.002	0.003	0.003
W	%	<0.005	<0.005	<0.005	<0.005
Pb	%	0.004	0.004	0.004	0.004
Sn	%	0.012	0.012	0.012	0.012
As	%	0.015	0.011	0.012	0.013
Zr	%	<0.0010	<0.0010	<0.0010	<0.0010
Ca	%	0.002	0.002	0.002	0.002
Ce	%	<0.0010	<0.0010	<0.0010	<0.0010
Sb	%	0.014	0.013	0.014	0.014
Se	%	0.003	0.004	0.004	0.004
Te	%	0.016	0.016	0.016	0.016
Ta	%	<0.007	<0.007	<0.007	<0.007
B	%	0.002	0.001	0.001	0.001
Zn	%	0.002	0.002	0.002	0.002
La	%	<0.0003	<0.0003	<0.0003	<0.0003

Appendix B: Continuous Cooling Transformation Curves

Table 9. Austenite Transformation Temperatures as Illustrated in **Figure 8**

Heating Rate (°C/s)	A _{c1} (°C)	A _{c3} (°C)
10	747	865
100	764	862
200	759	836
500	773	844
1000	763	813
2000	755	814
CTC [15]: 1.0 in. (25.4 mm) nominal plate thickness	A _{c1} (°C)	A _{c3} (°C)
10	695	840
Yue <i>et al.</i> [17]: 0.5 in. (12.7 mm) nominal plate thickness	A _{c1} (°C)	A _{c3} (°C)
200	765 ± 4.8	850 ± 6.7

Table 10. Experimentally Measured On-Cooling Transformation Temperatures for HSLA-100 Dilatometry Specimens Cooled from 790 °C (1454 °F). Note: Colors correspond to the transformation products discussed in **Figure 9-15**.

Cooling Rate (°C/s) [°F/s]	1 [1.8]	5 [9]	10 [18]	25 [45]	100 [180]	200 [360]
Transformation Temperature (°C) [°F]	684 [1263]	682 [1260]	672 [1242]	601 [1114]	583 [1081]	588 [1090]
	585 [1085]	586 [1087]	585 [1085]	483 [901]	449 [840]	457 [855]
	452 [846]	457 [855]	453 [847]	461 [862]	364 [687]	352 [666]

Table 11. Experimentally Measured On-Cooling Transformation Temperatures for HSLA-100 Dilatometry Specimens Cooled from 1000 °C (1832 °F). Note: Colors correspond to the transformation products discussed in **Figure 9-15**.

Cooling Rate (°C/s) [°F/s]	1 [1.8]	5 [9]	10 [18]	25 [45]	100 [180]	200 [360]
Transformation Temperature (°C) [°F]	678 [1252]	632 [1170]	596 [1105]	596 [1105]	532 [990]	502 [936]
	512 [954]	499 [930]	469 [876]	445 [833]	465 [869]	464 [867]
	458 [856]	453 [847]	424 [795]	369 [696]	333 [631]	331 [628]

Table 12. Experimentally Measured On-Cooling Transformation Temperatures for HSLA-100 Dilatometry Specimens Cooled from 1150 °C (2102 °F). Note: Colors correspond to the transformation products discussed in **Figure 9-15**.

Cooling Rate (°C/s) [°F/s]	1 [1.8]	5 [9]	10 [18]	25 [45]	100 [180]	200 [360]
Transformation Temperature (°C) [°F]	594 [1101]	573 [1063]	550 [1022]	507 [945]	479 [894]	481 [898]
	437 [819]	444 [831]	394 [741]	482 [900]	333 [631]	339 [642]
		414 [777]		360 [680]		

Table 13. Experimentally Measured On-Cooling Transformation Temperatures for HSLA-100 Dilatometry Specimens Cooled from 1350 °C (2462 °F). Note: Colors correspond to the transformation products discussed in **Figure 9-15**.

Cooling Rate (°C/s) [°F/s]	1 [1.8]	5 [9]	10 [18]	25 [45]	100 [180]	200 [360]
Transformation Temperature (°C) [°F]	589 [1092]	574 [1065]	555 [1031]	500 [932]	482 [900]	495 [923]
	449 [840]	402 [756]	406 [763]	480 [896]	362 [684]	361 [682]
				385 [725]		

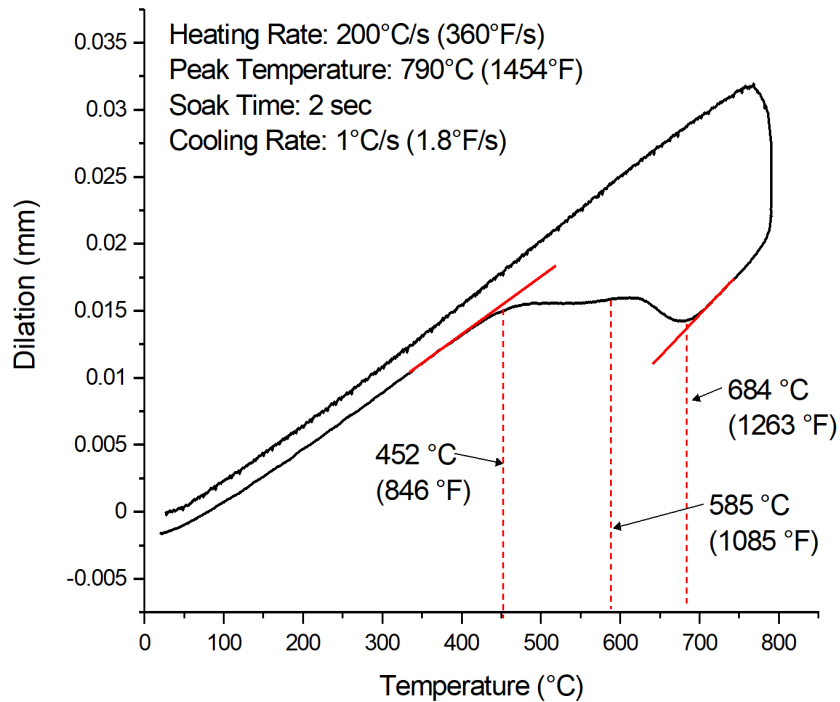


Figure 38. Dilatation curve from a HSLA-100 Gleeble sample heated to a peak temperature of 790 °C and cooled at 1 °C/s.

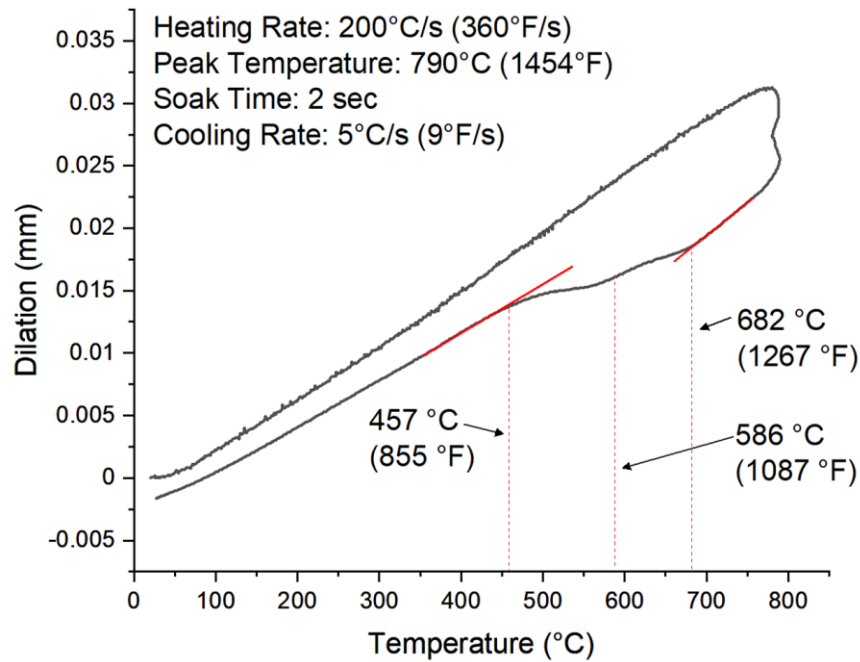


Figure 39. Dilatation curve from a HSLA-100 Gleeble sample heated to a peak temperature of 790 °C and cooled at 5 °C/s.

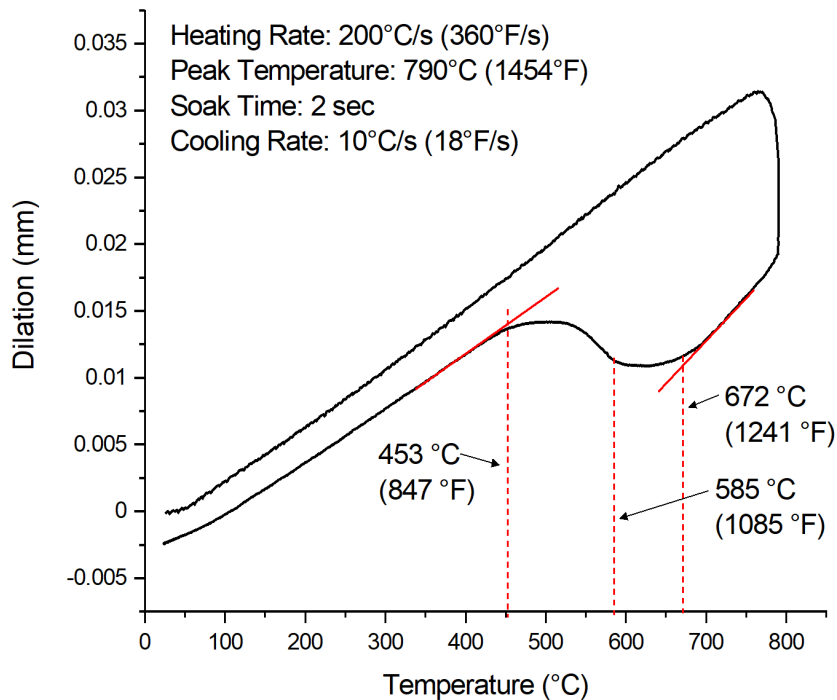


Figure 40. Dilatation curve from a HSLA-100 Gleeble sample heated to a peak temperature of 790 °C and cooled at 10 °C/s.

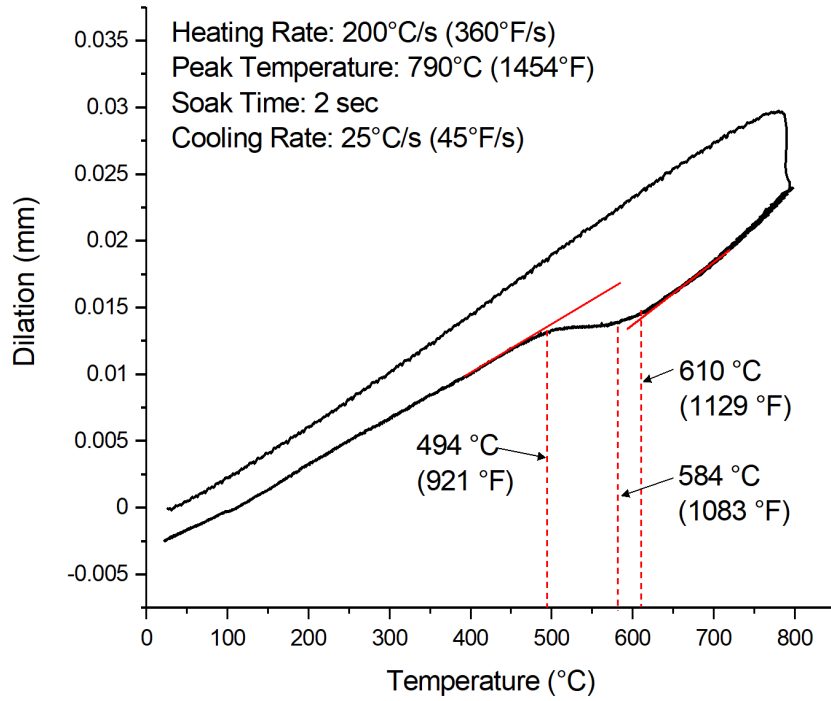


Figure 41. Dilation curve from a HSLA-100 Gleeble sample heated to a peak temperature of 790 °C and cooled at 25 °C/s.

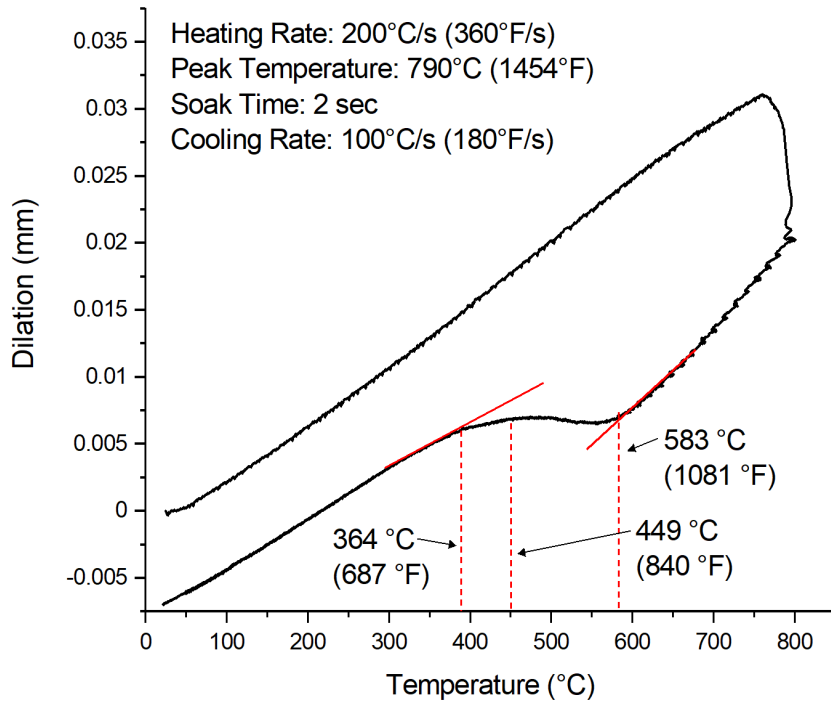


Figure 42. Dilation curve from a HSLA-100 Gleeble sample heated to a peak temperature of 790 °C and cooled at 100 °C/s.

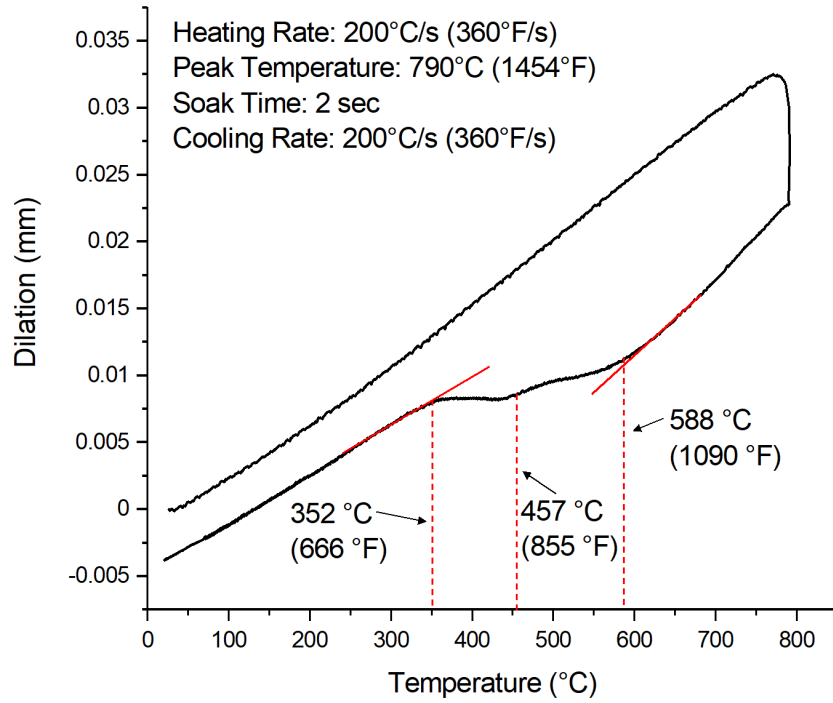


Figure 43. Dilation curve from a HSLA-100 Gleeble sample heated to a peak temperature of 790 °C and cooled at 200 °C/s.

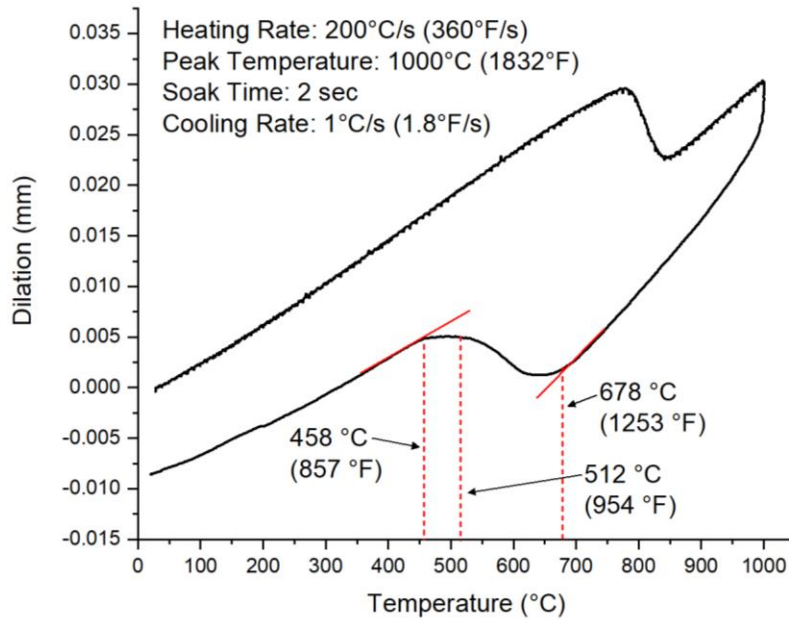


Figure 44. Dilation curve from a HSLA-100 Gleeble sample heated to a peak temperature of 1000 °C and cooled at 1 °C/s.

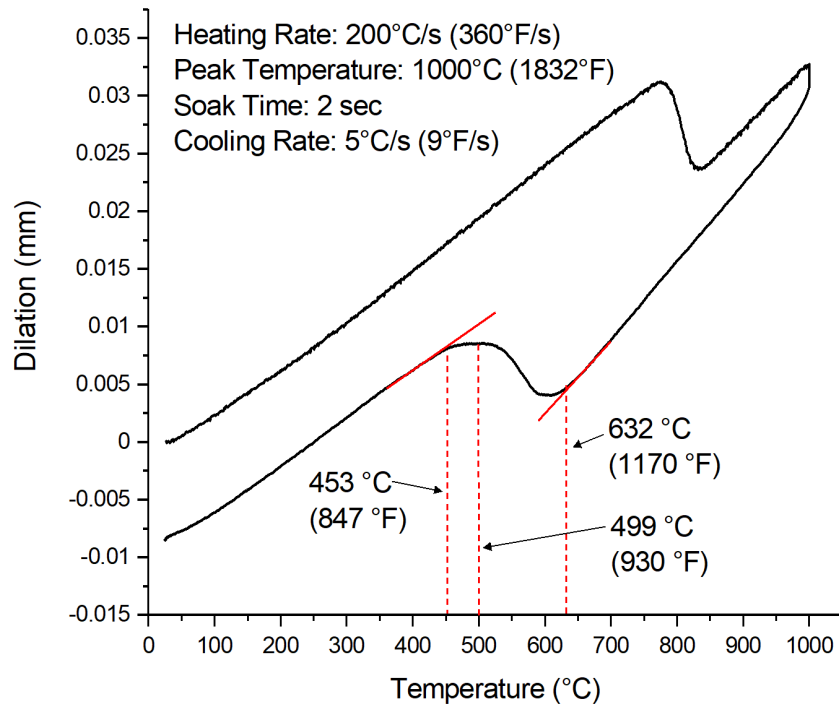


Figure 45. Dilatation curve from a HSLA-100 Gleeble sample heated to a peak temperature of 1000 °C and cooled at 5 °C/s.

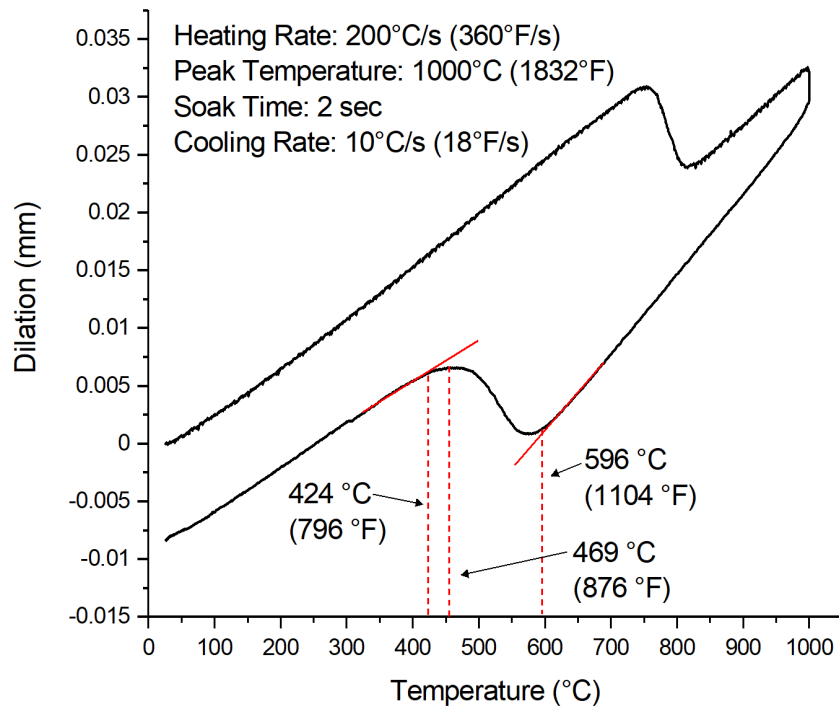


Figure 46. Dilatation curve from a HSLA-100 Gleeble sample heated to a peak temperature of 1000 °C and cooled at 10 °C/s.

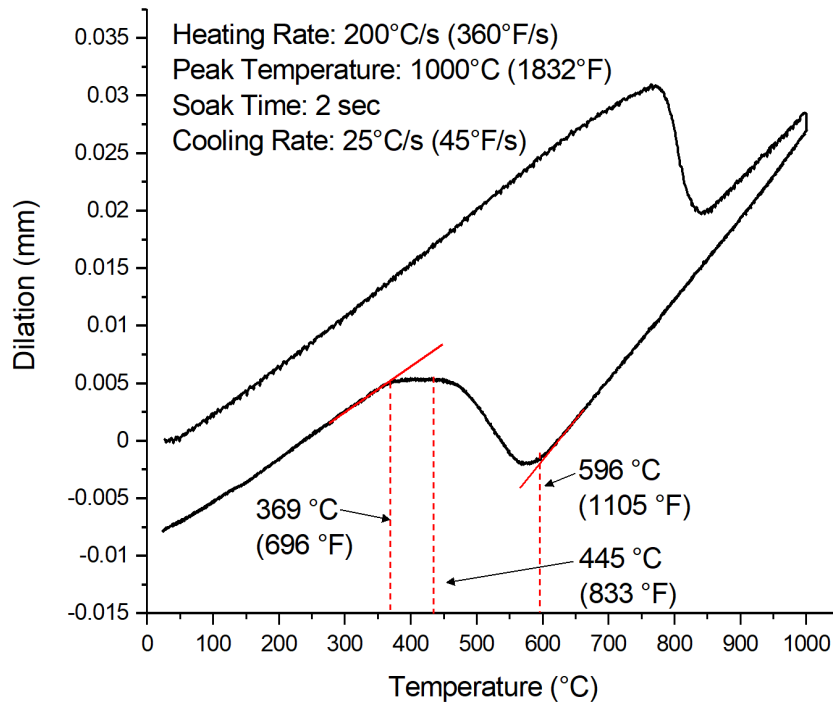


Figure 47. Dilatation curve from a HSLA-100 Gleeble sample heated to a peak temperature of 1000 °C and cooled at 25 °C/s.

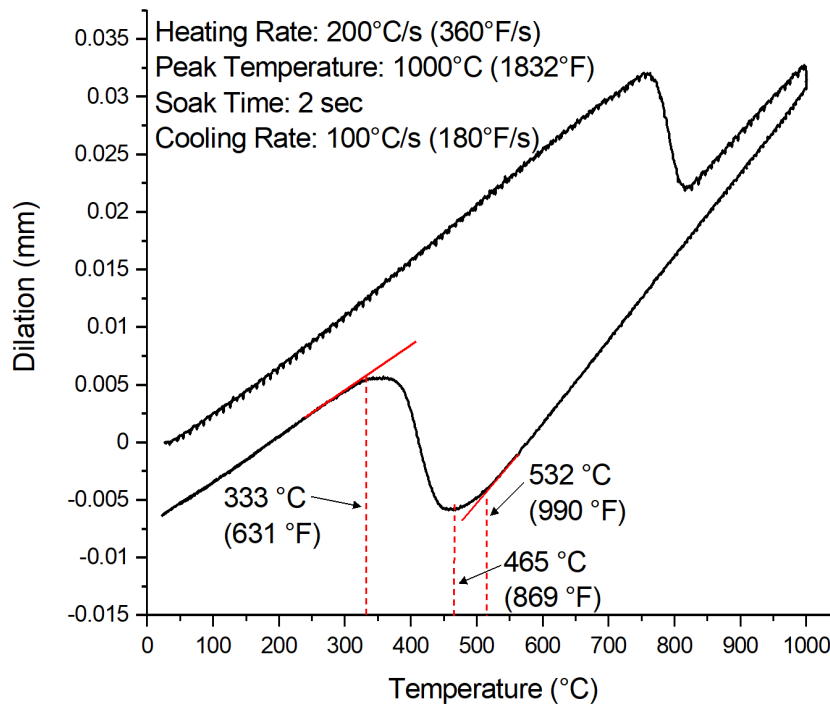


Figure 48. Dilatation curve from a HSLA-100 Gleeble sample heated to a peak temperature of 1000 °C and cooled at 100 °C/s.

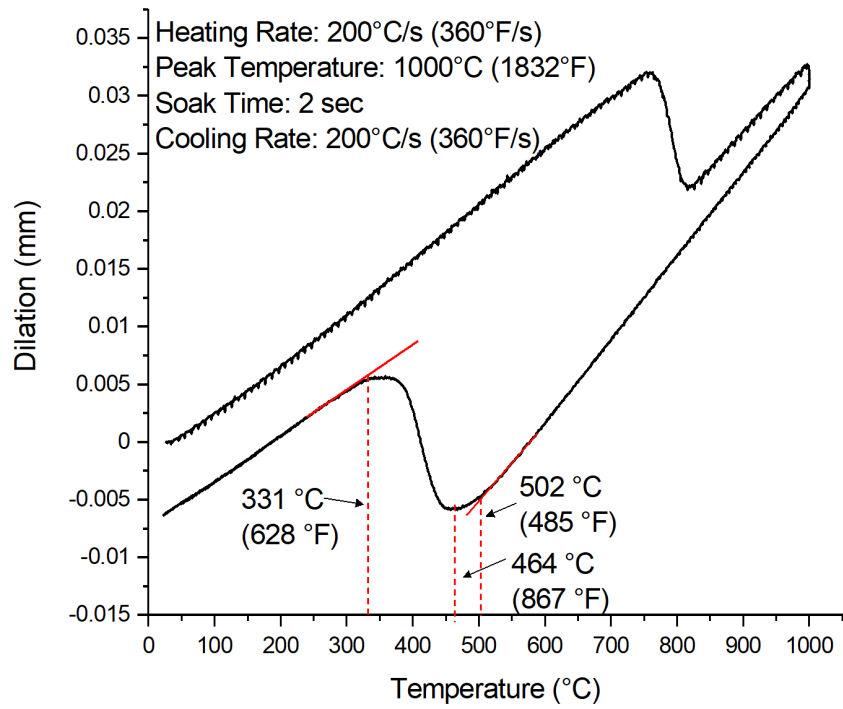


Figure 49. Dilatation curve from a HSLA-100 Gleeble sample heated to a peak temperature of 1000 °C and cooled at 200 °C/s.

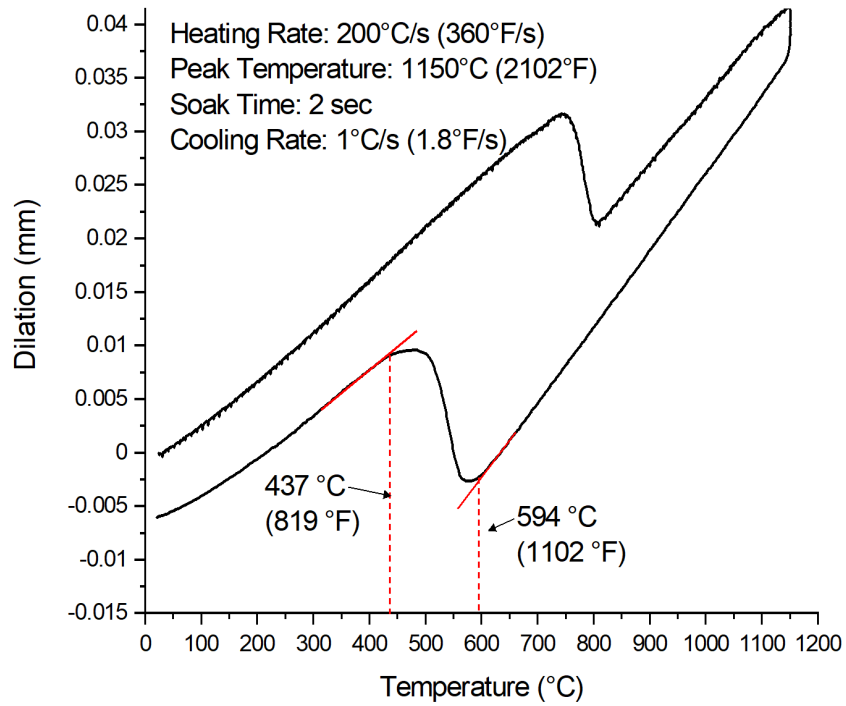


Figure 50. Dilatation curve from a HSLA-100 Gleeble sample heated to a peak temperature of 1150 °C and cooled at 1 °C/s.

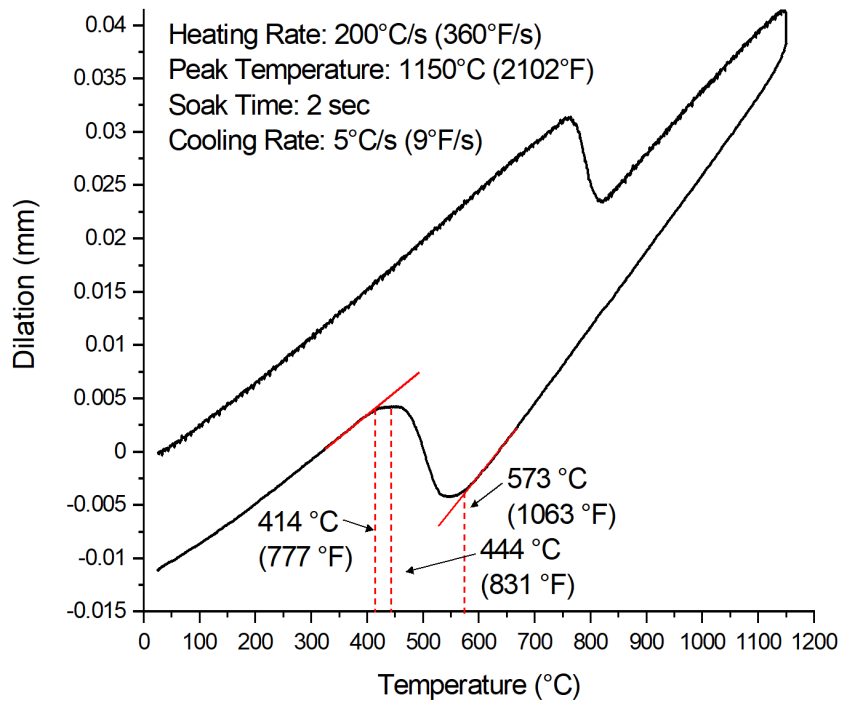


Figure 51. Dilatation curve from a HSLA-100 Gleeble sample heated to a peak temperature of 1150 °C and cooled at 5 °C/s.

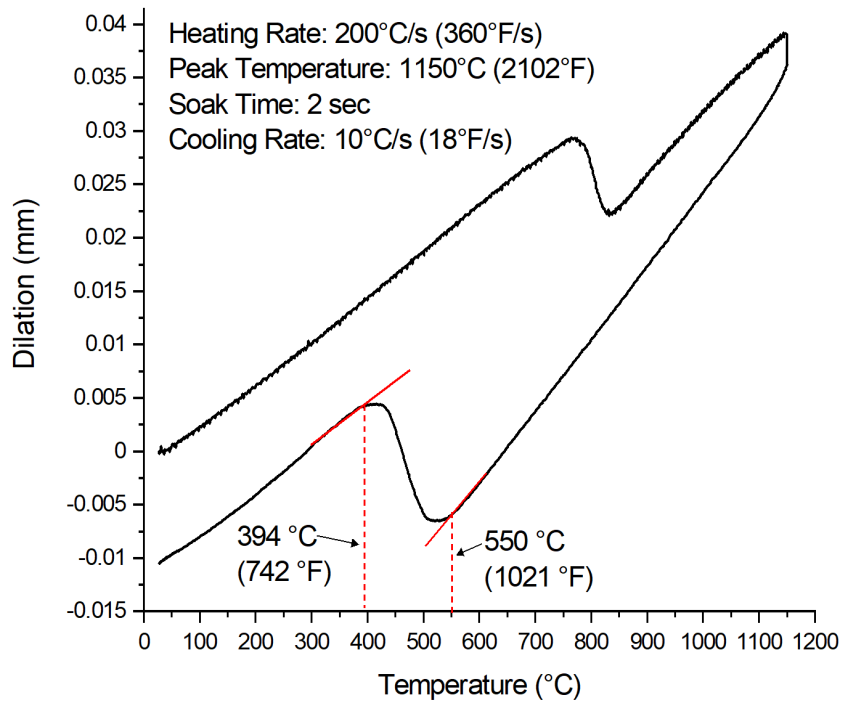


Figure 52. Dilatation curve from a HSLA-100 Gleeble sample heated to a peak temperature of 1150 °C and cooled at 10 °C/s.

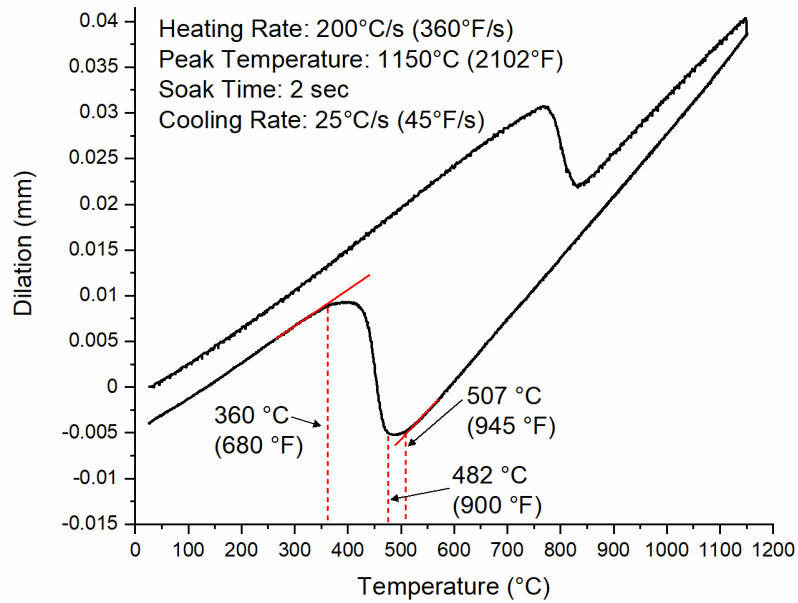


Figure 53. Dilatation curve from a HSLA-100 Gleeble sample heated to a peak temperature of 1150 °C and cooled at 25 °C/s.

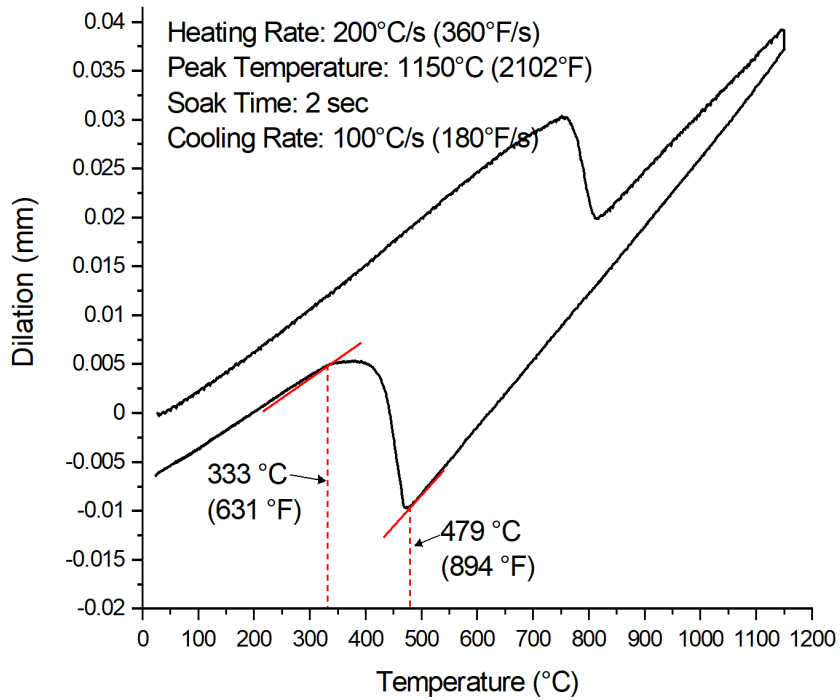


Figure 54. Dilatation curve from a HSLA-100 Gleeble sample heated to a peak temperature of 1150 °C and cooled at 100 °C/s.

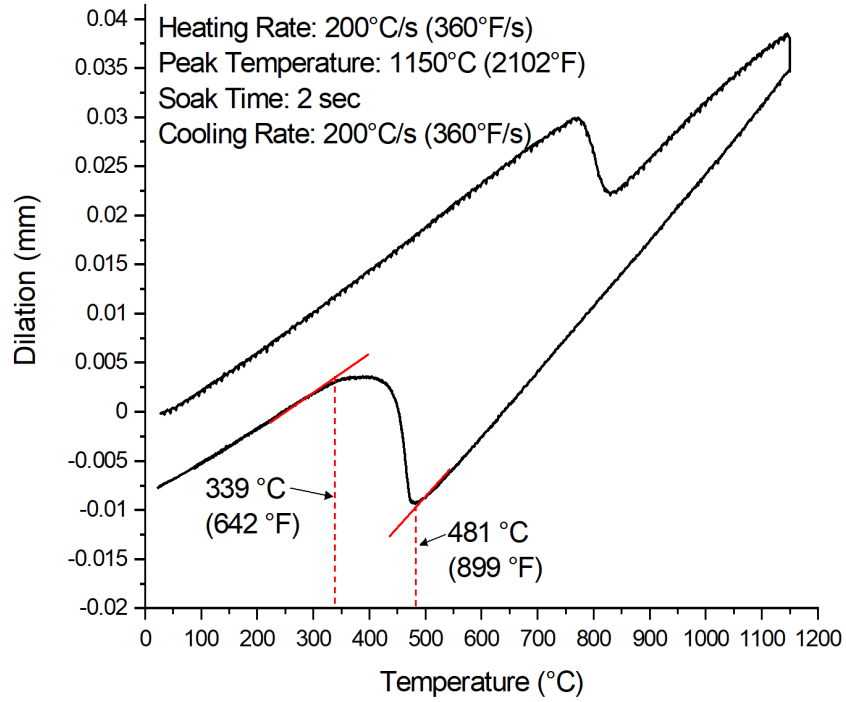


Figure 55. Dilation curve from a HSLA-100 Gleeble sample heated to a peak temperature of 1150 °C and cooled at 200 °C/s.

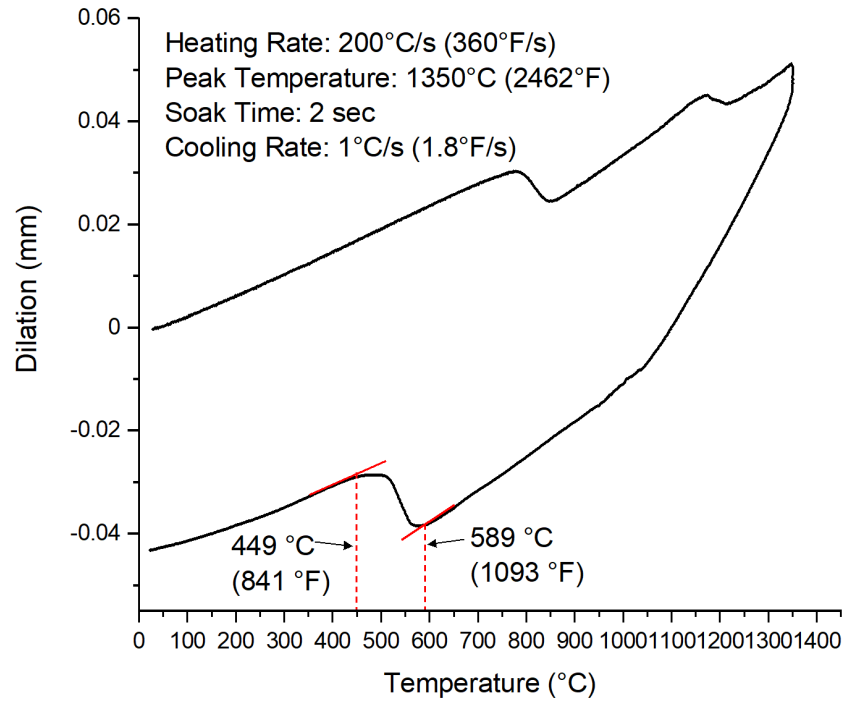


Figure 56. Dilation curve from a HSLA-100 Gleeble sample heated to a peak temperature of 1350 °C and cooled at 1 °C/s.

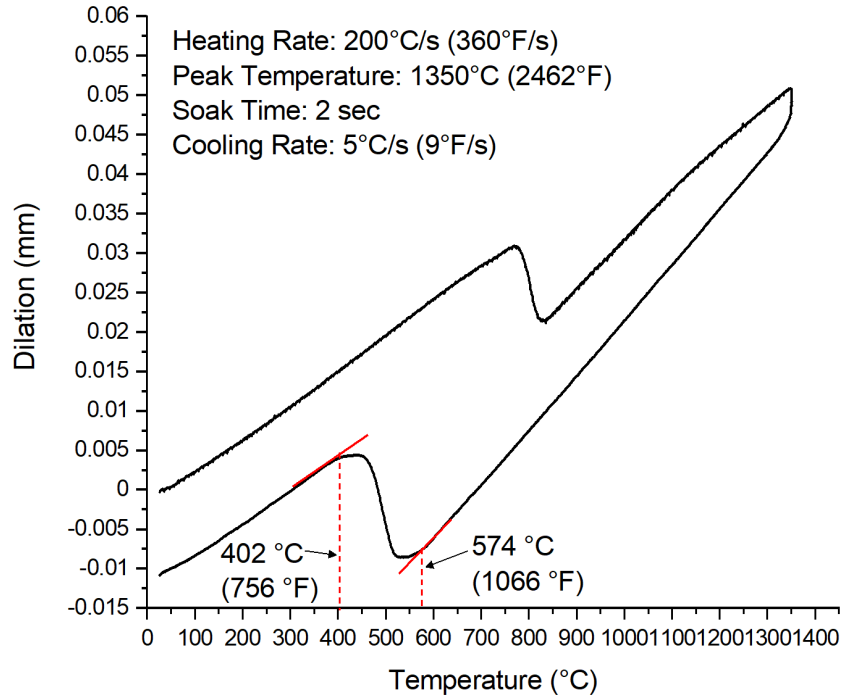


Figure 57. Dilatation curve from a HSLA-100 Gleeble sample heated to a peak temperature of 1350 °C and cooled at 5 °C/s.

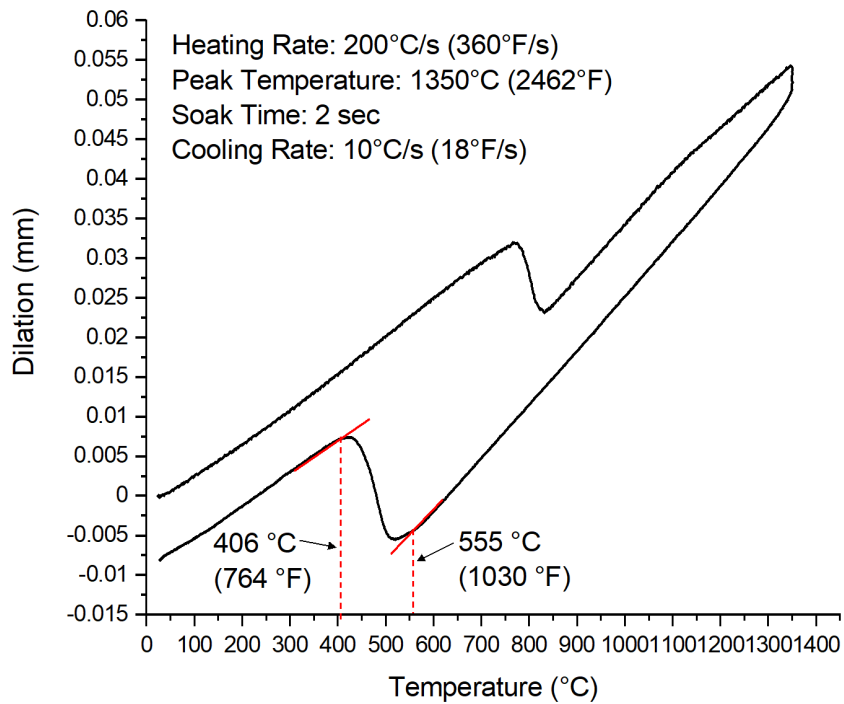


Figure 58. Dilatation curve from a HSLA-100 Gleeble sample heated to a peak temperature of 1350 °C and cooled at 10 °C/s.

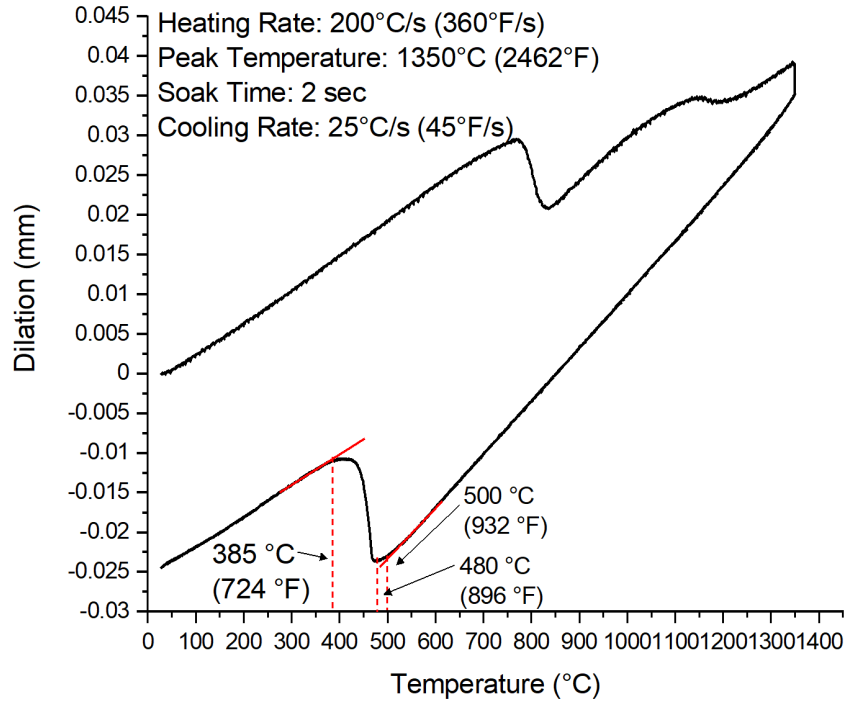


Figure 59. Dilatation curve from a HSLA-100 Gleeble sample heated to a peak temperature of 1350 °C and cooled at 25 °C/s.

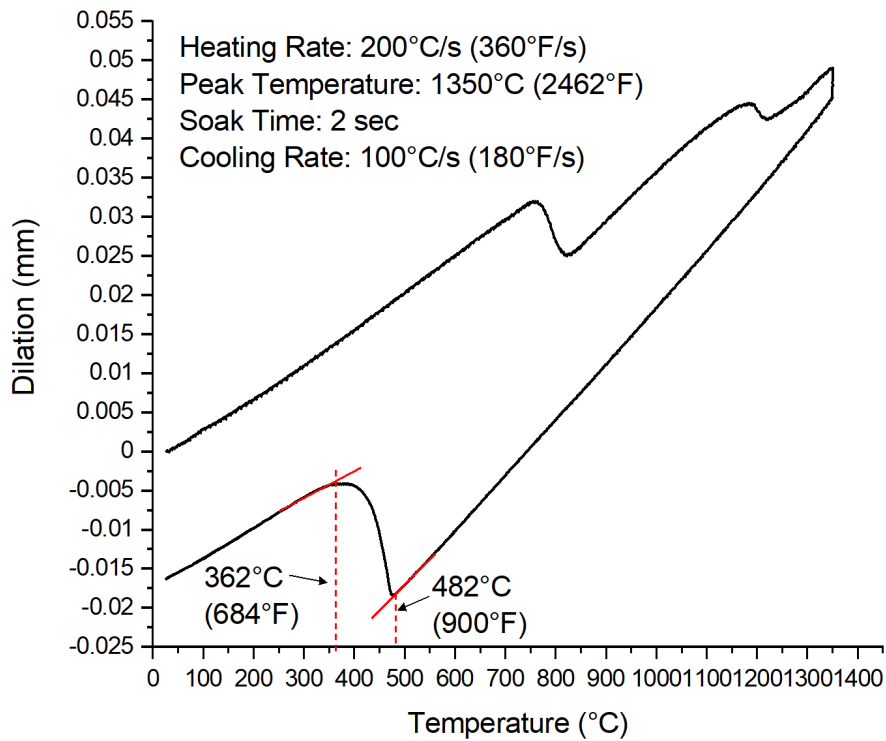


Figure 60. Dilatation curve from a HSLA-100 Gleeble sample heated to a peak temperature of 1350 °C and cooled at 100 °C/s.

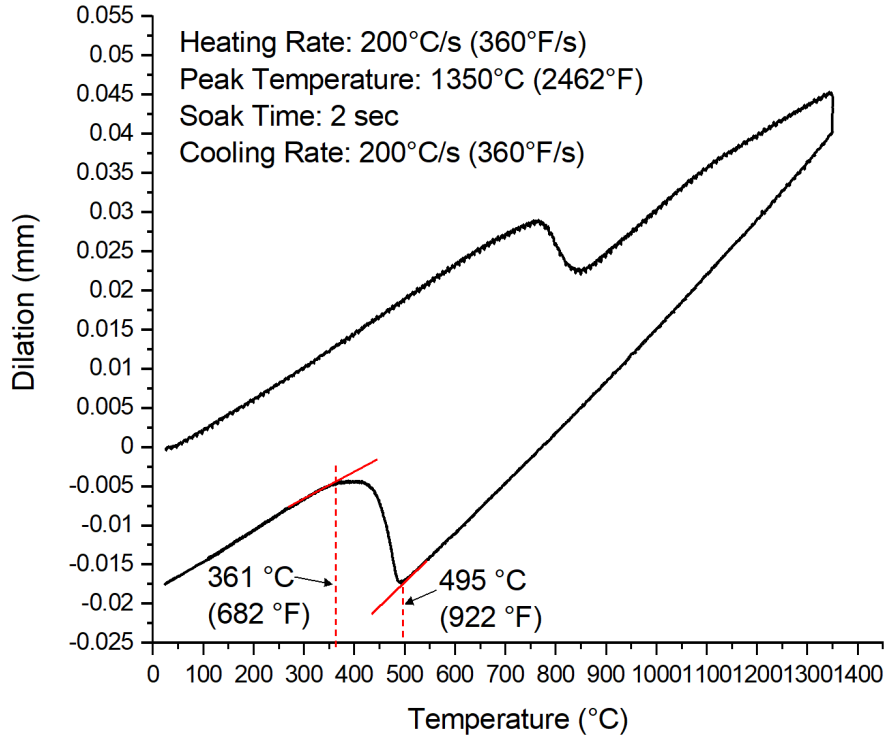


Figure 61. Dilatation curve from a HSLA-100 Gleeble sample heated to a peak temperature of 1350 °C and cooled at 200 °C/s.

Appendix C: Representative Microstructures of HSLA-100 CCT Specimens

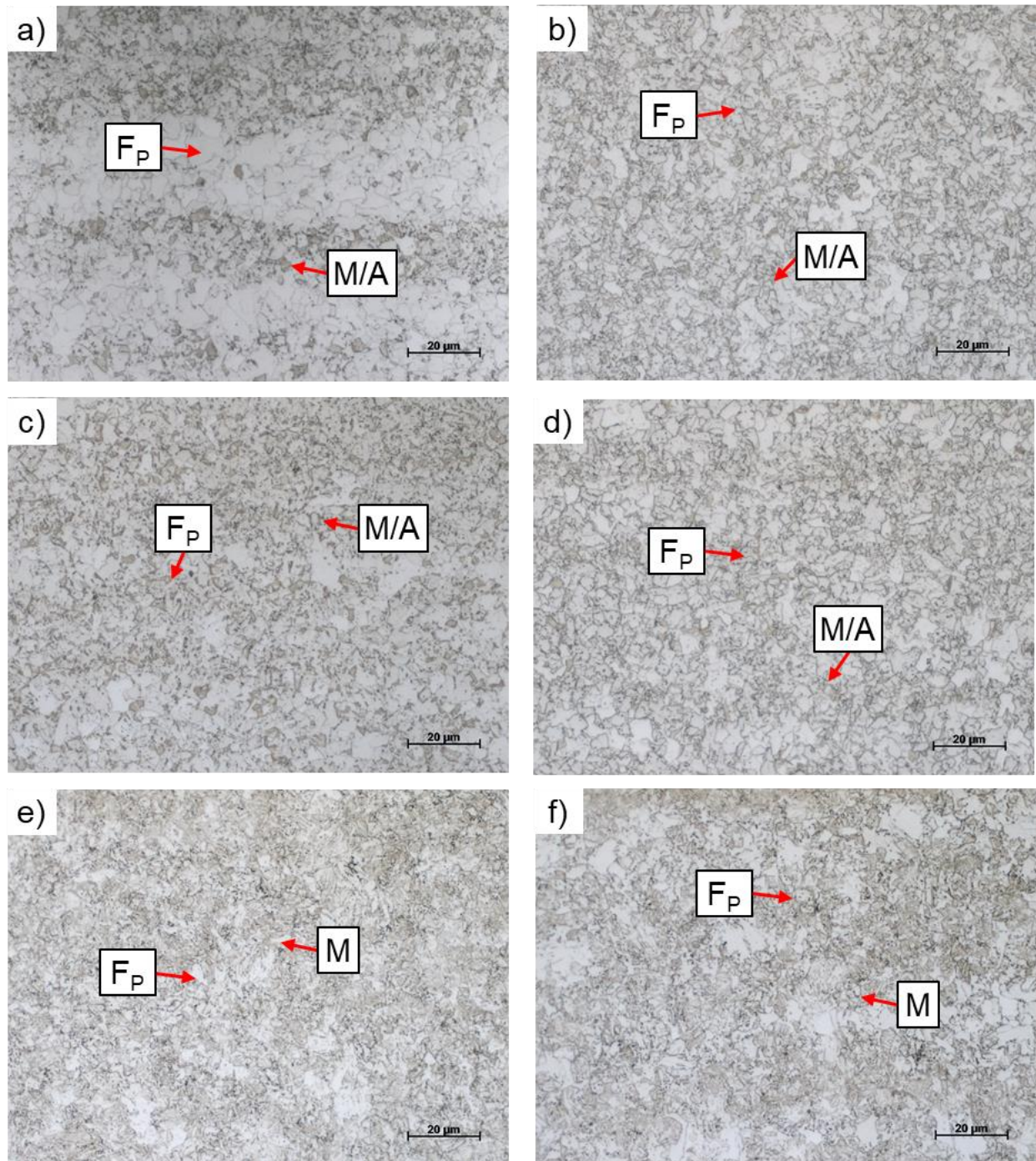


Figure 62. Representative microstructures from HSLA-100 dilatometry specimens heated to a peak temperature of 790 °C (1454 °F) and continuously cooled at various rates. (a-f): 1, 5, 10, 25, 100, and 200 °C/s (1.8, 9, 18, 45, 180, and 360 °F/s).

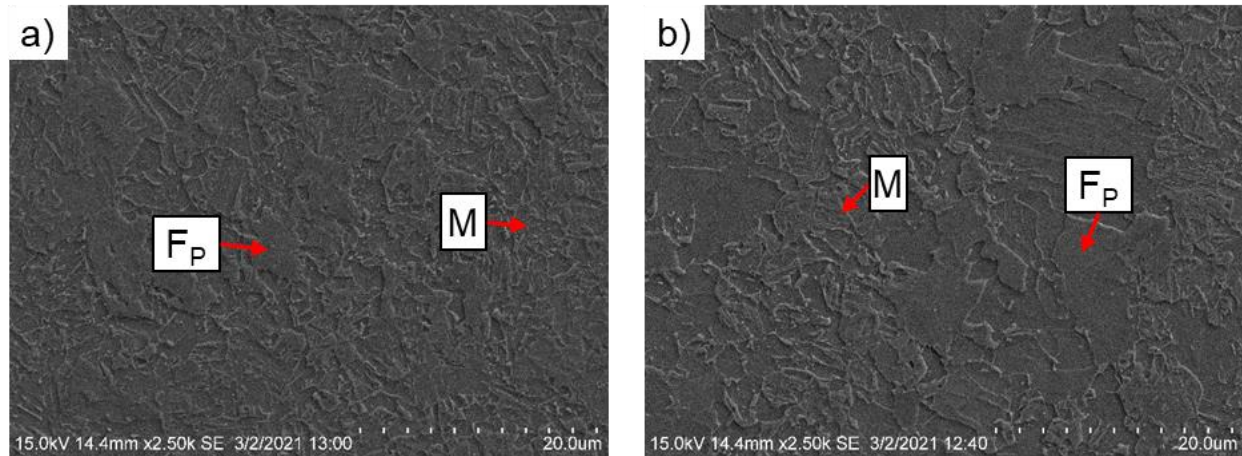


Figure 63. SEM images showing representative microstructures of HSLA-100 dilatometry specimens heated to a peak temperature of 790 °C (1454 °F) and continuously cooled at **a)** 100 °C/s (180 °F/s), and **b)** 200 °C/s (360 °F/s).

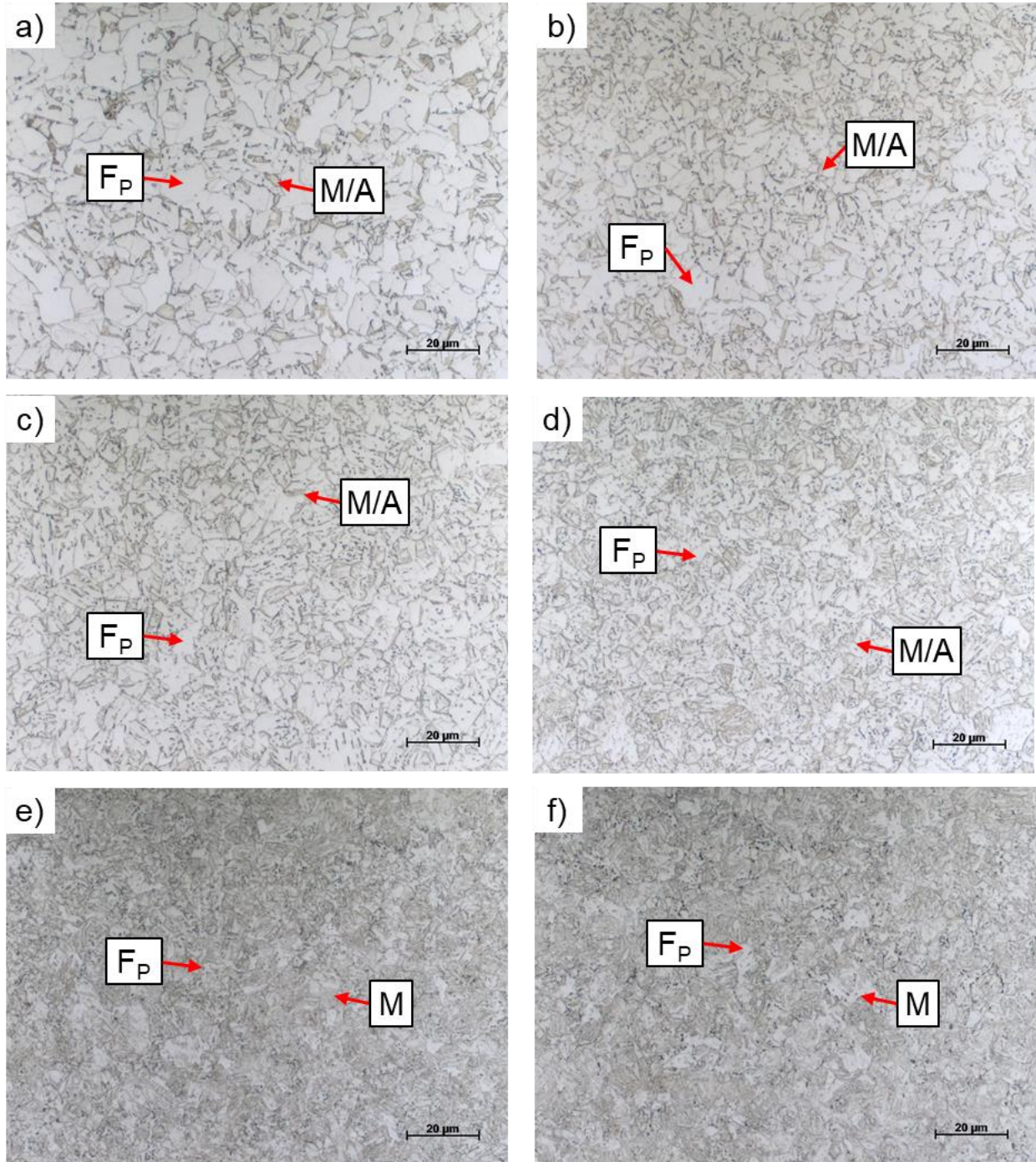


Figure 64. Representative microstructures from HSLA-100 dilatometry specimen heated to a peak temperature of 1000 °C (1832 °F) and continuously cooled at various rates. (a-f): 1, 5, 10, 25, 100, and 200 °C/s (1.8, 9, 18, 45, 180, and 360 °F/s).

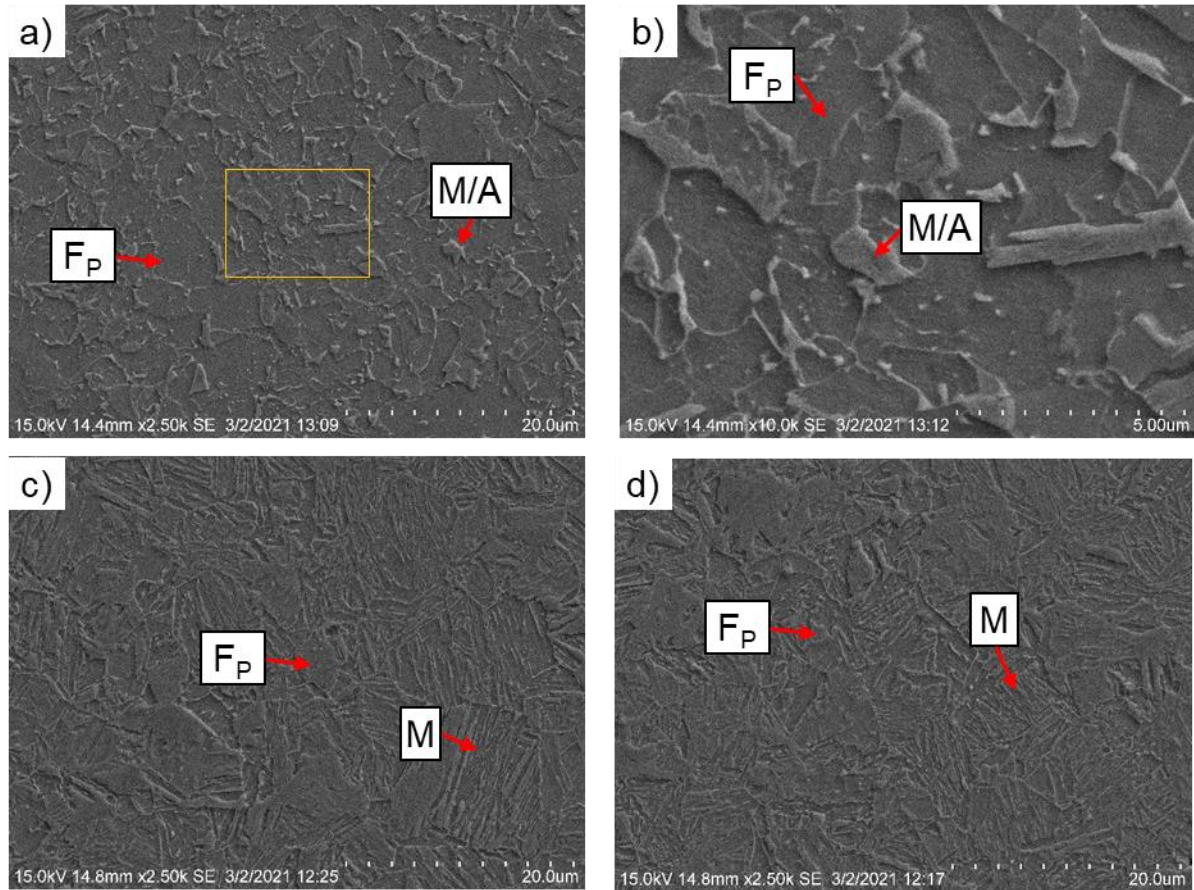


Figure 65. SEM images showing representative microstructures of HSLA-100 dilatometry specimens heated to a peak temperature of 1000 °C (1832 °F) and continuously cooled at: **a, b**) 25 °C/s (45 °F/s), **c**) 100 °C/s (180 °F/s), and **d**) 200 °C/s (360 °F/s). Note the yellow box in **a**) is the region highlighted at greater magnification in **b**).

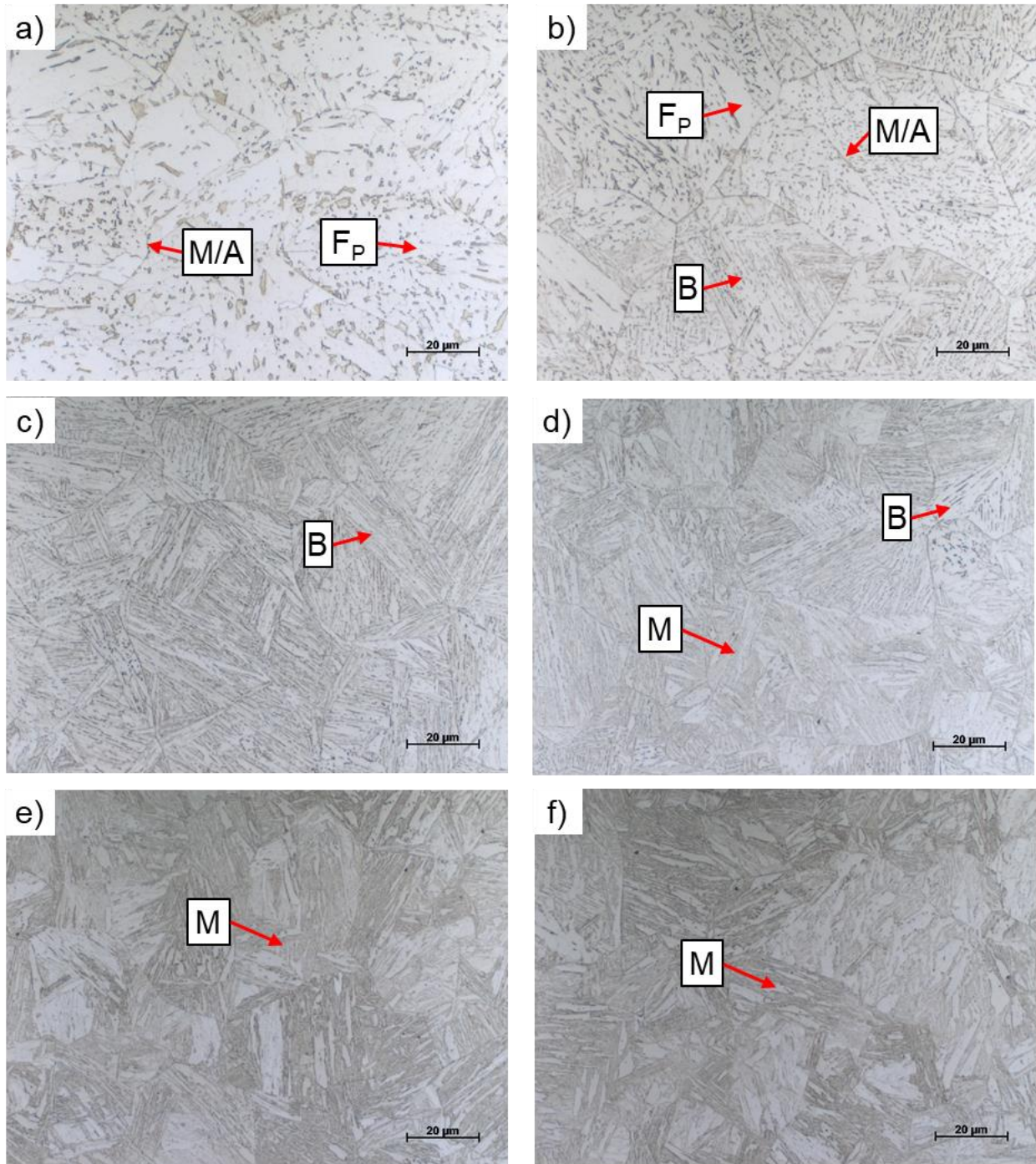


Figure 66. Representative microstructures from HSLA-100 dilatometry specimens heated to a peak temperature of 1150 °C (2102 °F) and continuously cooled at various rates. (a-f): 1, 5, 10, 25, 100, and 200 °C/s (1.8, 9, 18, 45, 180, and 360 °F/s).

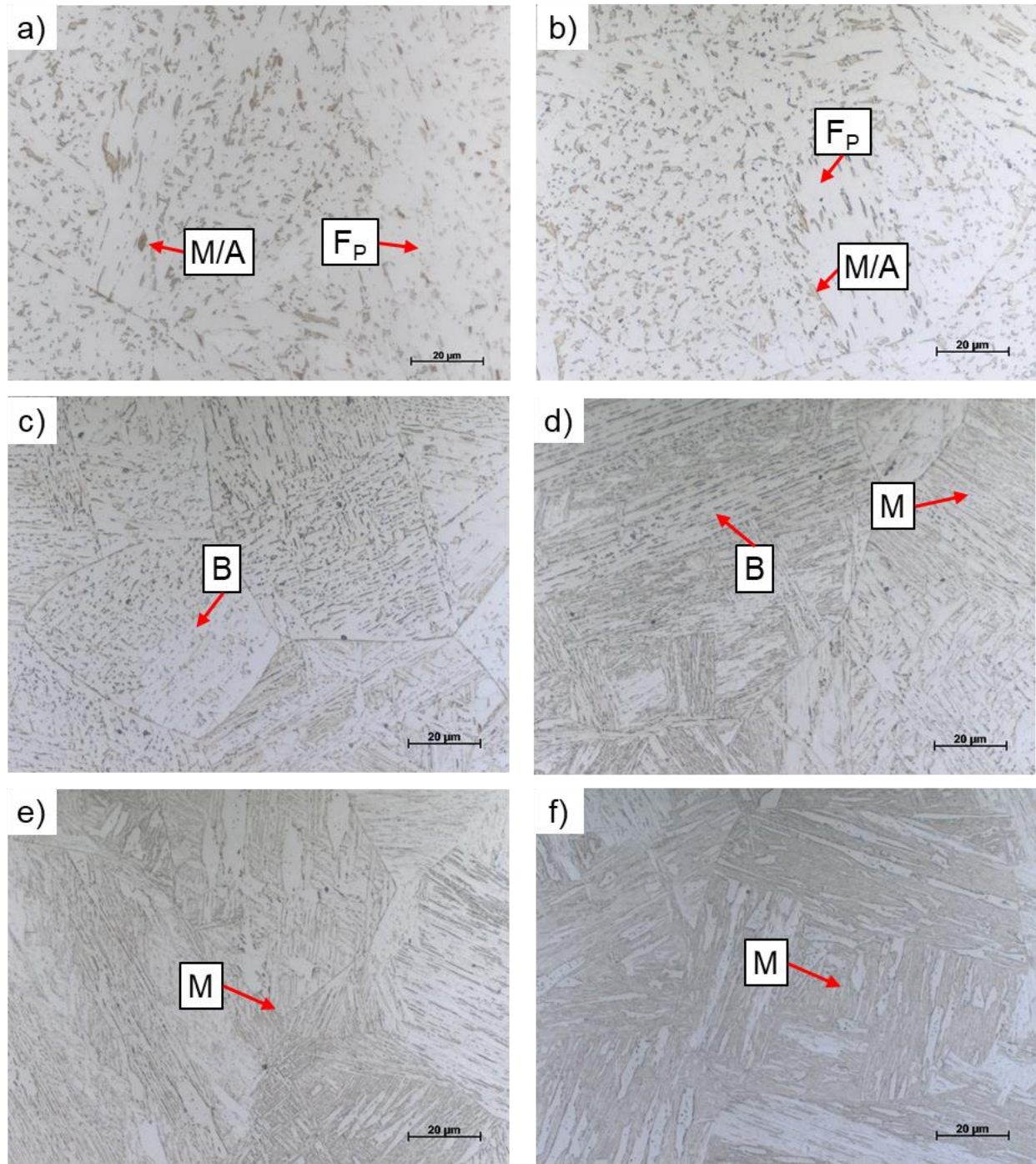


Figure 67. Representative microstructures from HSLA-100 dilatometry specimens heated to a peak temperature of 1350 °C (2462 °F) and continuously cooled at various rates. (a-f): 1, 5, 10, 25, 100, and 200 °C/s (1.8, 9, 18, 45, 180, and 360 °F/s).

Appendix D: Microhardness Measurements**Table 14.** Vickers Microhardness of HSLA-100 as a Function of Peak Temperature and Cooling Rate. Note: Errors are one standard deviation and values in parenthesis are the number of indents measured.

Cooling Rate		Peak Temperature				
		°C	790	1000	1150	1350
°C/s	°F/s	°F	1454	1832	2102	2462
1	1.8	242 ± 18 (18)	230 ± 13 (7)	239 ± 12 (8)	236 ± 13 (65)	
5	9	254 ± 12 (30)	251 ± 10 (7)	268 ± 25 (10)	240 ± 11 (5)	
10	18	249 ± 9 (21)	251 ± 12 (10)	298 ± 14 (10)	266 ± 13 (8)	
25	45	252 ± 16 (30)	280 ± 12 (10)	313 ± 16 (6)	310 ± 9 (12)	
100	180	285 ± 19 (6)	331 ± 9 (10)	327 ± 12 (6)	323 ± 8 (12)	
200	360	287 ± 17 (6)	326 ± 19 (10)	323 ± 17 (6)	335 ± 8 (12)	

Table 15. Vickers Microhardness Measurements across the Experimental Butt Joint Weldment Illustrated in **Figure 20** (Coordinate Frame Origin at Top Left)

Hardness (HV ₂₀₀)	X Coord. (µm)	Y Coord. (µm)	Hardness (HV ₂₀₀)	X Coord. (µm)	Y Coord. (µm)	Hardness (HV ₂₀₀)	X Coord. (µm)	Y Coord. (µm)
232	0	0	245	11750	-250	236	11750	-500
234	250	0	N/A	11699	132	245	12000	-500
231	500	0	N/A	11999	135	270	12250	-500
234	750	0	203	12299	138	273	12500	-500
241	1000	0	207	12599	142	275	12750	-500
254	1250	0	217	12899	145	266	13000	-500
257	1500	0	218	13199	148	252	13250	-500
224	1750	0	211	13499	152	239	13500	-500
234	2000	0	222	13799	155	253	13750	-500
246	2250	0	211	14099	158	240	14000	-500
231	2500	0	222	14399	162	227	14250	-500
252	2750	0	201	14699	166	228	14500	-500
241	12250	0	214	14999	168	246	14750	-500
239	12500	0	210	15299	172	243	14750	-750
234	12750	0	221	15599	176	252	14500	-750
264	13000	0	208	15898	179	248	14250	-750
255	13250	0	226	16198	182	238	14000	-750
241	13500	0	223	16498	186	251	13750	-750
240	13750	0	225	16798	189	247	13500	-750
241	14000	0	229	17098	192	249	13250	-750
236	14250	0	244	17398	196	256	13000	-750
235	14500	0	224	17698	199	268	12750	-750
238	14750	0	225	17998	202	274	12500	-750
234	14750	-250	229	18298	206	267	12250	-750
244	14500	-250	213	18598	209	284	12000	-750
238	14250	-250	193	18898	212	270	11750	-750
238	14000	-250	249	19198	216	257	11500	-750
236	13750	-250	223	19498	219	243	11250	-750
249	13500	-250	234	19798	222	243	11000	-750
255	13250	-250	241	20098	226	243	10750	-750
276	13000	-250	252	20398	230	248	3750	-750
276	12750	-250	257	20698	232	241	3500	-750
255	12500	-250	267	20998	236	244	3250	-750
234	12250	-250	273	21001	-14	229	3000	-750
248	12000	-250	269	20702	-17	239	2750	-750

Table 15, Continued.

Hardness (HV ₂₀₀)	X Coord. (µm)	Y Coord. (µm)	Hardness (HV ₂₀₀)	X Coord. (µm)	Y Coord. (µm)	Hardness (HV ₂₀₀)	X Coord. (µm)	Y Coord. (µm)
251	2500	-750	286	12000	-1000	259	3250	-1250
268	2250	-750	268	12250	-1000	260	3000	-1250
266	2000	-750	285	12500	-1000	265	2750	-1250
272	1750	-750	263	12750	-1000	274	2500	-1250
268	1500	-750	253	13000	-1000	286	2250	-1250
242	1250	-750	250	13250	-1000	272	2000	-1250
234	1000	-750	240	13500	-1000	259	1750	-1250
249	750	-750	256	13750	-1000	252	1500	-1250
252	500	-750	251	14000	-1000	250	1250	-1250
238	250	-750	253	14250	-1000	246	1000	-1250
231	0	-750	234	14500	-1000	244	750	-1250
255	0	-1000	241	14750	-1000	243	500	-1250
243	250	-1000	243	14750	-1250	238	250	-1250
253	500	-1000	243	14500	-1250	250	0	-1250
248	750	-1000	243	14250	-1250	245	0	-1500
246	1000	-1000	246	14000	-1250	250	250	-1500
251	1250	-1000	243	13750	-1250	245	500	-1500
251	1500	-1000	243	13500	-1250	234	750	-1500
261	1750	-1000	252	13250	-1250	245	1000	-1500
266	2000	-1000	249	13000	-1250	254	1250	-1500
281	2250	-1000	260	12750	-1250	249	1500	-1500
271	2500	-1000	249	12500	-1250	244	1750	-1500
259	2750	-1000	280	12250	-1250	254	2000	-1500
241	3000	-1000	282	12000	-1250	281	2250	-1500
253	3250	-1000	269	11750	-1250	278	2500	-1500
234	3500	-1000	263	11500	-1250	275	2750	-1500
232	3750	-1000	297	11250	-1250	273	3000	-1500
246	4000	-1000	293	11000	-1250	300	3250	-1500
253	4250	-1000	262	10750	-1250	271	3500	-1500
245	4500	-1000	237	10500	-1250	285	3750	-1500
252	4750	-1000	239	5000	-1250	274	4000	-1500
225	10500	-1000	247	4750	-1250	250	4250	-1500
228	10750	-1000	240	4500	-1250	243	4500	-1500
249	11000	-1000	243	4250	-1250	239	4750	-1500
271	11250	-1000	242	4000	-1250	238	5000	-1500
287	11500	-1000	281	3750	-1250	236	10250	-1500
283	11750	-1000	259	3500	-1250	243	10500	-1500

Table 15, Continued.

Hardness (HV ₂₀₀)	X Coord. (µm)	Y Coord. (µm)	Hardness (HV ₂₀₀)	X Coord. (µm)	Y Coord. (µm)	Hardness (HV ₂₀₀)	X Coord. (µm)	Y Coord. (µm)
298	10750	-1500	241	5750	-1750	278	3250	-2000
265	11000	-1500	239	5500	-1750	292	3500	-2000
272	11250	-1500	248	5250	-1750	293	3750	-2000
280	11500	-1500	245	5000	-1750	266	4000	-2000
282	11750	-1500	235	4750	-1750	282	4250	-2000
267	12000	-1500	249	4500	-1750	287	4500	-2000
272	12250	-1500	266	4250	-1750	253	4750	-2000
254	12500	-1500	274	4000	-1750	246	5000	-2000
252	12750	-1500	274	3750	-1750	239	5250	-2000
245	13000	-1500	253	3500	-1750	245	5500	-2000
246	13250	-1500	278	3250	-1750	242	5750	-2000
247	13500	-1500	310	3000	-1750	242	6000	-2000
248	13750	-1500	271	2750	-1750	244	9750	-2000
247	14000	-1500	280	2500	-1750	249	10000	-2000
243	14250	-1500	268	2250	-1750	283	10250	-2000
246	14500	-1500	253	2000	-1750	309	10500	-2000
252	14750	-1500	245	1750	-1750	303	10750	-2000
249	14750	-1750	249	1500	-1750	299	11000	-2000
252	14500	-1750	231	1250	-1750	286	11250	-2000
245	14250	-1750	243	1000	-1750	301	11500	-2000
249	14000	-1750	252	750	-1750	289	11750	-2000
252	13750	-1750	244	500	-1750	255	12000	-2000
254	13500	-1750	250	250	-1750	263	12250	-2000
251	13250	-1750	247	0	-1750	259	12500	-2000
256	13000	-1750	253	0	-2000	246	12750	-2000
247	12750	-1750	252	250	-2000	254	13000	-2000
253	12500	-1750	243	500	-2000	249	13250	-2000
258	12250	-1750	255	750	-2000	239	13500	-2000
268	12000	-1750	254	1000	-2000	246	13750	-2000
285	11750	-1750	262	1250	-2000	245	14000	-2000
291	11500	-1750	263	1500	-2000	264	14250	-2000
259	11250	-1750	258	1750	-2000	242	14500	-2000
293	11000	-1750	249	2000	-2000	255	14750	-2000
294	10750	-1750	270	2250	-2000	249	14750	-2250
300	10500	-1750	288	2500	-2000	242	14500	-2250
244	10250	-1750	290	2750	-2000	243	14250	-2250
247	10000	-1750	289	3000	-2000	245	14000	-2250

Table 15, Continued.

Hardness (HV ₂₀₀)	X Coord. (µm)	Y Coord. (µm)	Hardness (HV ₂₀₀)	X Coord. (µm)	Y Coord. (µm)	Hardness (HV ₂₀₀)	X Coord. (µm)	Y Coord. (µm)
243	13750	-2250	252	1250	-2250	246	7750	-2500
244	13500	-2250	241	1000	-2250	239	8000	-2500
249	13250	-2250	249	750	-2250	238	8250	-2500
251	13000	-2250	255	500	-2250	245	8500	-2500
245	12750	-2250	249	250	-2250	235	8750	-2500
253	12500	-2250	259	0	-2250	241	9000	-2500
259	12250	-2250	248	0	-2500	241	9250	-2500
260	12000	-2250	247	250	-2500	260	9500	-2500
271	11750	-2250	243	500	-2500	275	9750	-2500
269	11500	-2250	250	750	-2500	299	10000	-2500
283	11250	-2250	252	1000	-2500	297	10250	-2500
295	11000	-2250	254	1250	-2500	306	10500	-2500
311	10750	-2250	255	1500	-2500	280	10750	-2500
303	10500	-2250	255	1750	-2500	281	11000	-2500
313	10250	-2250	262	2000	-2500	294	11250	-2500
292	10000	-2250	272	2250	-2500	281	11500	-2500
249	9750	-2250	279	2500	-2500	273	11750	-2500
247	6250	-2250	263	2750	-2500	278	12000	-2500
243	6000	-2250	263	3000	-2500	254	12250	-2500
240	5750	-2250	284	3250	-2500	254	12500	-2500
246	5500	-2250	284	3500	-2500	249	12750	-2500
241	5250	-2250	273	3750	-2500	245	13000	-2500
262	5000	-2250	293	4000	-2500	246	13250	-2500
283	4750	-2250	298	4250	-2500	255	13500	-2500
296	4500	-2250	298	4500	-2500	246	13750	-2500
333	4250	-2250	269	4750	-2500	247	14000	-2500
336	4000	-2250	243	5000	-2500	241	14250	-2500
359	3750	-2250	234	5250	-2500	238	14500	-2500
353	3500	-2250	244	5500	-2500	250	14750	-2500
321	3250	-2250	245	5750	-2500	249	14750	-2750
298	3000	-2250	234	6000	-2500	246	14500	-2750
286	2750	-2250	241	6250	-2500	245	14250	-2750
290	2500	-2250	242	6500	-2500	253	14000	-2750
265	2250	-2250	239	6750	-2500	245	13750	-2750
262	2000	-2250	238	7000	-2500	250	13500	-2750
249	1750	-2250	247	7250	-2500	243	13250	-2750
240	1500	-2250	247	7500	-2500	254	13000	-2750

Table 15, Continued.

Hardness (HV ₂₀₀)	X Coord. (µm)	Y Coord. (µm)	Hardness (HV ₂₀₀)	X Coord. (µm)	Y Coord. (µm)	Hardness (HV ₂₀₀)	X Coord. (µm)	Y Coord. (µm)
251	12750	-2750	318	3500	-2750	243	5500	-3000
254	12500	-2750	279	3250	-2750	252	5750	-3000
257	12250	-2750	280	3000	-2750	241	6000	-3000
272	12000	-2750	270	2750	-2750	247	6250	-3000
272	11750	-2750	255	2500	-2750	243	6500	-3000
268	11500	-2750	257	2250	-2750	241	6750	-3000
281	11250	-2750	259	2000	-2750	252	7000	-3000
283	11000	-2750	249	1750	-2750	243	7250	-3000
263	10750	-2750	252	1500	-2750	246	7500	-3000
263	10500	-2750	258	1250	-2750	240	7750	-3000
276	10250	-2750	255	1000	-2750	243	8000	-3000
257	10000	-2750	249	750	-2750	244	8250	-3000
248	9750	-2750	262	500	-2750	238	8500	-3000
246	9500	-2750	250	250	-2750	252	8750	-3000
252	9250	-2750	237	0	-2750	244	9000	-3000
234	9000	-2750	247	0	-3000	243	9250	-3000
243	8750	-2750	246	250	-3000	250	9500	-3000
246	8500	-2750	242	500	-3000	243	9750	-3000
238	8250	-2750	243	750	-3000	248	10000	-3000
241	8000	-2750	253	1000	-3000	243	10250	-3000
241	7750	-2750	253	1250	-3000	264	10500	-3000
243	7500	-2750	255	1500	-3000	265	10750	-3000
238	7250	-2750	255	1750	-3000	288	11000	-3000
240	7000	-2750	261	2000	-3000	274	11250	-3000
240	6750	-2750	261	2250	-3000	278	11500	-3000
246	6500	-2750	269	2500	-3000	260	11750	-3000
240	6250	-2750	267	2750	-3000	265	12000	-3000
246	6000	-2750	268	3000	-3000	271	12250	-3000
236	5750	-2750	266	3250	-3000	258	12500	-3000
249	5500	-2750	282	3500	-3000	251	12750	-3000
240	5250	-2750	268	3750	-3000	253	13000	-3000
247	5000	-2750	245	4000	-3000	245	13250	-3000
238	4750	-2750	237	4250	-3000	247	13500	-3000
234	4500	-2750	242	4500	-3000	245	13750	-3000
273	4250	-2750	253	4750	-3000	240	14000	-3000
298	4000	-2750	243	5000	-3000	243	14250	-3000
289	3750	-2750	241	5250	-3000	244	14500	-3000

Table 15, Continued.

Hardness (HV ₂₀₀)	X Coord. (µm)	Y Coord. (µm)	Hardness (HV ₂₀₀)	X Coord. (µm)	Y Coord. (µm)	Hardness (HV ₂₀₀)	X Coord. (µm)	Y Coord. (µm)
250	14750	-3000	252	5750	-3250	252	3250	-3500
236	14750	-3250	249	5500	-3250	245	3500	-3500
216	14500	-3250	249	5250	-3250	249	3750	-3500
228	14250	-3250	251	5000	-3250	256	4000	-3500
227	14000	-3250	241	4750	-3250	263	4250	-3500
233	13750	-3250	241	4500	-3250	251	4500	-3500
240	13500	-3250	243	4250	-3250	247	4750	-3500
249	13250	-3250	243	4000	-3250	238	5000	-3500
245	13000	-3250	245	3750	-3250	247	5250	-3500
236	12750	-3250	242	3500	-3250	240	5500	-3500
249	12500	-3250	260	3250	-3250	252	5750	-3500
238	12250	-3250	253	3000	-3250	248	6000	-3500
257	12000	-3250	263	2750	-3250	250	6250	-3500
255	11750	-3250	250	2500	-3250	243	6500	-3500
254	11500	-3250	246	2250	-3250	246	6750	-3500
257	11250	-3250	264	2000	-3250	243	7000	-3500
246	11000	-3250	254	1750	-3250	252	7250	-3500
252	10750	-3250	253	1500	-3250	246	7500	-3500
244	10500	-3250	251	1250	-3250	249	7750	-3500
246	10250	-3250	255	1000	-3250	246	8000	-3500
246	10000	-3250	253	750	-3250	247	8250	-3500
247	9750	-3250	249	500	-3250	246	8500	-3500
246	9500	-3250	234	250	-3250	246	8750	-3500
243	9250	-3250	249	0	-3250	242	9000	-3500
246	9000	-3250	231	0	-3500	243	9250	-3500
245	8750	-3250	259	250	-3500	251	9500	-3500
252	8500	-3250	248	500	-3500	246	9750	-3500
244	8250	-3250	239	750	-3500	241	10000	-3500
246	8000	-3250	245	1000	-3500	247	10250	-3500
246	7750	-3250	252	1250	-3500	247	10500	-3500
246	7500	-3250	272	1500	-3500	246	10750	-3500
249	7250	-3250	250	1750	-3500	248	11000	-3500
247	7000	-3250	252	2000	-3500	256	11250	-3500
250	6750	-3250	257	2250	-3500	241	11500	-3500
249	6500	-3250	263	2500	-3500	252	11750	-3500
246	6250	-3250	259	2750	-3500	255	12000	-3500
248	6000	-3250	243	3000	-3500	256	12250	-3500

Table 15, Continued.

Hardness (HV ₂₀₀)	X Coord. (µm)	Y Coord. (µm)	Hardness (HV ₂₀₀)	X Coord. (µm)	Y Coord. (µm)	Hardness (HV ₂₀₀)	X Coord. (µm)	Y Coord. (µm)
253	12500	-3500	252	1500	-3750	238	14500	-4000
260	12750	-3500	255	1250	-3750	243	14750	-4000
251	13000	-3500	255	1000	-3750	226	14750	-4250
249	13250	-3500	249	750	-3750	232	14500	-4250
251	13500	-3500	253	500	-3750	236	14250	-4250
246	13750	-3500	243	250	-3750	235	14000	-4250
250	14000	-3500	255	0	-3750	243	13750	-4250
248	14250	-3500	246	0	-4000	249	13500	-4250
226	14500	-3500	236	250	-4000	244	13250	-4250
249	14750	-3500	239	500	-4000	244	13000	-4250
240	14750	-3750	244	750	-4000	243	12750	-4250
243	14500	-3750	244	1000	-4000	263	12500	-4250
254	14250	-3750	249	1250	-4000	246	12250	-4250
243	14000	-3750	250	1500	-4000	241	12000	-4250
241	13750	-3750	246	1750	-4000	249	4000	-4250
250	13500	-3750	229	2000	-4000	242	3750	-4250
247	13250	-3750	250	2250	-4000	253	3500	-4250
252	13000	-3750	248	2500	-4000	246	3250	-4250
258	12750	-3750	249	2750	-4000	257	3000	-4250
252	12500	-3750	255	3000	-4000	262	2750	-4250
259	12250	-3750	251	3250	-4000	249	2500	-4250
245	12000	-3750	251	3500	-4000	243	2250	-4250
255	11750	-3750	247	3750	-4000	253	2000	-4250
255	11500	-3750	244	4000	-4000	247	1750	-4250
246	11250	-3750	251	4250	-4000	240	1500	-4250
248	11000	-3750	246	11500	-4000	241	1250	-4250
247	4250	-3750	236	11750	-4000	241	1000	-4250
255	4000	-3750	249	12000	-4000	242	750	-4250
248	3750	-3750	262	12250	-4000	235	500	-4250
257	3500	-3750	241	12500	-4000	234	250	-4250
249	3250	-3750	251	12750	-4000	236	0	-4250
243	3000	-3750	241	13000	-4000	233	0	-4500
254	2750	-3750	247	13250	-4000	234	250	-4500
239	2500	-3750	246	13500	-4000	240	500	-4500
241	2250	-3750	243	13750	-4000	245	750	-4500
249	2000	-3750	247	14000	-4000	241	1000	-4500
253	1750	-3750	243	14250	-4000	236	1250	-4500

Table 15, Continued.

Hardness (HV₂₀₀)	X Coord. (µm)	Y Coord. (µm)
245	1500	-4500
256	1750	-4500
247	2000	-4500
263	2250	-4500
247	2500	-4500
257	2750	-4500
259	3000	-4500
251	12250	-4500
246	12500	-4500
243	12750	-4500
238	13000	-4500
228	13250	-4500
224	13500	-4500
228	13750	-4500
221	14000	-4500
223	14250	-4500
217	14500	-4500
231	14750	-4500
246	13000	-4750
233	12750	-4750
244	2000	-4750
271	1750	-4750
241	1500	-4750
248	1250	-4750
231	1000	-4750
229	750	-4750
218	500	-4750
210	250	-4750

Table 16. Vickers Microhardness Measurements across the Experimental Tee Joint Weldment Illustrated in **Figure 22** (Coordinate Origin in Top Left Corner)

Hardness (HV ₂₀₀)	X Coord. (μm)	Y Coord. (μm)	Hardness (HV ₂₀₀)	X Coord. (μm)	Y Coord. (μm)	Hardness (HV ₂₀₀)	X Coord. (μm)	Y Coord. (μm)
231	0	0	222	14399	162	216	17402	-54
224	300	4	N/A	11699	132	219	17102	-57
227	600	7	N/A	11999	135	212	16802	-60
236	900	10	203	12299	138	204	16502	-64
245	1200	14	207	12599	142	208	16202	-68
225	1500	17	217	12899	145	216	15902	-70
218	1800	20	218	13199	148	219	15602	-74
227	2100	24	211	13499	152	220	15302	-78
224	2400	27	222	13799	155	213	15002	-81
216	2700	30	211	14099	158	215	14702	-84
219	3000	34	222	14399	162	211	14402	-88
221	3300	38	201	14699	166	217	14102	-91
224	3600	40	214	14999	168	224	13802	-94
226	3900	44	210	15299	172	214	13502	-98
217	4200	48	221	15599	176	212	13202	-101
222	4500	51	208	15898	179	206	12902	-104
227	4800	54	226	16198	182	228	12602	-108
220	5100	58	223	16498	186	263	12302	-111
214	5400	61	225	16798	189	262	12002	-114
218	5700	64	229	17098	192	246	11702	-118
222	6000	68	244	17398	196	244	11402	-121
236	6300	71	224	17698	199	239	11102	-124
226	6600	74	225	17998	202	241	10802	-128
229	6900	78	229	18298	206	250	10502	-132
215	7200	81	213	18598	209	263	10202	-134
222	7500	84	193	18898	212	263	9902	-138
N/A	7800	88	249	19198	216	256	9602	-142
N/A	11999	135	223	19498	219	262	9302	-145
203	12299	138	234	19798	222	249	9002	-148
207	12599	142	241	20098	226	241	8702	-152
217	12899	145	252	20398	230	246	8402	-155
218	13199	148	257	20698	232	243	8102	-158
211	13499	152	267	20998	236	255	7802	-162
222	13799	155	273	21001	-14	280	7502	-165
211	14099	158	269	20702	-17	303	7202	-168

Table 16, Continued.

Hardness (HV ₂₀₀)	X Coord. (µm)	Y Coord. (µm)	Hardness (HV ₂₀₀)	X Coord. (µm)	Y Coord. (µm)	Hardness (HV ₂₀₀)	X Coord. (µm)	Y Coord. (µm)
212	6902	-172	231	3905	-456	211	15004	-331
206	6602	-175	226	4205	-452	214	15304	-328
240	6302	-178	228	4505	-448	209	15604	-324
221	6002	-182	216	4805	-446	214	15904	-320
231	5702	-185	204	5105	-442	224	16204	-318
206	5402	-188	222	5405	-438	217	16504	-314
221	5102	-192	220	5705	-435	249	16804	-310
225	4802	-196	226	6005	-432	258	17104	-307
218	4502	-198	275	6305	-428	241	17404	-304
211	4202	-202	272	6605	-425	274	17704	-300
221	3902	-206	282	6905	-422	294	18004	-297
223	3602	-209	274	7205	-418	276	18304	-294
210	3302	-212	263	7505	-415	285	18604	-290
229	3002	-216	245	7805	-412	274	18904	-287
219	2702	-219	245	8105	-408	252	19204	-284
216	2402	-222	246	8405	-405	249	19504	-280
217	2102	-226	246	8705	-402	248	19804	-277
224	1802	-229	259	9005	-398	248	20104	-274
218	1502	-232	272	9305	-395	269	20404	-270
279	1202	-236	269	9605	-392	266	20704	-267
264	902	-239	265	9904	-388	268	21004	-264
254	602	-242	259	10204	-384	276	21007	-514
252	302	-246	259	10504	-382	271	20707	-517
235	2	-249	242	10804	-378	278	20407	-520
243	6	-499	241	11104	-374	259	20107	-524
248	306	-496	241	11404	-371	246	19807	-527
249	606	-492	234	11704	-368	246	19507	-530
246	906	-489	237	12004	-364	261	19207	-534
291	1206	-486	258	12304	-361	252	18907	-537
257	1506	-482	297	12604	-358	275	18607	-540
272	1806	-479	260	12904	-354	288	18307	-544
288	2105	-476	245	13204	-351	281	18007	-547
285	2405	-472	219	13504	-348	307	17707	-550
250	2705	-469	216	13804	-344	303	17407	-554
249	3005	-466	220	14104	-341	271	17107	-557
226	3305	-462	224	14404	-338	214	16807	-560
229	3605	-459	221	14704	-334	218	16507	-564

Table 16, Continued.

Hardness (HV ₂₀₀)	X Coord. (µm)	Y Coord. (µm)	Hardness (HV ₂₀₀)	X Coord. (µm)	Y Coord. (µm)	Hardness (HV ₂₀₀)	X Coord. (µm)	Y Coord. (µm)
210	16207	-568	234	5108	-692	310	5710	-935
204	15907	-570	220	4808	-696	307	6010	-932
218	15607	-574	243	4508	-698	310	6310	-928
211	15307	-578	226	4208	-702	306	6610	-925
217	15007	-581	255	3908	-706	270	6910	-922
220	14707	-584	273	3608	-709	269	7210	-918
241	14408	-588	289	3308	-712	253	7510	-915
274	14108	-591	301	3008	-716	248	7810	-912
306	13808	-594	283	2708	-719	247	8110	-908
282	13508	-598	301	2408	-722	246	8410	-905
274	13208	-601	288	2108	-726	260	8710	-902
288	12908	-604	300	1808	-729	263	9010	-898
252	12608	-608	306	1508	-732	268	9310	-895
242	12308	-611	247	1208	-736	263	9610	-892
246	12008	-614	239	908	-739	268	9910	-888
243	11708	-618	242	608	-742	265	10210	-884
243	11408	-621	256	308	-746	275	10510	-882
252	11108	-624	254	8	-749	270	10810	-878
254	10808	-628	267	11	-999	246	11110	-874
248	10508	-632	263	311	-996	252	11410	-871
268	10208	-634	249	611	-992	248	11710	-868
263	9908	-638	250	911	-989	246	12010	-864
263	9608	-642	257	1211	-986	246	12310	-861
263	9308	-645	267	1511	-982	245	12610	-858
252	9008	-648	291	1811	-979	260	12910	-854
241	8708	-652	312	2111	-976	273	13210	-851
247	8408	-655	292	2411	-972	290	13510	-848
247	8108	-658	309	2711	-969	299	13810	-844
252	7808	-662	311	3011	-966	300	14110	-841
250	7508	-665	298	3311	-962	303	14410	-838
279	7208	-668	283	3611	-959	298	14710	-834
287	6908	-672	299	3910	-956	288	15010	-831
309	6608	-675	310	4210	-952	235	15310	-828
300	6308	-678	305	4510	-948	206	15610	-824
312	6008	-682	312	4810	-946	208	15910	-820
249	5708	-685	311	5110	-942	204	16210	-818
225	5408	-688	291	5410	-938	239	16510	-814

Table 16, Continued.

Hardness (HV ₂₀₀)	X Coord. (µm)	Y Coord. (µm)	Hardness (HV ₂₀₀)	X Coord. (µm)	Y Coord. (µm)	Hardness (HV ₂₀₀)	X Coord. (µm)	Y Coord. (µm)
317	16810	-810	303	14413	-1088	274	3314	-1212
293	17110	-807	290	14113	-1091	309	3014	-1216
297	17410	-804	274	13813	-1094	307	2714	-1219
300	17710	-800	272	13513	-1098	293	2414	-1222
299	18010	-797	258	13213	-1101	267	2114	-1226
292	18310	-794	252	12913	-1104	261	1814	-1229
272	18610	-790	246	12613	-1108	252	1514	-1232
243	18910	-787	246	12313	-1111	258	1214	-1236
239	19210	-784	249	12013	-1114	260	914	-1239
250	19510	-780	244	11713	-1118	245	614	-1242
251	19810	-777	249	11413	-1121	253	314	-1246
266	20110	-774	251	11113	-1124	258	14	-1249
262	20410	-770	268	10813	-1128	248	16	-1499
269	20710	-767	268	10513	-1132	262	316	-1496
267	21010	-764	261	10213	-1134	231	616	-1492
268	21012	-1014	257	9913	-1138	246	916	-1489
266	20712	-1017	259	9613	-1142	235	1216	-1486
273	20412	-1020	268	9313	-1145	242	1516	-1482
273	20112	-1024	262	9013	-1148	246	1816	-1479
267	19812	-1027	260	8713	-1152	266	2116	-1476
254	19512	-1030	265	8414	-1155	274	2416	-1472
251	19212	-1034	257	8114	-1158	265	2716	-1469
251	18912	-1037	259	7814	-1162	259	3016	-1466
254	18612	-1040	246	7514	-1165	278	3316	-1462
256	18312	-1044	255	7214	-1168	262	3616	-1458
263	18012	-1047	255	6914	-1172	273	3916	-1456
297	17712	-1050	253	6614	-1175	305	4216	-1452
296	17412	-1054	274	6314	-1178	254	4516	-1448
319	17112	-1057	284	6014	-1182	275	4816	-1446
298	16812	-1060	282	5714	-1185	271	5116	-1442
284	16512	-1064	292	5414	-1188	272	5416	-1438
306	16213	-1068	303	5114	-1192	262	5716	-1435
284	15913	-1070	298	4814	-1196	247	6016	-1432
307	15613	-1074	303	4514	-1198	245	6316	-1428
280	15313	-1078	302	4214	-1202	250	6616	-1425
279	15013	-1081	305	3914	-1206	241	6916	-1422
290	14713	-1084	293	3614	-1209	236	7216	-1418

Table 16, Continued.

Hardness (HV ₂₀₀)	X Coord. (µm)	Y Coord. (µm)	Hardness (HV ₂₀₀)	X Coord. (µm)	Y Coord. (µm)	Hardness (HV ₂₀₀)	X Coord. (µm)	Y Coord. (µm)
228	7516	-1415	246	18616	-1290	229	12618	-1608
242	7816	-1412	243	18916	-1287	236	12318	-1611
252	8116	-1408	252	19216	-1284	257	12018	-1614
267	8416	-1405	248	19516	-1280	258	11718	-1618
255	8716	-1402	259	19816	-1277	255	11418	-1621
254	9016	-1398	269	20116	-1274	259	11118	-1624
260	9316	-1394	272	20416	-1270	256	10818	-1628
263	9616	-1392	264	20716	-1267	270	10518	-1632
270	9916	-1388	260	21016	-1264	265	10219	-1634
255	10216	-1384	263	21018	-1514	262	9919	-1638
262	10516	-1382	259	20718	-1516	266	9619	-1642
255	10816	-1378	259	20418	-1520	263	9319	-1644
250	11116	-1374	255	20118	-1524	260	9019	-1648
252	11416	-1371	249	19818	-1527	255	8719	-1652
228	11716	-1368	255	19518	-1530	273	8419	-1655
231	12016	-1364	244	19218	-1534	252	8119	-1658
234	12316	-1361	255	18918	-1537	261	7819	-1662
238	12616	-1358	261	18618	-1540	272	7519	-1665
236	12916	-1354	241	18318	-1544	262	7219	-1668
246	13216	-1351	245	18018	-1547	269	6919	-1672
241	13516	-1348	243	17718	-1550	260	6619	-1675
244	13816	-1344	237	17418	-1554	268	6319	-1678
249	14116	-1341	238	17118	-1557	263	6019	-1682
259	14416	-1338	259	16818	-1560	274	5719	-1685
259	14716	-1334	268	16518	-1564	263	5419	-1688
268	15016	-1330	249	16218	-1568	262	5119	-1692
242	15316	-1328	266	15918	-1570	273	4819	-1695
259	15616	-1324	286	15618	-1574	293	4519	-1698
272	15916	-1320	264	15318	-1578	274	4219	-1702
291	16216	-1318	241	15018	-1580	263	3919	-1706
281	16516	-1314	249	14718	-1584	278	3619	-1708
269	16816	-1310	257	14418	-1588	257	3319	-1712
267	17116	-1307	256	14118	-1591	263	3019	-1716
256	17416	-1304	261	13818	-1594	255	2719	-1719
246	17716	-1300	242	13518	-1598	243	2419	-1722
251	18016	-1297	252	13218	-1601	253	2120	-1726
252	18316	-1294	248	12918	-1604	246	1820	-1729

Table 16, Continued.

Hardness (HV ₂₀₀)	X Coord. (µm)	Y Coord. (µm)	Hardness (HV ₂₀₀)	X Coord. (µm)	Y Coord. (µm)	Hardness (HV ₂₀₀)	X Coord. (µm)	Y Coord. (µm)
249	1520	-1732	267	9322	-1894	255	20421	-1770
249	1220	-1736	265	9622	-1892	258	20721	-1766
250	920	-1739	258	9922	-1888	259	21021	-1764
253	620	-1742	256	10222	-1884	257	21024	-2014
263	320	-1746	260	10522	-1881	263	20724	-2016
267	20	-1749	267	10822	-1878	274	20424	-2020
259	22	-1999	255	11122	-1874	263	20124	-2024
255	322	-1996	259	11422	-1871	264	19824	-2027
263	622	-1992	258	11722	-1868	275	19524	-2030
275	922	-1989	246	12022	-1864	278	19224	-2034
254	1222	-1986	243	12322	-1861	259	18924	-2037
237	1522	-1982	249	12622	-1858	239	18624	-2040
248	1822	-1979	246	12922	-1854	236	18324	-2044
240	2122	-1976	231	13222	-1851	235	18024	-2047
244	2422	-1972	234	13522	-1848	251	17724	-2050
243	2722	-1969	230	13822	-1844	241	17424	-2054
251	3022	-1966	237	14122	-1841	237	17124	-2057
249	3322	-1962	238	14422	-1838	231	16824	-2060
251	3622	-1958	238	14722	-1834	249	16524	-2064
244	3922	-1956	241	15022	-1830	252	16224	-2067
246	4222	-1952	249	15321	-1828	238	15924	-2070
244	4522	-1948	250	15621	-1824	237	15624	-2074
255	4822	-1945	246	15921	-1820	238	15324	-2078
266	5122	-1942	246	16221	-1817	255	15024	-2080
265	5422	-1938	235	16521	-1814	240	14724	-2084
246	5722	-1935	231	16821	-1810	263	14424	-2088
249	6022	-1932	240	17121	-1807	268	14124	-2091
238	6322	-1928	248	17421	-1804	253	13824	-2094
257	6622	-1925	252	17721	-1800	236	13524	-2098
252	6922	-1922	259	18021	-1797	236	13224	-2101
246	7222	-1918	253	18321	-1794	227	12924	-2104
259	7522	-1915	258	18621	-1790	234	12624	-2108
257	7822	-1912	258	18921	-1787	225	12324	-2111
246	8122	-1908	258	19221	-1784	246	12024	-2114
251	8422	-1905	252	19521	-1780	254	11724	-2118
247	8722	-1902	259	19821	-1777	249	11424	-2121
268	9022	-1898	257	20121	-1774	261	11124	-2124

Table 16, Continued.

Hardness (HV ₂₀₀)	X Coord. (µm)	Y Coord. (µm)	Hardness (HV ₂₀₀)	X Coord. (µm)	Y Coord. (µm)	Hardness (HV ₂₀₀)	X Coord. (µm)	Y Coord. (µm)
265	10824	-2128	265	28	-2499	259	11127	-2374
274	10524	-2131	251	328	-2496	259	11427	-2371
255	10224	-2134	249	628	-2492	269	11727	-2368
258	9924	-2138	254	928	-2489	238	12027	-2364
252	9624	-2142	242	1228	-2486	213	12327	-2361
264	9324	-2144	235	1528	-2482	243	12627	-2358
257	9024	-2148	241	1828	-2479	226	12927	-2354
247	8724	-2152	241	2128	-2476	235	13227	-2351
252	8424	-2155	235	2428	-2472	237	13527	-2348
243	8124	-2158	221	2728	-2469	239	13827	-2344
229	7824	-2162	240	3028	-2466	235	14127	-2341
235	7524	-2165	238	3328	-2462	257	14427	-2338
239	7224	-2168	228	3628	-2458	226	14727	-2334
235	6924	-2172	230	3928	-2456	259	15027	-2330
232	6624	-2175	217	4228	-2452	236	15327	-2328
238	6324	-2178	233	4528	-2448	241	15627	-2324
238	6024	-2182	240	4828	-2445	238	15927	-2320
241	5724	-2185	234	5128	-2442	233	16227	-2317
238	5424	-2188	240	5428	-2438	234	16527	-2314
234	5124	-2192	259	5728	-2435	238	16827	-2310
246	4824	-2195	263	6028	-2432	228	17126	-2307
239	4524	-2198	238	6328	-2428	223	17426	-2304
252	4224	-2202	240	6628	-2425	236	17726	-2300
261	3925	-2206	238	6928	-2422	232	18026	-2297
252	3625	-2208	240	7228	-2418	238	18326	-2294
235	3325	-2212	244	7528	-2415	234	18626	-2290
252	3025	-2216	259	7828	-2412	249	18926	-2287
237	2725	-2219	266	8128	-2408	256	19226	-2284
238	2425	-2222	264	8428	-2405	249	19526	-2280
238	2125	-2226	270	8728	-2402	256	19826	-2277
248	1825	-2229	257	9028	-2398	251	20126	-2274
245	1525	-2232	259	9327	-2394	262	20426	-2270
259	1225	-2236	249	9627	-2392	262	20726	-2266
264	925	-2239	258	9927	-2388	259	21026	-2264
259	625	-2242	256	10227	-2384	268	21030	-2514
249	325	-2246	246	10527	-2381	269	20730	-2516
259	25	-2249	249	10827	-2378	273	20430	-2520

Table 16, Continued.

Hardness (HV ₂₀₀)	X Coord. (µm)	Y Coord. (µm)	Hardness (HV ₂₀₀)	X Coord. (µm)	Y Coord. (µm)	Hardness (HV ₂₀₀)	X Coord. (µm)	Y Coord. (µm)
265	20130	-2524	256	9030	-2648	255	1834	-2979
259	19830	-2527	255	8730	-2652	246	2134	-2976
246	19530	-2530	256	8430	-2655	244	2434	-2972
254	19230	-2534	248	8130	-2658	255	2734	-2968
252	18930	-2537	252	7830	-2662	243	3033	-2966
254	18630	-2540	244	7530	-2665	260	3333	-2962
252	18330	-2544	233	7230	-2668	252	3633	-2958
238	18030	-2547	238	6930	-2672	246	3933	-2956
231	17730	-2550	236	6630	-2675	248	4233	-2952
238	17430	-2554	228	6330	-2678	251	4533	-2948
254	17130	-2557	232	6030	-2682	252	4833	-2945
236	16830	-2560	241	5730	-2685	253	5133	-2942
227	16530	-2564	247	5430	-2688	251	5433	-2938
232	16230	-2567	242	5130	-2692	252	5733	-2935
255	15930	-2570	236	4830	-2695	257	6033	-2932
252	15630	-2574	233	4530	-2698	260	6333	-2928
241	15330	-2578	246	4230	-2702	252	6633	-2925
260	15030	-2580	255	3930	-2706	253	6933	-2922
230	14730	-2584	247	3630	-2708	255	7233	-2918
239	14430	-2588	262	3330	-2712	257	7533	-2915
236	14130	-2591	241	3030	-2716	255	7833	-2912
246	13830	-2594	236	2730	-2719	271	8133	-2908
219	13530	-2598	246	2430	-2722	276	8433	-2905
224	13230	-2601	246	2130	-2726	274	8733	-2902
238	12930	-2604	263	1830	-2729	259	9033	-2898
228	12630	-2608	245	1530	-2732	261	9333	-2894
234	12330	-2611	266	1230	-2736	266	9633	-2892
243	12030	-2614	269	930	-2739	266	9933	-2888
243	11730	-2618	275	630	-2742	263	10233	-2884
247	11430	-2621	267	330	-2746	256	10533	-2881
251	11130	-2624	263	30	-2749	263	10833	-2878
255	10830	-2628	270	34	-2999	253	11132	-2874
252	10530	-2631	271	334	-2996	267	11432	-2871
256	10230	-2634	266	634	-2992	259	11732	-2868
260	9930	-2638	263	934	-2989	246	12032	-2864
255	9630	-2642	267	1234	-2986	247	12332	-2861
262	9330	-2644	259	1534	-2982	244	12632	-2858

Table 16, Continued.

Hardness (HV ₂₀₀)	X Coord. (µm)	Y Coord. (µm)	Hardness (HV ₂₀₀)	X Coord. (µm)	Y Coord. (µm)	Hardness (HV ₂₀₀)	X Coord. (µm)	Y Coord. (µm)
241	12932	-2854	252	18335	-3044	263	7236	-3168
250	13232	-2851	255	18035	-3047	259	6936	-3172
247	13532	-2848	253	17735	-3050	259	6636	-3175
245	13832	-2844	252	17435	-3054	251	6336	-3178
229	14132	-2841	249	17135	-3057	255	6036	-3182
231	14432	-2838	251	16835	-3060	256	5736	-3185
234	14732	-2834	246	16535	-3064	246	5436	-3188
236	15032	-2830	242	16235	-3067	255	5136	-3192
244	15332	-2828	238	15935	-3070	252	4836	-3195
238	15632	-2824	247	15636	-3074	244	4536	-3198
255	15932	-2820	251	15336	-3078	246	4236	-3202
249	16232	-2817	246	15036	-3080	248	3936	-3206
249	16532	-2814	249	14736	-3084	252	3636	-3208
254	16832	-2810	252	14436	-3088	253	3336	-3212
248	17132	-2807	254	14136	-3090	246	3036	-3216
243	17432	-2804	243	13836	-3094	249	2736	-3218
258	17732	-2800	251	13536	-3098	250	2436	-3222
254	18032	-2797	255	13236	-3101	260	2136	-3226
246	18332	-2794	246	12936	-3104	258	1836	-3229
274	18632	-2790	259	12636	-3108	264	1536	-3232
259	18932	-2787	265	12336	-3111	264	1236	-3236
270	19232	-2784	255	12036	-3114	270	936	-3239
268	19532	-2780	256	11736	-3118	257	636	-3242
275	19832	-2777	263	11436	-3121	262	336	-3246
274	20132	-2774	262	11136	-3124	263	36	-3249
279	20432	-2770	268	10836	-3128			
271	20732	-2766	265	10536	-3131			
270	21032	-2764	270	10236	-3134			
266	21035	-3014	267	9936	-3138			
263	20735	-3016	274	9636	-3142			
276	20435	-3020	272	9336	-3144			
275	20135	-3024	268	9036	-3148			
269	19835	-3026	268	8736	-3152			
268	19535	-3030	266	8436	-3154			
270	19235	-3034	268	8136	-3158			
259	18935	-3037	270	7836	-3162			
256	18635	-3040	264	7536	-3165			

Appendix E: Thermo-Physical Property Datasets for HSLA-100**Table 17.** Experimentally Measured Specific Heat of HSLA-100

Temperature (°C)	c_p (J/g-°C)	(°C)	c_p (J/g-°C)	(°C)	c_p (J/g-°C)	(°C)	c_p (J/g-°C)
23	0.4485	320	0.5623	620	0.776	920	0.6195
30	0.4516	330	0.567	630	0.7971	930	0.621
40	0.456	340	0.5709	640	0.8134	940	0.6354
50	0.4603	350	0.5746	650	0.8369	950	0.6356
60	0.4645	360	0.5787	660	0.8647	960	0.6392
70	0.4686	370	0.5829	670	0.8998	970	0.6428
80	0.4727	380	0.5874	680	0.9333	980	0.6504
90	0.4767	390	0.5919	690	0.9722	990	0.6583
100	0.4809	400	0.5972	700	1.0093	1000	0.6562
110	0.4846	410	0.6021	710	1.0486	1010	0.6716
120	0.4882	420	0.6072	720	1.1102	1020	0.6857
130	0.492	430	0.6126	730	1.2066	1030	0.6747
140	0.4956	440	0.6177	740	1.3125	1040	0.6831
150	0.4991	450	0.623	750	1.2621	1050	0.6715
160	0.5027	460	0.6283	760	1.1049	1060	0.6811
170	0.5062	470	0.6345	770	1.021	1070	0.6823
180	0.5098	480	0.6412	780	0.9707	1080	0.6809
190	0.5136	490	0.6486	790	0.9501	1090	0.6836
200	0.5172	500	0.6556	800	0.9376	1100	0.6879
210	0.5208	510	0.6653	810	0.9301	1110	0.6802
220	0.5243	520	0.6759	820	0.9193	1120	0.6825
230	0.5278	530	0.6829	830	0.8879	1130	0.674
240	0.5312	540	0.6851	840	0.8065	1140	0.6642
250	0.5345	550	0.6919	850	0.673	1150	0.6578
260	0.5379	560	0.699	860	0.6106	1160	0.7076
270	0.5411	570	0.7059	870	0.6024	1170	0.7357
280	0.5446	580	0.7215	880	0.6072	1180	0.7369
290	0.5483	590	0.7321	890	0.6072	1190	0.744
300	0.5525	600	0.7453	900	0.6149	1200	0.7473
310	0.5573	610	0.7588	910	0.6225		

Table 18. Experimentally Measured Thermal Properties of HSLA-100

Temperature (°C)	Thermal Diffusivity (cm²/sec)	Density (g/cm³)	Thermal Conductivity (W/cm-°C)
23	0.09606	7.4653	0.32163
50	0.09585	7.4608	0.32917
100	0.09528	7.4466	0.34121
200	0.09096	7.4169	0.34893
300	0.08414	7.3858	0.34335
400	0.07571	7.3527	0.33245
500	0.06691	7.3190	0.32106
600	0.05623	7.2854	0.30532
700	0.04121	7.2545	0.28957
800	0.05367	7.2617	0.23435
900	0.05984	7.2764	0.26774
1000	0.06135	7.2326	0.29117
1100	0.06296	7.1933	0.31154
1200	0.05834	7.1540	0.31190
1300	---	7.1147	---

Appendix F: Thermo-Mechanical Properties

Table 19. Assumed Elevated Temperature Elastic Modulus for HSLA-100 Base Material. Note: Data are based on an assumed room temperature modulus of 210 GPa (30.5 Msi) as shown in **Figure 28**.

Temperature (°C [°F])	Fraction of Room Temperature Modulus	Elastic Modulus (GPa [Msi])
23 (73)	1.0000	210 (30.5)
100 (212)	1.0000	210 (30.5)
200 (392)	0.9000	189 (27.4)
300 (572)	0.8000	168 (24.4)
400 (752)	0.7000	147 (21.3)
500 (932)	0.6000	126 (18.3)
600 (1112)	0.3100	65 (9.4)
700 (1292)	0.1300	27 (4.0)
800 (1472)	0.0900	19 (2.7)
900 (1652)	0.0675	14 (2.1)
1000 (1832)	0.0450	9 (1.4)
1100 (2012)	0.0225	5 (0.7)
1200 (2192)	0.0000	0 (0)

Table 20. Elevated Temperature Mechanical Properties of HSLA-100 Base Material. Data as shown in **Figures 29-30**.

Test Temperature (°C [°F])	Yield Strength (MPa [ksi])	Tensile Strength (MPa [ksi])
23 (74)	732 (106)	807 (117)
200 (392)	714 (104)	859 (125)
400 (752)	580 (84)	633 (92)
600 (1112)	348 (50)	422 (61)
700 (1292)	137 (20)	183 (27)
800 (1472)	34 (4.9)	51 (7.4)
900 (1652)	46 (6.7)	55 (8.0)
1000 (1832)	31 (4.5)	39 (5.7)
1100 (2012)	6.5 (0.94)	8.2 (1.2)

Table 21. Yield Strength of Simulated HSLA-100 CGHAZs after Heating to 1350 °C (2462 °F) and Cooling at Different Rates. Note: Data as illustrated in **Figure 31**.

Temperature (°C) [°F]	Yield Strength (MPa)			
	1 °C/s Cooling	10 °C/s Cooling	25 °C/s Cooling	100 °C/s Cooling
25 [77]	541	753	788	773
200 [392]	580	766	812	854
400 [752]	498	709	748	731
600 [1112]	407	418	438	458
700 [1292]	235	177	188	204

Table 22. On-Heating Flow Behavior of HSLA-100 Base Material. Note: Data as shown in **Figures 32-33**.

22 °C (72 °F)		200 °C (392 °F)		400 °C (752 °F)		600 °C (1112 °F)		700 °C (1292 °F)	
$\epsilon_{p, true}$	σ (MPa)	$\epsilon_{p, true}$	σ (MPa)	$\epsilon_{p, true}$	σ (MPa)	$\epsilon_{p, true}$	σ (MPa)	$\epsilon_{p, true}$	σ (MPa)
0.000	720	0.000	665	0.000	550	0.000	320	0.000	100
0.005	735	0.005	759	0.005	610	0.005	390	0.005	158
0.010	750	0.010	782	0.010	635	0.010	410	0.010	171
0.020	780	0.020	815	0.015	644	0.020	420	0.020	186
0.030	805	0.030	850					0.030	189
0.040	825	0.040	875					0.040	191
0.050	842	0.050	896					0.050	193
0.100	900							0.100	195
0.200	960							0.109	195
0.250	973								

800 °C (1472 °F)		900 °C (1652 °F)		1000 °C (1832 °F)		1100 °C (2012 °F)	
$\epsilon_{p, true}$	σ (MPa)	$\epsilon_{p, true}$	σ (MPa)	$\epsilon_{p, true}$	σ (MPa)	$\epsilon_{p, true}$	σ (MPa)
0.000	35	0.000	32	0.000	29	0.000	6
0.005	41	0.005	49	0.005	33	0.005	6.5
0.010	42	0.010	51	0.010	34	0.010	7.0
0.020	45	0.020	53	0.020	36	0.020	7.4
0.030	48	0.030	54	0.030	37	0.030	7.5
0.040	50	0.040	56	0.040	38	0.040	7.5
0.050	52	0.050	57	0.050	39		
0.100	59	0.100	61	0.100	44		
0.165	66	0.200	66	0.160	48		
		0.300	67				

Table 23. Flow Stress of Simulated HSLA-100 CGHAZs after Heating to 1350 °C (2462 °F) and Cooling at 1 °C/s (1.8 °F/s). Note: Data as illustrated in **Figure 34** and terminal values are at the UTS.

25 °C (77 °F)		200 °C (392 °F)		400 °C (752 °F)		600 °C (1112 °F)		700 °C (1292 °F)	
$\epsilon_{p, true}$	σ (MPa)	$\epsilon_{p, true}$	σ (MPa)	$\epsilon_{p, true}$	σ (MPa)	$\epsilon_{p, true}$	σ (MPa)	$\epsilon_{p, true}$	σ (MPa)
0	541	0	580	0	498	0	407	0	235
0.005	644	0.005	637	0.005	568	0.005	462	0.0048	272
0.01	681	0.01	666	0.01	606	0.01	469		
0.02	732	0.02	695	0.02	653	0.105	470		
0.03	760	0.03	710	0.03	686				
0.04	780	0.04	723	0.04	718				
0.05	793	0.0473	731	0.5	740				
0.056	800			0.0907	791				

Table 24. Flow Stress of Simulated HSLA-100 CGHAZs after Heating to 1350 °C (2462 °F) and Cooling at 10 °C/s (18 °F/s). Note: Data as illustrated in **Figure 35** and terminal values are at the UTS.

25 °C (77 °F)		200 °C (392 °F)		400 °C (752 °F)		600 °C (1112 °F)		700 °C (1292 °F)	
$\epsilon_{p, true}$	σ (MPa)	$\epsilon_{p, true}$	σ (MPa)	$\epsilon_{p, true}$	σ (MPa)	$\epsilon_{p, true}$	σ (MPa)	$\epsilon_{p, true}$	σ (MPa)
0	753	0	766	0	709	0	418	0	177
0.005	860	0.005	889	0.005	785	0.005	493	0.005	213
0.01	906	0.01	943	0.01	813	0.010	509	0.0074	216
0.02	937	0.02	995	0.02	840				
0.03	964	0.03	1017	0.03	854				
0.04	969	0.04	1027	0.0311	857				
0.05	977	0.05	1036						
0.059	977	0.10	1057						
		0.111	1057						

Table 25. Flow Stress of Simulated HSLA-100 CGHAZs after Heating to 1350 °C (2462 °F) and Cooling at 25 °C/s (45 °F/s). Data as illustrated in **Figure 36** and terminal values are at the UTS.

25 °C (77 °F)		200 °C (392 °F)		400 °C (752 °F)		600 °C (1112 °F)		700 °C (1292 °F)	
$\epsilon_{p, true}$	σ (MPa)	$\epsilon_{p, true}$	σ (MPa)	$\epsilon_{p, true}$	σ (MPa)	$\epsilon_{p, true}$	σ (MPa)	$\epsilon_{p, true}$	σ (MPa)
0	788	0	812	0	748	0	438	0	188
0.005	893	0.005	926	0.005	822	0.005	505	0.005	208
0.01	938	0.01	978	0.01	852	0.008	510	0.0059	208
0.02	976	0.02	1025	0.02	880				
0.03	993	0.03	1045	0.0276	888				
0.036	1003	0.0391	1060						

Table 26. Flow Stress of Simulated HSLA-100 CGHAZs after Heating to 1350 °C (2462 °F) and Cooling at 100 °C/s (180 °F/s). Data as illustrated in **Figure 37** and terminal values are at the UTS.

25 °C (77 °F)		200 °C (392 °F)		400 °C (752 °F)		600 °C (1112 °F)		700 °C (1292 °F)	
$\epsilon_{p, true}$	σ (MPa)	$\epsilon_{p, true}$	σ (MPa)	$\epsilon_{p, true}$	σ (MPa)	$\epsilon_{p, true}$	σ (MPa)	$\epsilon_{p, true}$	σ (MPa)
0	773	0	854	0	731	0	458	0	204
0.005	917	0.005	958	0.005	817	0.005	504	0.0047	223
0.01	967	0.01	1007	0.01	849	0.0066	508		
0.02	1012	0.02	1058	0.02	877				
0.03	1031	0.03	1079	0.0258	885				
0.035	1037	0.04	1092						
		0.041	1096						

Table 27. Engineering Fracture Strain for the Specimens Shown in **Figures 34-36**.

Temperature (°C) [°F]	Fracture Strain, $\epsilon_{f, eng}$ (mm/mm)			
	1 °C/s Cooling	10 °C/s Cooling	25 °C/s Cooling	100 °C/s Cooling
25 [77]	0.311	0.291	0.259	0.267
200 [392]	0.254	0.193	0.182	0.185
400 [752]	0.257	0.181	0.191	0.169
600 [1112]	0.041	0.025	0.018	0.016
700 [1292]	0.020	0.045	0.047	0.046

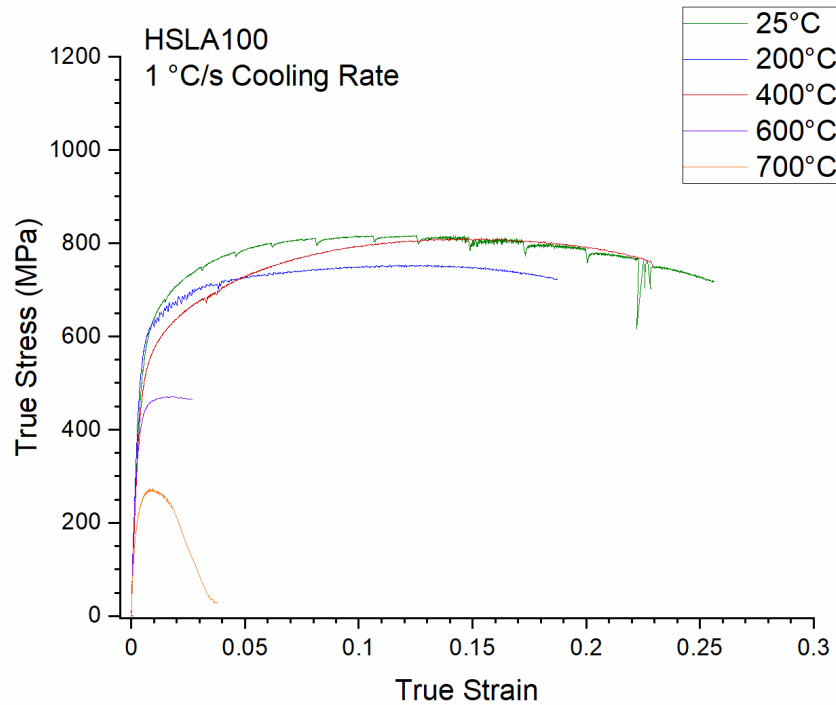


Figure 68. Uniaxial tension stress-strain curves from Gleeble tensile samples thermally cycled to a peak temperature of 1350 °C (2462 °F), cooled at 1 °C/s (1.8 °F/s), then reheated to the test temperature.

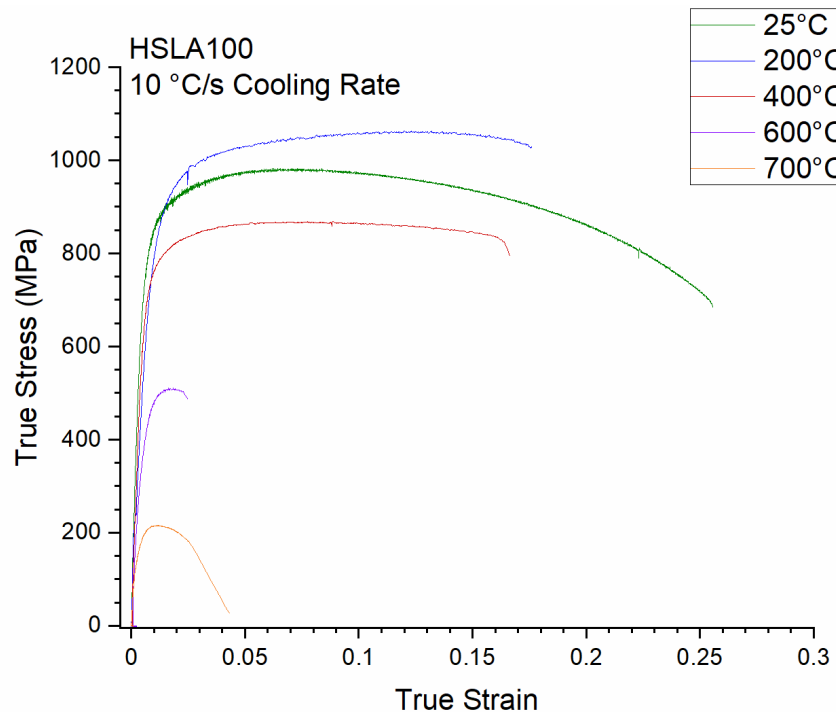


Figure 69. Uniaxial tension stress-strain curves from Gleeble tensile samples thermally cycled to a peak temperature of 1350 °C (2462 °F), cooled at 10 °C/s (18 °F/s), then reheated to the test temperature.

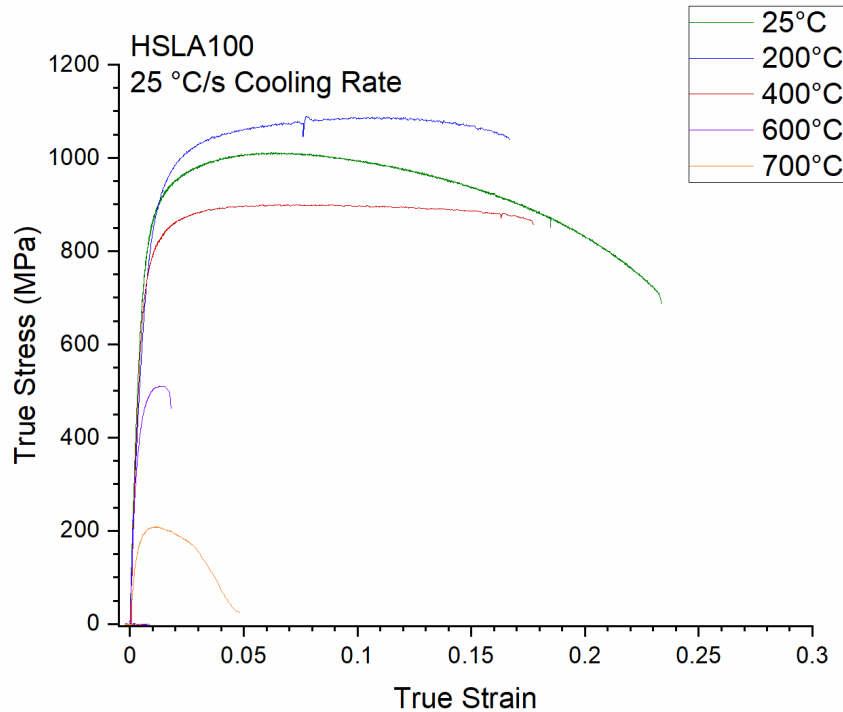


Figure 70. Uniaxial tension stress-strain curves from Gleeble tensile samples thermally cycled to a peak temperature of 1350 °C (2462 °F), cooled at 25 °C/s (45 °F/s), then reheated to the test temperature.

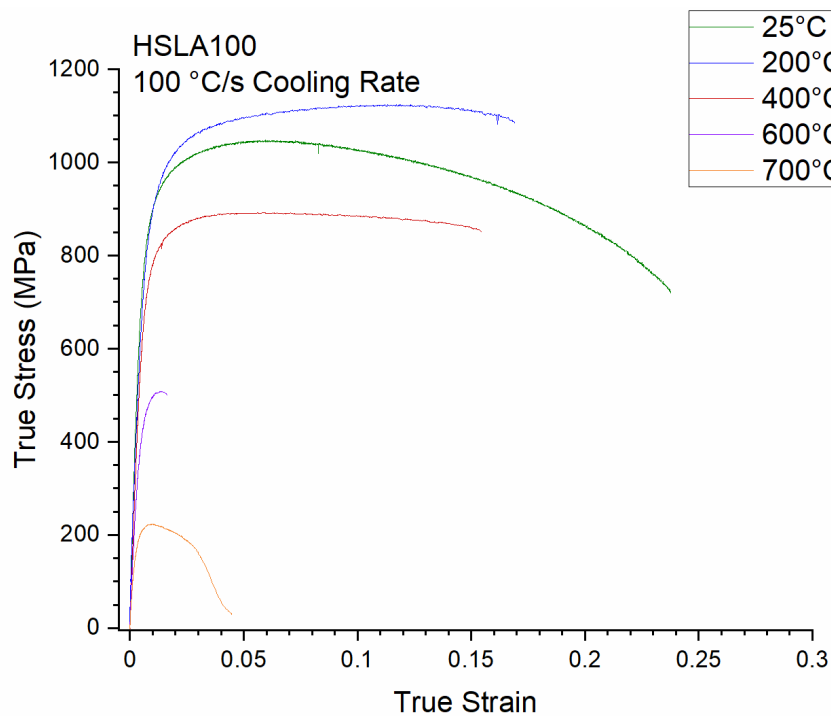


Figure 71. Uniaxial tension stress-strain curves from Gleeble tensile samples thermally cycled to a peak temperature of 1350 °C (2462 °F), cooled at 100 °C/s (180 °F/s), then reheated to the test temperature.

REFERENCES

- [1] L. F. Andersen, "Residual Stresses and Deformations in Steel Structures," Doctoral Thesis, Department of Naval Architecture and Offshore Engineering, University of Denmark, 2000.
- [2] MIL-S-22698C, "Military Specification: Steel Plate, Shapes, and Bars, Weldable Ordinary Strength and Higher Strength: Structural," 29 June 1988.
- [3] ASTM A945/M-16, "Standard Specification for High-Strength Low-Alloy Structural Steel Plate with Low Carbon and Restricted Sulfur for Improved Weldability, Formability, and Toughness," ASTM International, West Conshohocken, PA, 2016.
- [4] NAVSEA Technical Publication T9074-BD-GIB-010/0300 Rev. 2, "Base Materials for Critical Applications: Requirements for Low Alloy Steel Plate, Forgings, Castings, Shapes, Bars, and Heats of HY-80/100/130 and HSLA-80/100," 18 December 2012.
- [5] D. H. Bechetti, J. K. Semple, C. R. Fisher and W. Zhang, "Temperature-Dependent Material Property Databases for Marine Steels - Part 1: DH36," NSWCCD-61-TR-2019/03, 2019.
- [6] J. K. Semple, D. H. Bechetti, W. Zhang and C. R. Fisher, "Temperature-Dependent Material Property Databases for Marine Steels - Part 2: HSLA-65," NSWCCD-61-TR-2020/03, 2020.
- [7] J. K. Semple, D. H. Bechetti, W. Zhang and C. R. Fisher, "Temperature-Dependent Material Property Databases for Marine Steels - Part 3: HSLA-80," NSWCCD-61-TR-2020/24, 2020.
- [8] ASTM E417-17, "Standard Test Method for Analysis of Carbon and Low-Alloy Steel by Spark Atomic Emission Spectrometry," ASTM International, West Conshohocken, PA, 2017.
- [9] G. R. Eisler and P. W. Fuerschbach, "SOAR: An Extensible Suite of Codes for Weld Analysis and Optimal Weld Schedules," in *Seventh International Conference on Computer Technology in Welding*, San Francisco, CA, 1997.
- [10] ASTM E1461-13, "Standard Test Method for Thermal Diffusivity by the Flash Method," ASTM International, West Conshohocken, PA, 2013.
- [11] ASTM E1269-11 (2018), "Standard Test Method for Determining Specific Heat Capacity by Differential Scanning Calorimetry," ASTM International, West Conshohocken, PA, 2018.
- [12] ASTM A370-18, "Standard Test Methods and Definitions for Mechanical Testing of Steel Products," ASTM International, West Conshohocken, PA, 2018.
- [13] ASTM E21-17, "Standard Test Methods for Elevated Temperature Tension Tests of Metallic Materials," ASTM International, West Conshohocken, PA, 2017.
- [14] T. D. Huang, M. Harbison, S. Scholler, H. Rucker, J. Hu, P. Dong, M. Collette, H. Chung, M. Groden, W. Zhang, J. Semple, R. Kirchain, R. Roth, M. Bustamante, Y. Yang, R. Dull, Y. Goorochurn, M. Doroudian, C. F. Fisher, M. Sinfield, D. Kihl and A. Gonzalez, "Robust Distortion Control Methods and Implementation for Construction of Lightweight Metallic Structures," *SNAME Transactions*, 2016.
- [15] J. J. Valencia and C. Papesch, "Thermophysical Properties and High Temperature Tensile Properties of HSLA-100 Steel Plate," Naval Metalworking Center as operated by Concurrent Technologies Corporation, Johnstown, PA, 2007.
- [16] N. Yurioka, S. Oshita and H. Tamehiro, "Determination of Necessary Preheating Temperature in Steel Welding," *Welding Journal*, vol. 52, no. 6, pp. 147-s to 153-s, 1983.
- [17] X. Yue, J. C. Lippold, B. T. Alexandro and S. S. Babu, "Continuous Cooling Transformation Behavior in the CGHAZ of Naval Steels," *Welding Journal*, vol. 91, no. 3, pp. 67-s to 75-s, 2012.

- [18] ASTM E1382-97 (2015), "Standard Test Methods for Determining Average Grain Size Using Semiautomatic And Automatic Image Analysis," ASTM International, West Conshohocken, PA, 2015.
- [19] R. R. Mohanty, N. Fonstein and O. Girina, "Effect of Heating Rate on the Austenite Formation in Low-Carbon High-Strength Steels Annealed in the Intercritical Region," *Metallurgical and Materials Transaction A*, vol. 42A, no. 12, pp. 3680-3690, 2011.
- [20] F. L. G. Oliveira, M. S. Andrade and A. B. Cota, "Kinetics of Austenite Formation during Continuous Heating in a Low Carbon Steel," *Materials Characterization*, vol. 58, pp. 256-261, 2007.
- [21] C. A. Apple and G. Krauss, "The Effect of Heating Rate on the Martensite to Austenite Transformation in Fe-Ni-C Alloys," *Acta Materialia*, vol. 20, pp. 849-856, 1972.
- [22] Bainite Committee of The Iron & Steel Institute of Japan, "Atlas for Bainitic Microstructures, Vol. 1: Continuous-Cooled Microstructures of Low Carbon HSLA Steels," The Iron & Steel Institute of Japan, 1992.
- [23] H. K. D. H. Bhadeshia and R. W. K. Honeycombe, *Steels: Microstructure and Properties*, 3 ed., Oxford, UK: Butterworth-Heinemann, 2006.
- [24] A. K. Sinha, *Ferrous Physical Metallurgy*, Stoneham, MA: Butterworth Publishers, 1989.
- [25] G. Thewlis, "Classification and Quantification of Microstructures in Steels," *Materials Science and Technology*, vol. 20, pp. 143-160, 2004.
- [26] International Institute of Welding, *Compendium of Weld Metal Microstructures and Properties: Submerged-arc Welds in Ferritic Steel*, Cambridge, UK: Woodhead Publishing, 1985.
- [27] A. Bhagat, S. Pabi, S. Ranganathan and O. Mohanty, "Aging Behaviour in Copper Bearing High Strength Low Alloy Steels," *ISIJ International*, vol. 44, no. 1, pp. 115-122, 2004.
- [28] M. Sun, Y. Xu and J. Wang, "Effect of Aging Time on Microstructure and Mechanical Properties in a Cu-Bearing Marine Engineering Steel," *Materials*, vol. 13, no. 16, pp. 1-12, 2020.
- [29] S. Das, A. Ghosh, S. Chatterjee and P. Ramachandra Rao, "Evolution of microstructure in an ultra-low carbon Cu bearing HSLA forging," *Scandinavian Journal of Metallurgy*, vol. 31, pp. 272-280, 2002.
- [30] J. Valencia and C. Papesch, "Apparent Specific Heat and Thermal Expansion During Heating of HSLA-80 and DH-36 Steel Plates," Concurrent Technologies Corporation, Johnstown PA, 2005.
- [31] J. O. Andersson, T. Herlander, L. Hoglund, P. F. Shi and B. Sundman, "Thermo-Calc & DICTRA, Computational Tools for Materials Science," *Calphad*, vol. 26, pp. 92-101, 2002.
- [32] M. Shome and O. N. Mohanty, "Continuous cooling Transformation Diagrams Applicable to the Heat-Affected Zone of HSLA-80 and HSLA-100 Steels," *Metallurgical and Materials Transactions A*, vol. 37A, pp. 2159-2169, 2006.
- [33] G. Spanos, R. Fonda, R. Vandermeer and A. Matuszeski, "Microstructural Changes in HSLA-100 Steel Thermally Cycled to Simulate the Heat-Affected Zone during Welding," *Metallurgical and Materials Transactions A*, vol. 26A, pp. 3277-3293, 1995.
- [34] M. Peet, "Prediction of Martensite Start Temperature," *Materials Science and Technology*, vol. 31, no. 11, pp. 1370-1375, 2014.
- [35] S. Kang, S. Yoon and S.-J. Lee, "Prediction of Bainite Start Temperature in Alloy Steels with Difference Grain Sizes," *ISIJ International*, vol. 54, no. 4, pp. 997-999, 2014.
- [36] C. Capdevilla, F. G. Caballero and C. Garcia de Andres, "Determination of Ms Temperature in Steels: A Bayesian Neural Network Model," *ISIJ International*, vol. 42, pp. 894-902, 2002.

- [37] J. S. Kirkaldy and D. Venugopalan, "Phase Transformations in Ferrous Alloys," in *Phase Transformations in Ferrous Alloys: Proceedings of an International Conference*, Philadelphia, PA, 1984.
- [38] ASTM E111-17, "Standard Test Method for Young's Modulus, Tangent Modulus, and Chord Modulus," ASTM International, West Conshohocken, PA, 2017.
- [39] E. 1993-1-1, "Eurocode 3: Design of steel structures - Part 1-1: General rules and rules for buildings," 2005.
- [40] E. 1993-1-2, "Eurocode 3: Design of steel structures - Part 1-2: General rules - Structural fire design," 2005.
- [41] ASTM A541/M-05 (2015), "Standard Specification for Quenched and Tempered Carbon and Alloy Steel Forgings for Pressure Vessel Components," ASTM International, West Conshohocken, PA, 2015.
- [42] ASTM A131/M-14, "Standard Specification for Structural Steel for Ships," ASTM International, West Conshohocken, PA, 2014.
- [43] American Bureau of Shipping, "Rules for Materials and Welding (Part 2)," Houston, TX, 2016.
- [44] W. S. Rasband, "ImageJ," U. S. National Institutes of Health, Bethesda, MD, USA, 1997-2018. [Online]. Available: <https://imagej.nih.gov/ij/>.
- [45] C. Heinze, A. Pittner, M. Rethmeiri and S. S. Babu, "Dependency of Martensite Start Temperature on Prior Austenite Grain Size and Its Influence on Welding-Induced Residual Stress," *Computational Materials Science*, vol. 69, pp. 251-260, 2013.
- [46] B. Taljat, B. Radhakrishnan and T. Zacharia, "Numerical Analysis of GTA Welding Process with Emphasis on Post-Solidification Phase Transformation Effects on Residual Stress," *Materials Science and Engineering A*, vol. A246, pp. 45-54, 1998.
- [47] S.-J. Lee, J.-S. Park and Y.-K. Lee, "Effect of Austenite Grain Size on the Transformation kinetics of Upper and Lower Bainite in a Low-Alloy Steel," *Scripta Materialia*, vol. 59, no. 1, pp. 87-90, 2008.
- [48] P. Holsberg, "An Overview of Some Current Research on Welding Residual Stresses and Distortion in the U.S. Navy," Naval Surface Warfare Center, Carderock Division, West Bethesda, MD, 1997.
- [49] J. Valencia and C. Papesch, "Thermophysical Properties Characterization of HSLA-65 Rolled Plate," Concurrent Technologies Corporation, 2005.
- [50] J. Valencia and C. Papesch, "Thermophysical Properties and High Temperature Tensile Properties of HSLA-65 Steel Plate," Concurrent Technologies Corporation, 2007.
- [51] K. Sampath, "An Understanding of HSLA-65 Plate Steels," *Journal of Materials Engineering and Performance*, vol. 15, no. 1, pp. 32-40, 2006.

This page intentionally left blank

DISTRIBUTION

EXTERNAL

NSWCCD INTERNAL DISTRIBUTION

	<i>Copies</i>	<i>Code</i>	<i>Name</i>	<i>Copies</i>
DEFENSE TECHNICAL INFORMATION CENTER 727 JOHN J KINGMAN ROAD SUITE 0944 FORT BELVOIR, VA 22060-6218	1	60		1
		60	Mercier	1
		60	Rivera	1
		604	Waters	1
RESEARCH COMMONS NAVAL UNDERSEA WARFARE CENTER BUILDING 101 NEWPORT, RI 02841	1	61	DeLoach	1
		611	Davis	1
		611	Bechetti	1
		611	Fisher	2
		611	Semple	1
		611	Sinfield	1
COMMANDER ATTN: SEA 05P2 NAVAL SEA SYSTEMS COMMAND 1333 ISAAC HULL AVENUE S.E. WASHINGTON NAVY YARD WASHINGTON, DC 20376 ATTN: Archer, Bjornson, McGrorey, Melvin	4	612	Roe	1
		651	Nelson	1
		651	Rodriguez	1
		664	Miraglia	1
		664	Nahshon	1
ATTN: SEA 05P4 NAVAL SEA SYSTEMS COMMAND 1333 ISAAC HULL AVENUE S.E. WASHINGTON NAVY YARD WASHINGTON, DC 20376 ATTN: Rodgers	1			
OFFICE OF NAVAL RESEARCH 875 N RANDOLPH ST ARLINGTON, VA 22217 ATTN: Farren, Fonda, Mullins	1			
LIGHTWEIGHT INNOVATIONS FOR TOMORROW (LIFT) 1400 ROSA PARKS BOULEVARD DETROIT, MI 48216 ATTN: Hawke	1			
HUNTINGTON-INGALLS INDUSTRIES - INGALLS SHIPBUILDING 100 JERRY ST PE HIGHWAY PASCAGOULA, MS 39581 ATTN: Scholler, Yang	2			
OHIO STATE UNIVERSITY WELDING ENGINEERING PROGRAM 1248 ARTHUR E ADAMS DR COLUMBUS, OH 43221 ATTN: Zhang	1			

